Measurement of the B^0 Lifetime Using Partial Reconstruction*

Mahalaxmi Krishnamurthy

Stanford Linear Accelerator Center
Stanford University
Stanford, CA 94309

SLAC-Report-660

Prepared for the Department of Energy
under contract number DE-AC03-76SF00515

Printed in the United States of America. Available from the National Technical Information Service, U.S. Department of Commerce, 5285 Port Royal Road, Springfield, VA 22161.

* Ph.D. thesis, Colorado State University, Fort Collins, Colorado.

DISSERTATION

MEASUREMENT OF THE B^0 LIFETIME USING PARTIAL RECONSTRUCTION

Submitted by

Mahalaxmi Krishnamurthy

Department of Physics

In partial fulfillment of the requirements

for the Degree of Doctor of Philosophy

Colorado State University

Fort Collins, Colorado

Fall 2002

COLORADO STATE UNIVERSITY

August 14, 2002

WE HEREBY RECOMMEND THAT THE DISSERTATION PREPARED UNDER OUR SUPERVISION BY MAHALAXMI KRISHNAMURTHY ENTITLED MEASUREMENT OF THE B^0 LIFETIME USING PARTIAL RECONSTRUCTION BE ACCEPTED AS FULFILLING IN PART REQUIREMENTS FOR THE DEGREE OF DOCTOR OF PHILOSOPHY.

Committee on Graduate Work

Adviser

Department Head

ABSTRACT OF DISSERTATION

Measurement of the B^0 lifetime using Partial Reconstruction

We present here the first measurement of the B^0 lifetime using partial reconstruction in $B^0 \to D^{*-}\rho^+$ decay.

A sample of approximately 5500 $B^0 \to D^{*-}\rho^+$ events were identified among 22.7 million $B\bar{B}$ pairs collected by the *BABAR* experiment during the years 1999-2000. With this data, the B^0 lifetime is measured to be $1.616 \pm 0.064 \pm 0.075$ ps, in good agreement with the world average.

This measurement demonstrates that is it possible to use this technique to perform time-dependent B^0 decay analysis that is central to the measurement of the charge-parity ($\mathcal{CP}$) asymmetries. Investigation of $\mathcal{CP}$ observables through measurements of the decays of B^0 mesons is the primary goal of the *BABAR* experiment at the PEP-II storage ring located at Stanford Linear Accelerator Center (SLAC). As the B^0 particle decays to final states that are directly sensitive to the $\mathcal{CP}$ parameter γ are highly suppressed, a promising alternative approach is to use the final state $B^0 \to D^*h$. Using the partial event reconstruction analysis method it is possible to compensate for the small $\mathcal{CP}$ asymmetries in this decay.

Mahalaxmi Krishnamurthy
Physics Department
Colorado State University
Fort Collins, CO 80523
Fall 2002

Acknowledgments

I would like to thank my thesis advisor, Prof. Robert Wilson, for his constant support, advise and encouragement throughout this dissertation. He provided me with the wonderful opportunity to work on the *BABAR* experiment and its Cherenkov detector, DIRC, at SLAC during a very exciting phase of the experiment.

I am grateful for the generous help provided by Prof. Walter Toki and Prof. John Harton of the CSU HEP group.

I would like to express my gratitude to the members of the DIRC group, I have enjoyed to work with them. In particular, I thank the father of the DIRC (Dr. Blair Ratcliff), Dr. David Aston, Dr. Jaroslav Va'vra, Dr. Jochen Schwiening, and Dr. Stefan Spanier for the opportunity to work on understanding systematic issues of the DIRC and to guide me through the nuances of supervising the daily operation DIRC.

I would like thank to my wonderful colleagues at IR2 during my time as DIRC commissioner, in particular my fellow DIRC commissioners, Dr. Carsten Hast, Ms. Ingrid Ofte, Dr. Georges Vasileiadis who were always around to help and were a great pleasure to work with.

I am indebted to Dr. Abner Soffer who introduced me to the analysis method of partial reconstruction and for the invaluable discussions and guidance without which the analysis would have never reached its completion . I would like to thank my colleagues in the *BABAR* inclusive hadronic B decays analysis working group for their

constructive criticism and insights, in particular Dr. Wolfgang Walkowia and Dr. Marco Zito.

I would like to thank Dr. Wouter Verkerke for the constant software support on the very complex likelihood fit package. His quick bug fixes on the *BABAR* RooFit package not only saved some sleepless nights but also reduced the final computational time.

I not only enjoyed sharing the office with Dr. Johan Blouw, Dr. Wei Yang, and Jinglong Zhang but also the many interesting discussions on politics.

I am touched by the concern and constant encouragement throughout these years by all my friends and relatives. In particular, my uncle Mr. Swaminathan, who made the seven hours ordeal of waiting outside the US consulate in Bombay a fun experience.

I am greatly thankful to my parents, Lalita and Krishnamurthy, and my brother, Sundar, for their endless love, and unconditional support throughout my educational endeavors. I am very thankful to my husband, Stefan, for his constant encouragement and patience during my dissertation.

Contents

List of Figures

LIST OF FIGURES

List of Tables

Chapter 1

Introduction

1.1. Topic Overview

The discovery of parity violation in 1956 by C. S. Wu [1] and collaborators in nuclear β decays added a new perspective to the way we view nature. Prior to that pioneering work, equations that describe the fundamental interactions were thought to be invariant under the discrete symmetries of charge conjugation and parity. Subsequently the discovery of $\mathcal{CP}$ violation in 1964 by Christenson, Cronin, Fitch and Turlay [2] in the decay of neutral kaons at the Brookhaven National Laboratory overturned the untested assumption that the product of charge and parity, $\mathcal{CP}$, is a good symmetry in nature. Motivated by this discovery Kobayashi and Maskawa predicted the existence of a b quark (the thrid generation), as more than two generations of quarks are needed for $\mathcal{CP}$ violation, a year before the c quark was discovered and four years before the b quark was discovered in the form of the $\Upsilon(4S)$ resonance [3].

1. Introduction

From the Standard Model of weak interactions it is expected that in the kaon system the $\mathcal{CP}$ violation is a small effect and hence an impediment to the progress in that sector. There have been thirty-seven years of experimental studies in the kaon system since the discovery of $\mathcal{CP}$ violation and only recently direct $\mathcal{CP}$ violation has been observed [4; 5]. In contrast to the kaon system, the Standard Model of weak interactions implies that the B particle decays exhibit larger $\mathcal{CP}$ asymmetries as you compare things which are of the same order of magnitude. This prediction has been demonstrated by the *BABAR* and BELLE experiments [6; 7]. The ultimate goal of the B factories is to provide enough measurements on a large variety of final state decays of the B meson to fully understand $\mathcal{CP}$ violation in the context of the Standard Model or invalidate the Standard Model.

The resources required by such experiments mean that it is no longer a one nation quest but an international effort. The manpower required by such experiments is enormous. For example, there is a need for sub-system experts who are responsible for the day to day maintenance of the sub-detectors, responsible for maintaining the necessary software and to produce billions of Monte Carlo events that correctly simulate data to understand systematic effects. The *BABAR* experiment is made up of 560 collaborators from nine countries and 76 institutions from around the world. Though the success of each measurement is due in large part to the contributions of all collaborators, the results presented in this thesis are due primarily to the intellectual

efforts of the author.

1.2. Thesis Overview

The goal of this thesis is to establish whether or not the method of "partial reconstruction" can be used to do time-dependent measurements and hence the measurement of $\sin(2\beta+\gamma)$. The most convincing demonstration is the measurement of the B^0 lifetime, which would be the first measurement using this technique in the mode $B^0 \to D^{*-}\rho^+$ and is complementary to the precise measurement of the B^0 lifetime using the standard technique of "full reconstruction" (the low statistics in full reconstruction is compensated by the use of many decay channels). Previously, the method of partial reconstruction has been used to do only time-independent measurements. The advantage of the method of partial reconstruction over the traditional technique of full reconstruction is a gain in the number of reconstructed final state events. This is necessary to obtain a statistically significant measurement of $\sin(2\beta+\gamma)$. With a gain in the number of signal events there is also an increase in the number of background events that may influence the final result.

To establish the validity of a procedure one has first to establish the feasibility to do a competitive B^0 decay vertex reconstruction. A critical component is the understanding of backgrounds and their influence on the final result. One also needs to establish a stable and reproduceable fit procedure. In this thesis we hope to demon-

strate that the method of partial reconstruction can be used to do a time-dependent measurement. In the course of this analysis, we have made use of numerous software packages provided by members of the *BABAR* collaboration. Although we will attempt to use generic descriptions as much as possible, as an aid to other collaborators we provide references to *BABAR* specific terminology in parenthesis. These tools are provided and tested for use by the entire collaboration so that certain systematic errors and efficiencies are common to all analyses and a common correction can be applied.

The basic theoretical background for this analysis is presented in Chapter 2. It presents the different manifestations of $\mathcal{CP}$ violation. We describe the Standard Model prediction of $\mathcal{CP}$ violation with emphasis on the B system. The parameter of particular interest is $\sin(2\beta+\gamma)$, in the modes $B^0 \to D^* h$, is expected to be in the order of 2%. The details presented are a condensation of published papers.

Chapter 3 provides an overview of the PEP-II electron-positron storage ring and the sub-system components of the *BABAR* detector. Though the author was not involved in the design and construction of the detector she was a commissioner for the DIRC, the particle identification detector, for eighteen months. She gained a wealth of experience in the day to day operational issues of this sub-system. Some details of the operations and performance of the DIRC sub-detector are provided in Appendix-A.

Chapter 4 explains the selection and reconstruction of the final state of interest

out of millions of triggered events in the data collected by the experiment during the years 1999-2000. The special challenge is that the time-dependent $\mathcal{CP}$ asymmetries in the $B^0 \to D^* h$ are expected to be at a level of only about 2%. Hence a large number of events are needed to do a significant measurement, but the reconstruction of the D^0 decay modes produced in the decay of the D^* have a low efficiency. For a data set corresponding to approximately 100 million $B^0\overline{B}^0$ pairs the expected statistical error on $\sin(2\beta + \gamma)$ is 0.51 for the $B^0 \to D^{*-}\pi^+$ mode hence a large data sample is required to do a statistically significant measurement. The technique to increase efficiency is to select signal events in which the D^0 is not reconstructed from its decay products. This method of B^0 reconstruction is called "Partial Reconstruction". This results in a much larger efficiency albeit with higher background. In this chapter we describe the technique of partial reconstruction for event selection, which has been successfully used by the CLEO experiment in B decays to do time-independent measurements. The code to select events using partial reconstruction was already available as a standard *BABAR* code when the author started working on it.

At the time of this analysis no time-dependent measurements had been done using partial reconstruction in hadronic decay modes of the B^0, hence it was necessary to establish a procedure to reconstruct the decay vertex of the B^0 meson and the decay length time-difference, Δt. It is from this point on that the author made the most significant contributions to the analysis. Chapter 5 contains the details of the

reconstruction of the decay vertex position of the partially reconstructed B^0, and the other B^0. From the difference between the two decay positions the B^0 lifetime is derived. This difference between the two decay positions the B^0 is also central to the measurement of $\sin(2\beta + \gamma)$.

Chapter 6 describes the data and Monte Carlo simulation samples used in this analysis. The data set used for this analysis was collected during the 1999-2000 data-taking period and consists of 22.7 million $B\bar{B}$ pairs corresponding to an integrated luminosity of 20.7 fb^{-1} taken at the $\Upsilon(4S)$ resonance. An additional 2.6 fb^{-1} of data was collected about 40 MeV below the $\Upsilon(4S)$ resonance and was used to study the continuum background $e^+e^- \to q\bar{q}$ where $q = u, d, s$.

The final fit procedure used to extract the B^0 lifetime from multiple backgrounds requires 18 parameters. In chapter 7 the author explains the technique of the fit method used to obtain the B^0 lifetime. Backgrounds, with a signal to background ratio of 0.6 in partial reconstruction in the final state of interest, are a bigger challenge compared to full reconstruction where the ratio is greater than 4. Understanding the backgrounds is imperative to this analysis.

The fits were based on a likelihood fit package that was developed for *BABAR* within the ROOT frame work. The underlying minimization algorithm is the established MINUIT package from CERN. This fit package was developed at the same time when the author was working on time dependent fits for the lifetime measurement

and hence the author became involved in debugging and providing feedback on the code. This package is now a standard *BABAR* fit package.

Chapter 8 contains the results of the fit. It explains and quantifies the effect of various biases to the final lifetime measurement.

As the fit technique is very involved, a simplified Monte Carlo referred to in this thesis as a "Toy" Monte Carlo was used to test the technical correctness of the fit engine. This provides a robust estimate of the distribution of the fit parameters, their errors and the correlations between the parameters. In chapter 9 we describe this process in detail.

Chapter 10 explains the systematic error evaluation in the analysis and cross-checks that were done to establish the stability of the result. Due to backgrounds and a complicated fit technique a number of systematic checks needed to be performed that were not common to other *BABAR* time-dependent analysis. The systematic errors that are common to other *BABAR* time-dependent analysis are taken directly from them.

1.3. Analysis Review and Associated Work

The analysis detailed in this thesis has been presented at numerous *BABAR* collaboration meetings and has been reviewed by several senior collaboration physicists, primarily Prof. Patrica Burchat (Stanford University), Prof. Su Dong (SLAC) and

Dr. Martino Margoni (Universita'di Padova). It has been presented at the American Physical Society Division of Particles and Fields 2002 conference by the author and is to be submitted as a journal publication to Phys. Rev. D. Rapid Communications

As a consequence of the author's experience with time-dependent measurements she became involved in the preliminary steps for the measurement of $\sin(2\beta+\gamma)$ and also in the measurement of $\sin(2\beta)$ in the charmless decay of $B^0 \to \phi {K_s}^0$. The latter analysis is to be presented at conferences in summer 2002 but is not included in this thesis.

Chapter 2

$\mathcal{CP}$ Violation in the B system

2.1. Introduction

From a theoretical stand-point $\mathcal{CP}$ violation can be incorporated in the three generations of quarks of the Standard Model [8], but the model does not predict specific values for the $\mathcal{CP}$ violating parameters. Even though $\mathcal{CP}$ violation is observed in the K and B meson system we lack a fundamental understanding of its origins [9]. This is a critical gap in our knowledge since $\mathcal{CP}$ violation is a crucial ingredient in the current efforts to explain the observed matter-antimatter asymmetry [10]. It is now believed that it is not possible to explain the observed asymmetry based on the Standard Model alone, the parameters of the Standard Model must be fully examined. Such tests are the primary purpose of the *BABAR* experiment; the goal of which is to measure a set of $\mathcal{CP}$ parameters and to confirm or refute the ability of the Standard Model to accommodate these values.

2.2. The Meaning of Discrete Symmetries

For an operator acting on a quantum field to be physically meaningful to an inertial observer it must preserve the Minkowski interval $t^2 - \vec{x}^2$. Such quantities are known as Lorentz invariants. The set of continuous transformations that preserve this interval are the familiar Lorentz transformations that comprises the product space of rotations, translations, and Lorentz boosts. The three independent discrete transformations that also preserve $t^2 - \vec{x}^2$ are the charge conjugation operator (C), the parity operator (P), and the time-reversal operator (T).

2.2.1. Parity

The parity operator $\mathcal{P}$ sends $(t, \vec{x}) \rightarrow (t, -\vec{x})$, that is it reverses the signs of the three spatial elements of a four-vector. Thus it reverses the sign of the momentum of the particle ($(E, \vec{p}) \rightarrow (E, -\vec{p})$) but leaves the angular momentum ($\vec{x} \times \vec{p}$) unchanged. Parity can be visualized as a mirror-image operation plus an 180-degree rotation about a normal to the plane of the mirror as shown in Fig. 2.1.

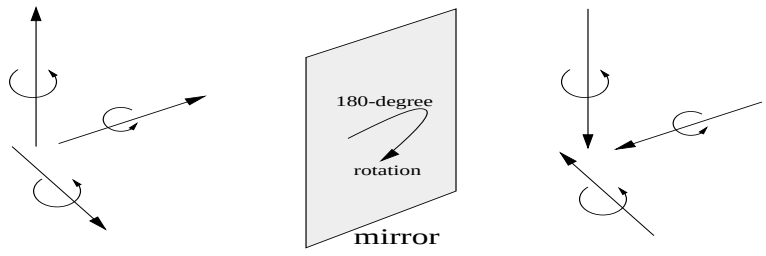

Figure 2.1: The parity operation :$(t, \vec{x}) \rightarrow (t, -\vec{x})$.

2.2.2. Time Reversal

The time reversal operator $\mathcal{T}$ sends $(t, \vec{x}) \to (-t, \vec{x})$ and $(E, \vec{p}) \to (-E, -\vec{p})$ thus it reverses momentum and spins, and also flips the sign of the time component of a state. This is shown schematically in Fig. 2.2.

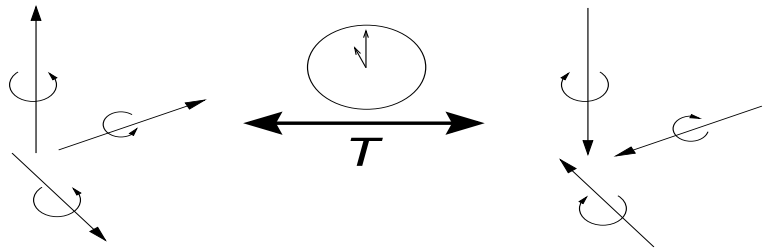

Figure 2.2: The time operation shown here that reverses the direction of the spin of a particle.

2.2.3. Charge Conjugation

The charge conjugate operator $\mathcal{C}$ transforms a particle into its anti-particle without changing position or momentum or spin of the particle.

2.2.4. Field Transformation of $\mathcal{P}$, $\mathcal{C}$, $\mathcal{T}$

The transformation properties of the various bilinear fields are summarized in Table. 2.1, [11]. The above $\mathcal{CP}$ transformation rules imply that each combination of fields that appear in the Lagrangian transforms under $\mathcal{CP}$ to its Hermitian conjugate. However there are coefficients in front of these expressions that represent either a

Table 2.1: Summary of the action of the $\mathcal{C}$, P, and T operators on bilinears of the Dirac field; $\tilde{x}^\mu = x_\mu$

Term (form)	$\mathcal{C}$	P	T	$\mathcal{CPT}$
Scalar:$S(x)$ $(\bar{\psi}(x)\psi(x))$	$S(x)$	$S(\tilde{x})$	$S(-\tilde{x})$	$S(-x)$
Pseudo-scalar: $P(x)$ $(\bar{\psi}(x)\gamma^5\psi(x))$	$P(x)$	-$P(\tilde{x})$	-$P(-\tilde{x})$	$P(-x)$
Vector: $V^\mu(x)$ $(\bar{\psi}(x)\gamma^\mu\psi(x))$	-$V^\mu(x)$	$V^\mu(\tilde{x})$	$V_\mu(-\tilde{x})$	-$V^\mu(-x)$
Pseudo-vector:$A^\mu(x)(\bar{\psi}\gamma^\mu\gamma^5\psi)$	$A^\mu(x)$	$-A^\mu(\tilde{x})$	$A_\mu(-\tilde{x})$	-$A^\mu(-x)$
Tensor:$T^{\mu\nu}(x)$ $(\bar{\psi}(x)[\gamma^\mu,\gamma^\nu]\psi(x))$	-$T^{\mu\nu}(x)$	$T_{\mu\nu}(\tilde{x})$	-$T_{\mu\nu}(-\tilde{x})$	$T^{\mu\nu}(-x)$

coupling constant or a particle mass. These coefficients are invariant under a $\mathcal{CP}$ transformation. If any of these quantities are complex the coefficients in front of the $\mathcal{CP}$ related term are complex conjugates of each other. In such a case $\mathcal{CP}$ is not necessarily a good symmetry of the Lagrangian. When the rates of a physical process that depend on these Lagrangian parameters are calculated, $\mathcal{CP}$ violating effects may introduce rate differences between pairs of $\mathcal{CP}$ conjugate processes.

The combined transformation $\mathcal{CPT}$ simultaneously performs time evolution, interchanging a particle into its anti-particle and a reflection of the space axis through the origin. There is a strong theoretical prejudice against the possibility of $\mathcal{CPT}$ violation [12]. The most basic consequence of $\mathcal{CPT}$ symmetry is the equality of the masses and lifetimes of a particle and its anti-particle. The best experimental test of $\mathcal{CPT}$ comes from the neutral kaon system by measuring [13].

$$|m_{K^0K^0} - m_{\bar{K}^0\bar{K}^0}| = (1.5 \pm 2.0) \times 10^{-18}\,\mathrm{GeV}/c^2. \tag{2.1}$$

From here on $\mathcal{CPT}$ symmetry is assumed.

2.3. Mixing of Neutral Mesons and their Time Evolution

The four pairs of conjugate neutral mesons that decay weakly, K^0, D^0, B_d^0, and B_s^0, can each mix with their respective anti-particle via a pair of "box" diagrams; Fig. 2.3. The ability to mix implies that the flavor eigenstates may not be equivalent to the mass eigenstates; the observed presence of mixing (into conjugate flavor-specific decays) implies that the mass and flavor eigenstates are in fact different. Lack of $\mathcal{CP}$ symmetry implies a third set of eigenstates, $\mathcal{CP}$ eigenstates, which could differ from the mass and flavor eigenstates, as will be shown.

2.3.1. Mixing of Neutral Mesons

Let us first consider the Schrodinger equation of motion for a single particle in its own rest frame. Omitting the spatial part we get:

$$-i\hbar\frac{\partial|\Psi\rangle}{\partial t} = E|\Psi\rangle. \tag{2.2}$$

setting ($\hbar = c = 1$) The solution is

$$|\Psi(t)\rangle \propto e^{-imt}|\Psi\rangle. \tag{2.3}$$

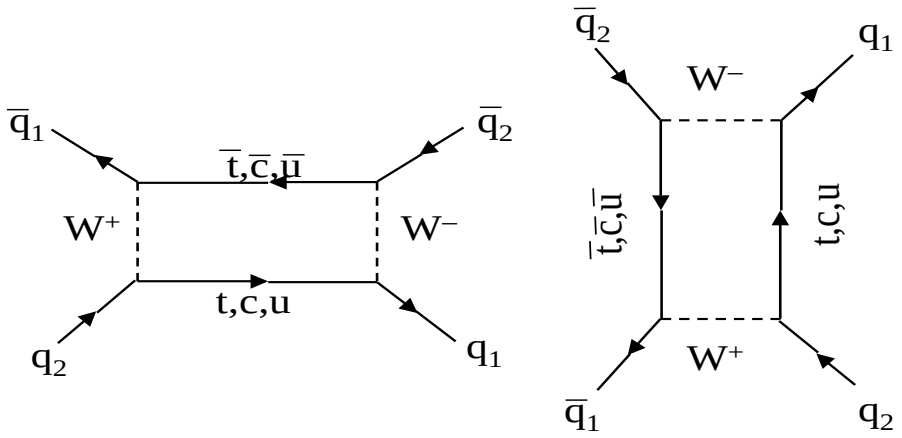

Figure 2.3: The two mixing diagrams, $\bar{q}_1, q_2$ can be either b, d, s quarks. These diagrams are called "box" diagrams.

Suppose the particle is unstable and its amplitude decays according to an exponential decay law with a decay constant of $\frac{\gamma}{2}$. Then

$$|\Psi(t)\rangle \propto e^{-imt} e^{\frac{-\gamma t}{2}} |\Psi\rangle \Rightarrow e^{-iAt}|\Psi\rangle. \tag{2.4}$$

Where $\mathcal{R}e(A) = m$ and $\mathcal{I}m(A) = \frac{-\gamma}{2}$ Now let us consider a system made of two states such that

$$|\Psi(t)\rangle = \alpha|X^0\rangle + \beta|\bar{X}^0\rangle. \tag{2.5}$$

The time evolution given is given by:

$$i\frac{\partial}{\partial t}\begin{pmatrix}\alpha\\ \\ \beta\end{pmatrix} = \mathcal{H}\begin{pmatrix}\alpha\\ \\ \beta\end{pmatrix} \equiv \begin{pmatrix} m_{11}-\frac{1}{2}i\gamma_{11} & m_{12}-\frac{1}{2}i\gamma_{12}\\ \\ m_{21}-\frac{1}{2}i\gamma_{21} & m_{22}-\frac{1}{2}i\gamma_{22}\end{pmatrix}\begin{pmatrix}\alpha\\ \\ \beta\end{pmatrix}. \tag{2.6}$$

The m and γ parts represent the mass and decay width, respectively, of the time dependence. Each of the off-diagonal elements can be complex. Thus a state that starts off as a pure $|X^0\rangle$ after some time is an admixture of the two states. If the state $|X^0\rangle$ and $|\bar{X}^0\rangle$ are the particle and anti-particle of each other then according to $\mathcal{CPT}$ invariance $m_{11} = m_{22} = m$, $\gamma_{11} = \gamma_{22} = \gamma$ and $m_{21} = m_{12}^*$, $\gamma_{21} = \gamma_{21}^*$. Therefore the equation of motion becomes:

$$i\frac{\partial}{\partial t}\begin{pmatrix}\alpha\\ \\ \beta\end{pmatrix} = \begin{pmatrix} m-\frac{1}{2}i\gamma & m_{12}-\frac{1}{2}i\gamma_{12}\\ \\ m_{12}^*-\frac{1}{2}i\gamma_{12}^* & m-\frac{1}{2}i\gamma\end{pmatrix}\begin{pmatrix}\alpha\\ \\ \beta\end{pmatrix}. \tag{2.7}$$

The Schrodinger equation is best solved by diagonalizing the matrix [14]. The solution yields two decoupled equations to represent the two mass eigenstates given by

$$\begin{aligned}|X_L\rangle &= p|X^0\rangle + q|\bar{X}^0\rangle\\ |X_H\rangle &= p|X^0\rangle - q|\bar{X}^0\rangle.\end{aligned} \tag{2.8}$$

where q and p obey the normalization condition

$$|p|^2 + |q|^2 = 1. \tag{2.9}$$

The eigenvalues for the eigenstates $|X_L\rangle$ and $|X_R\rangle$ are given by

$$\begin{aligned} M_H - \frac{i}{2}\Gamma_H &= m - \frac{i}{2}\gamma + \frac{q}{p}(m_{12} - \frac{i}{2}\gamma_{12}), \\ M_L - \frac{i}{2}\Gamma_L &= m - \frac{i}{2}\gamma - \frac{q}{p}(m_{12} - \frac{i}{2}\gamma_{12}). \end{aligned} \tag{2.10}$$

The observables are

$$\begin{aligned} M_H - M_L = \Delta m &= -2Re(\frac{q}{p}(m_{12} - \frac{i}{2}\gamma_{12})), \\ \Gamma_H - \Gamma_L = \Delta\Gamma &= 4\mathcal{I}m(\frac{q}{p}(m_{12} - \frac{i}{2}\gamma_{12})). \end{aligned} \tag{2.11}$$

$$\begin{aligned} \frac{q}{p} &= \pm\sqrt{\frac{m_{12}^* - \frac{i}{2}\gamma_{12}^*}{m_{12} - \frac{i}{2}\gamma_{12}}}, \\ \text{or} \qquad \frac{q}{p} &= \frac{\Delta m - \frac{i}{2}\Delta\Gamma}{2(m_{12} - \gamma_{12})}. \end{aligned} \tag{2.12}$$

An initially pure $|X^0\rangle$ state will, therefore, time evolve as a superposition of the mass eigenstates $|X_L\rangle$ and $|X_H\rangle$. The time-evolution can be fully expressed in terms of the

physically intuitive quantities m, Γ, Δm, and $\Delta\Gamma$.

$$|X^0(t)\rangle = g_+(t)|X^0\rangle + (q/p)g_-(t)|\bar{X}^0\rangle,$$
$$|\bar{X}^0(t)\rangle = (p/q)g_-(t)|X^0\rangle + g_+(t)|\bar{X}^0\rangle. \tag{2.13}$$

where

$$g_+(t) = e^{-imt}e^{-\Gamma t/2}(e^{-i\Delta mt/2}e^{-\Delta\Gamma t/2} + e^{+i\Delta mt/2}e^{+\Delta\Gamma t/2}) \tag{2.14}$$

$$g_-(t) = e^{-imt}e^{-\Gamma t/2}(e^{-i\Delta mt/2}e^{-\Delta\Gamma t/2} - e^{+i\Delta mt/2}e^{+\Delta\Gamma t/2}). \tag{2.15}$$

2.3.2. The Neutral B System

In the case of the neutral B^0 meson the theoretical expectation [15] for the ratio $\Delta\Gamma$ to Γ.

$$\frac{\Delta\Gamma}{\Gamma} = \mathcal{O}(10^{-2}). \tag{2.16}$$

In fact $\Delta\Gamma_B$ has yet to be measured experimentally. On the other hand Δm has been measured by *BABAR* [16] to be 3.37×10^{-13} GeV/c^2, a factor of 13 orders of magnitude smaller than the mass of the B, 5.27 GeV/c^2. The ratio [17]

$$\frac{\Delta m_B}{\Gamma_B} = 0.723 \pm 0.032. \tag{2.17}$$

From Eq. 2.16 and Eq. 2.17 one learns that [15],

$$\Delta m_B >> \Delta\Gamma_B. \tag{2.18}$$

Taking into account these observations the time evolution of the neutral B meson Eq. 2.13 simplifies to

$$|B^0_{phys}(t)\rangle = g_+(t)|B^0\rangle + (q/p)g_-(t)|\overline{B}^0\rangle. \tag{2.19}$$

$$|\overline{B}^0_{phys}(t)\rangle = g_+(t)|\overline{B}^0\rangle + (p/q)g_-(t)|B^0\rangle. \tag{2.20}$$

where

$$g_+(t) = e^{-imt}e^{-\Gamma t/2}\cos(\Delta m t/2). \tag{2.21}$$

$$g_-(t) = e^{-imt}e^{-\Gamma t/2} i\sin(\Delta m t/2). \tag{2.22}$$

A state which is created at time $t = 0$ as a pure B^0 system, evolves in time as a mixture of B^0 and $\overline{B}^0$ and is denoted as B^0_{phys}. The evolution of a pure $\overline{B}^0$ state at time $t = 0$ is denoted as $\overline{B}^0_{phys}$.

2.4. Time Formalism for Coherent $B\overline{B}$ States

This section considers the consequences of producing neutral $B\overline{B}$ meson pairs in an e^+e^- collider at the $\Upsilon(4S)$ resonance. In this situation the B^0 and the $\bar{B}^0$ mesons

are produced in a coherent state of angular momentum, $L = 1$. Each of these particles evolves in time as described in Sec. 2.3.2. However they evolve in phase such that up to when one decays there is always one B^0 and one $\overline{B}^0$ present. After one of them has decayed the constraint no longer applies and the other particle continues to evolve independently until it decays. Thus it is possible to find events with two B^0 or two $\bar{B}^0$, at a rate whose probability is governed by the time between the two decays.

2.5. Types of $\mathcal{CP}$ Violation in B Decays

There are three main types of $\mathcal{CP}$ violation in the B system. $\mathcal{CP}$ violation is possible only when there is an interference between at least two phases. In the charged B system only $\mathcal{CP}$ violation in decay is possible.

2.5.1. $\mathcal{CP}$ Violation in Decay

Let A_f and $\bar{A}_{\bar{f}}$ represent the amplitude of the decay of B and $\bar{B}$ to decay into final states f and $\bar{f}$. The quantity $\left|\frac{\bar{A}_{\bar{f}}}{A_f}\right|$ is phase-convention independent and is physically meaningful.

There are two types of phases present in the amplitudes A_f and $\bar{A}_{\bar{f}}$.

The complex parameters of the Lagrangian contributing to the amplitude will appear as complex conjugates in the $\mathcal{CP}$ conjugate decay amplitude. This means that the phases will appear in A_f and $\bar{A}_{\bar{f}}$ with opposite sign. In the Standard Model,

such phases enter only via the electroweak sector of the theory, that is, through the Cabbibo Kobayashi Maskawa (CKM) mass mixing matrix, and are often called "weak" phases. The second type of phase arises due to strong interactions and are called "strong" phase. They appear in the two amplitudes with the same sign and in general do not violate $\mathcal{CP}$. The phase of any one term is convention dependent and hence a meaningless quantity, but the difference between the phases is convention independent and hence is a meaningful quantity.

The amplitude of a decay process can be written as a sum of three components, its magnitude A, its weak phase $e^{i\phi}$ and its strong phase $e^{i\delta}$. Then if several amplitudes represented by decay graphs contribute to the process $B \to f$, the amplitude A_f is written as

$$A_f = \sum_i A_i e^{i(\delta_i + \phi_i)}. \tag{2.23}$$

the corresponding phase independent quantity is

$$\left|\frac{\bar{A}_{\bar{f}}}{A_f}\right| = \left|\frac{\sum_i A_i e^{i\delta_i - \phi_i}}{\sum_i A_i e^{i\delta_i + \phi_i}}\right|. \tag{2.24}$$

Thus if the phases of the amplitudes are not the same then the two amplitudes will be different, leading to $\mathcal{CP}$ non-conservation. Thus the condition for $\mathcal{CP}$ conservation is

$$\left|\frac{\bar{A}_{\bar{f}}}{A_f}\right| = 1. \tag{2.25}$$

The deviation from equality is known as $\mathcal{CP}$ violation in decay or "direct" $\mathcal{CP}$ violation. Thus direct $\mathcal{CP}$ violation only occurs if two terms with differing weak phases acquire different strong phases [15]:

$$|A|^2 - |\bar{A}|^2 = -2\sum_{i,j} A_i A_j \sin(\phi_i - \phi_j)\sin(\delta_i - \delta_j). \tag{2.26}$$

Furthermore the rate asymmetry can be expressed in terms of the decay amplitudes:

$$a_f = \frac{1 - |\bar{A}/A|^2}{1 + |\bar{A}/A|^2}. \tag{2.27}$$

The most compelling evidence of $\mathcal{CP}$ violation in decay has been observed in the kaon system at the Na48 experiment [4] at CERN and the KTeV experiment [5] at Fermilab. Direct $\mathcal{CP}$ violation is yet to be seen in the B system. Since the strong phases that enter into measurements of $\mathcal{CP}$ violation in decay involve hadronic uncertainties (which arise due to QCD gluon exchange where perturbative or symmetry arguments can not be used), the relation of such measurements to CKM factors (see next section) cannot be calculated from first principles, but the strong phases may themselves be measured if the CKM factors are known from other measurements. These strong phase measurements can then be used as an input to other measurements that have equivalent strong phases (thus allowing the extraction of other parameters). Thus measurements of $\mathcal{CP}$ violation in decay can, indirectly, provide a useful handle on

fundamental quantities.

This is the only kind of $\mathcal{CP}$ violation that can occur in the charged B system.

2.5.2. $\mathcal{CP}$ Violation Purely in Mixing

From section. 2.3 recall that the mass eigenstates of the neutral meson system are the eigenvectors of the Hamiltonian

$$\begin{aligned} |X_L\rangle &= p|X^0\rangle + q|\bar{X}^0\rangle, \\ |X_H\rangle &= p|X^0\rangle - q|\bar{X}^0\rangle. \end{aligned} \tag{2.28}$$

where

$$q = \sqrt{\frac{m_{12}^* - \frac{1}{2}i\gamma_{12}^*}{m_{12} - \frac{1}{2}i\gamma_{12}}}p. \tag{2.29}$$

If $\mathcal{CP}$ was conserved quantity then $m_{21} = e^{-i2\eta}m_{12}$ and $\gamma_{21} = e^{-i2\eta}\gamma_{12}$ where η is some arbitrary phase. Thus from Eq. 2.29 we have

$$\frac{q}{p} = e^{-i\eta}. \tag{2.30}$$

If $\mathcal{CP}$ is violated :

$$\begin{aligned} \left|\frac{q}{p}\right| &\neq 1, \\ q &\neq e^{-i\eta}p. \end{aligned} \tag{2.31}$$

This implies that q and p have different magnitudes and the $\mathcal{CP}$ conjugates of the mass eigenstates clearly will differ from the mass eigenstates themselves by more than a trivial phase. Thus the mass eigenstates will not be $\mathcal{CP}$ eigenstates and $\mathcal{CP}$ violation will be manifest. It is purely an effect of mixing and is independent of decay mode. Thus it may be referred to as $\mathcal{CP}$ violation purely in mixing or as "indirect" $\mathcal{CP}$ violation.

This type of $\mathcal{CP}$ violation has been observed in the neutral kaon system [2]; the discovery of $\mathcal{CP}$ violation in 1964 was a detection of $\mathcal{CP}$ violation purely in mixing. In the neutral B system this can be measured by studying semi-leptonic decays as they are dominated by a single decay graph and the only way $\mathcal{CP}$ violation can enter is through mixing. Thus

$$a_{sl} = \frac{\Gamma(B^0_{phys}(t) \to l^- \nu X) - \Gamma(\overline{B}^0_{phys}(t) \to l^+ \nu X)}{\Gamma(B^0_{phys}(t) \to l^- \nu X) + \Gamma(\overline{B}^0_{phys}(t) \to l^+ \nu X)}. \tag{2.32}$$

or in terms of $|q/p|$

$$a_{sl} = \frac{1 - |q/p|^4}{1 + |q/p|^4}. \tag{2.33}$$

As discussed in Sec. 2.3.2 such effects are expected to be very small, since

$$\Delta m = \mathcal{O}(10^3)\Delta\Gamma. \tag{2.34}$$

this implies that

$$|m_{12}| \gg |\gamma_{12}|. \tag{2.35}$$

In the neutral B system $\mathcal{CP}$ violation purely in mixing is expected to be at a 10^{-3} level. Moreover, it is difficult to calculate $|q/p|$ as it requires calculation of γ_{12} and m_{12}, which involve large hadronic uncertainties [18].

2.5.3. $\mathcal{CP}$ Violation in the Interference Between Decays of Mixed and Unmixed Mesons

The final states, f and $\bar{f}$, that may be reached from either B^0 or $\overline{B}^0$ decays can exhibit a third type of $\mathcal{CP}$ violation, which results from the interference between the decays of mixed and unmixed neutral B mesons that both decay to the same final state. Here, the physically meaningful phase convention independent quantity is:

$$\lambda \equiv \frac{q}{p}\frac{\bar{A}_f}{A_f} = \eta_f \frac{q}{p}\frac{\bar{A}_{\bar{f}}}{A_{\bar{f}}}. \tag{2.36}$$

where $\eta_f(\pm 1)$ is the $\mathcal{CP}$ eigenvalue of the state f and

$$\bar{A}_f = \eta_f \bar{A}_{\bar{f}}. \tag{2.37}$$

If $|q/p| = 1$ and $|\bar{A}_f/A_f| = 1$ then $|\lambda| = 1$ and $\mathcal{CP}$ is conserved in mixing and decay separately. But if

$$arg(\lambda_f) \neq 0 \tag{2.38}$$

there is a relative phase between mixing and decay, and $\mathcal{CP}$ is not conserved in the interference between mixing and decay. To see this last point consider the following: The amplitudes of the decay for the time evolved neutral B meson is from Eq. 2.20 can be written as

$$\begin{aligned} |\langle f|\mathcal{H}|B^0_{phys}(t)\rangle| &= A_f\left(g_+(t) + \lambda g_-(t)\right), \\ |\langle f|\mathcal{H}|\overline{B}^0_{phys}(t)\rangle| &= A_f\frac{p}{q}\left(g_-(t) + \lambda g_+(t)\right). \end{aligned} \tag{2.39}$$

This gives

$$\begin{aligned} \Gamma(B^0_{phys}(t) \to f) = \; |\langle f|\mathcal{H}|B^0_{phys}(t)\rangle|^2 \quad &= \quad |A_f|^2\Big[e^{-\Gamma t}\cos^2(\frac{\Delta m t}{2}) + e^{-\Gamma t}|\lambda|^2\sin^2(\frac{\Delta m t}{2}) \\ &+ \quad ie^{-\Gamma t}\lambda\cos(\frac{\Delta m t}{2})\sin(\frac{\Delta m t}{2}) \\ &- \quad ie^{-\Gamma t}\lambda^*\cos(\frac{\Delta m t}{2})\sin(\frac{\Delta m t}{2})\Big], \\ &= \quad |A_f|^2 e^{-\Gamma t}\Big[\frac{1+|\lambda|^2}{2} - \frac{1-|\lambda|^2}{2}\cos(\Delta m t) \\ &\quad -\mathcal{I}m(\lambda)\sin(\Delta m t)\Big]. \end{aligned} \tag{2.40}$$

Where $\mathcal{I}m(\lambda)$ is the imaginary part of λ Similarly,

$$\Gamma(\overline{B}^0_{phys}(t) \to f) = |\langle f|\mathcal{H}|\overline{B}^0_{phys}(t)\rangle|^2 \quad = \quad |A_f|^2 e^{-\Gamma t}\Big[\frac{1+|\lambda|^2}{2} - \frac{1-|\lambda|^2}{2}\cos(\Delta m t) + \mathcal{I}m(\lambda)\sin(\Delta m t)\Big]. \tag{2.41}$$

where the approximation $|q/p| = 1$ has been used. If one now forms the difference of these rates divided by the sum, the time dependent $\mathcal{CP}$ asymmetry is given by

$$a_f(t) = ng\frac{\Gamma(B^0_{phys}(t) \to f) - \Gamma(\bar{B}^0_{phys}(t) \to f)}{\Gamma(B^0_{phys}(t) \to f) + \Gamma(\bar{B}^0_{phys}(t) \to f).} \tag{2.42}$$

Where ng is the $\mathcal{CP}$ eigenvalue taking values ± 1 and is obtained from experiment. Thus giving

$$a_f(t) = \frac{(1-|\lambda|^2)\cos(\Delta m t) - 2\mathcal{I}m(\lambda)\sin(\Delta m t)}{1+|\lambda|^2}. \tag{2.43}$$

which is non zero if any of the three types of $\mathcal{CP}$ violation are present. However, in the absence of $\mathcal{CP}$ violation in decay and mixing, $|\lambda| = 1$ the asymmetry reduces to

$$a_f(t) = -\mathcal{I}m(\lambda)\sin(\Delta m t). \tag{2.44}$$

where t is the difference between the decay times of the two B meson, $t_f - t_{ftag}$. This type of $\mathcal{CP}$ violation is called $\mathcal{CP}$ violation in the interference between the decays with

and without mixing.

2.5.4. Summary

There are three types of $\mathcal{CP}$ violation in the B system .

1: $\mathcal{CP}$ violation in decay or direct $\mathcal{CP}$ violation: This occurs whenever the magnitude of the amplitude of a decay is not the same as its $\mathcal{CP}$ conjugate. This is the only type of $\mathcal{CP}$ violation in the charged B meson sector. It requires the presence of at least two interfering amplitudes with different weak and strong phases, $|\bar{A}_f/A_f| \neq 1$

2: $\mathcal{CP}$ violation in mixing or indirect $\mathcal{CP}$ violation: This occurs when $|q/p| \neq 1$.

3: $\mathcal{CP}$ violation in interference and decay: This occurs only when the final state is common to both the particle and its anti-particle and is due to the interference between direct decay and a decay when the B^0 meson gets mixed into its anti-particle $\overline{B}^0$ meson and then subsequently decays into the same final state f. $\mathcal{CP}$ violation in interference and decay requires $arg(\lambda) \neq 0$.

2.6. $\mathcal{CP}$ Violation in the Standard Model

$\mathcal{CP}$ violation within the context of the Standard Model $SU(2) \times U(1)$ electroweak symmetry was introduced by Kobayashi and Maskawa in 1973 with the postulation of a third family of quarks. The b-quark was first observed in 1977. The development of the 3×3 CKM matrix and its $\mathcal{CP}$ violating phase was a steady and piecewise

process. More detailed information can be found in references [9] and [19].

2.6.1. Weak Interactions and the CKM Matrix

Rochester and Butler in October of 1947 discovered the K^0 meson through its decay to two charged π [21]. Later in 1955 the Λ hyperon was discovered through its decay to a proton and a π. The lifetime of the Λ hyperon is 10^{-10} seconds which is large compared to strong transition of about 10^{-23}. These discoveries led to the puzzle that the production rate of these particles far exceeded the decay rate. Thus it was found experimentally that strangeness-changing decays are suppressed compared with strangeness-conserving weak decays. To account for the decay of strange particles in 1963 Cabbibo introduced quark mixing angle, now known as the Cabibbo angle [22]. In order to supress strangness changing neutral currents Glashow, Iliopoulous and Maiani (GIM) proposed the existence of the c quark some years before its discovery. To calculate the $K^0\bar{K}^0$ mixing Lee and Gaillard [20] predicted the mass of the c quark from the box diagram. Due to this mixing the mass eigenstates differ from the weak eigenstates. The mixing matrix is used to describe transitions between quark generations

Such a matrix must be unitary since quark number is manifestly conserved. With

two generations, a unitary matrix can be described by a single parameter Θ_c:

$$\begin{pmatrix} d_{mass} \\ \\ s_{mass} \end{pmatrix} = \begin{pmatrix} \cos\Theta_c & \sin\Theta_c \\ \\ -\sin\Theta_c & \cos\Theta_c \end{pmatrix} \begin{pmatrix} d \\ \\ s \end{pmatrix}. \tag{2.45}$$

where d_{mass} and s_{mass} are the mass eigenstates while d and s are the flavor eigenstates. The Cabbibo angle Θ_c is thus a full description of two-generation mixing. More generally, we can write the charged-current coupling j_{cc} with two generations as

$$j^{\mu}_{cc} = \begin{pmatrix} \bar{u} & \bar{c} \end{pmatrix} \gamma^{\mu}(1-\gamma^5) \begin{pmatrix} d_{mass} \\ \\ s_{mass} \end{pmatrix} = \begin{pmatrix} \bar{u} & \bar{c} \end{pmatrix} \gamma^{\mu}(1-\gamma^5) V_{ij} \begin{pmatrix} d \\ \\ s \end{pmatrix}. \tag{2.46}$$

where V_{ij} is the 2×2 Cabbibo matrix parameterized by Θ_c above. With an arbitrary number of generations, the charged current ($W^{\pm}$) Lagrangian becomes:

$$\mathcal{L}_W = \frac{g}{\sqrt{2}} \left\{ \bar{u}^L_i \gamma^{\mu} W^+_{\mu} V_{ij} d^L_j + \bar{d}^L_i \gamma^{\mu} W^-_{\mu} V^*_{ij} u^L_j \right\}. \tag{2.47}$$

with u^L_i representing the vector of up-type quarks and d^L_i representing the down-type quarks. Applying the $\mathcal{CP}$ operation to the Lagrangian, one obtains:

$$CP(\mathcal{L}_W) = \frac{g}{\sqrt{2}} \left\{ \bar{d}^L_i \gamma^{\mu} W^-_{\mu} V_{ij} u^L_j + \bar{u}^L_i \gamma^{\mu} W^+_{\mu} V^*_{ij} d^L_j \right\}. \tag{2.48}$$

This is exactly the same except for the complex conjugation of V. Thus, if we can find a basis for which V (as well as the quark masses) are real, then $\mathcal{CP}$ is a symmetry.

Unitary matrices of dimension N form a group, the Lie group $SU(N)$ [9]. An orthogonal $N \times N$ matrix has $\frac{N(N-1)}{2}$ real parameters and $\frac{(N-1)(N-2)}{2}$ phases. Thus for two generations of quarks there is only one real parameter, the Cabbibo angle Θ_c. For three generations of quarks there are three real parameters and one complex phase. If this phase is not an integer multiple of π then we can no longer find a basis in which V is real and $\mathcal{CP}$ will no longer be a good symmetry.

2.6.2. Unitarity Conditions and the Unitarity Triangle

Unitarity of the CKM matrix V requires that

$$V^\dagger V = V V^\dagger = 1 \quad \Rightarrow \quad \sum_j V_{ji}^* V_{jk} = \sum_j V_{ij} V_{kj}^* = \quad \delta_{ik}. \tag{2.49}$$

With a 3-generation CKM matrix given by V as:

$$V = \begin{pmatrix} V_{ud} & V_{us} & V_{ub} \\ V_{cd} & V_{cs} & V_{cb} \\ V_{td} & V_{ts} & V_{tb} \end{pmatrix}. \tag{2.50}$$

2. $\mathcal{CP}$ Violation in the B system

A convenient parameterization of the CKM matrix can be made in terms of four Wolfenstein parameters, [23], λ, A, ρ, η with $\lambda = \sin(\Theta_c)$ playing the role of the expansion parameter and η representing the $\mathcal{CP}$ violating parameter.

$$V = \begin{pmatrix} 1 - \frac{\lambda^2}{2} & \lambda & A\lambda^3(\rho - i\eta) \\ -\lambda & 1 - \frac{\lambda^2}{2} & A\lambda^2 \\ A\lambda^3(1 - \rho - i\eta) & -A\lambda^2 & 1 \end{pmatrix} + \mathcal{O}(\lambda^4). \tag{2.51}$$

The unitarity of the CKM matrix produces certain relation among its elements. Three of these equations are useful for understanding $\mathcal{CP}$ violation in the standard model :

$$V_{us}^* V_{ud} + V_{cs}^* V_{cd} + V_{ts}^* V_{td} = 0 \tag{2.52}$$

$$V_{ub}^* V_{us} + V_{cb}^* V_{cs} + V_{tb}^* V_{ts} = 0 \tag{2.53}$$

$$V_{ub}^* V_{ud} + V_{cb}^* V_{cd} + V_{tb}^* V_{td} = 0 \tag{2.54}$$

These expressions require the sum of the three complex numbers to vanish and can be represented as a triangle in the complex plane. The area of all these three triangles is the same and is directly proportional to the amount of $\mathcal{CP}$ violation [24]. The third equation is the most interesting because all the sides of the triangle are of the same

order of magnitude, λ^3 and the angles are larger compared to the other two triangles. This triangle is used in the study of the B_d system and is commonly referred to as the *unitarity* triangle.

It is useful to show this triangle in a rescaled form. Since $V_{cb}^* V_{cs}$ is a real quantity this side lies along the horizontal axis and is taken to be of unit length, as shown in Fig. 2.4. The apex of this triangle lies at (ρ, η) and the three angles labeled α, β and

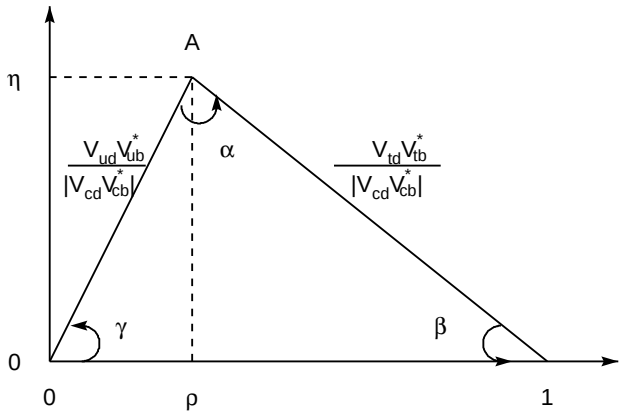

Figure 2.4: The rescaled Unitarity Triangle where all the sides have been divided by $|V_{cb}^* V_{cs}|$ and the CKM angles.

γ are given by

$$\alpha \equiv arg\Big[-\frac{V_{td}V_{tb}^*}{V_{ud}V_{ub}^*}\Big], \quad \beta \equiv arg\Big[-\frac{V_{cd}V_{cb}^*}{V_{td}V_{tb}^*}\Big], \quad \gamma \equiv arg\Big[-\frac{V_{ud}V_{ub}^*}{V_{cd}V_{cb}^*}\Big]. \tag{2.55}$$

The sides and the angles are physical quantities. The angles are extracted from time-dependent asymmetries and the sides are measurable from semi-leptonic branching fractions. A theoretical error is associated with the extraction of the CKM parameters. By doing redundant measurements on the sides and the angles one looks for violation of the conditions of unitarity in the three generation theory.

2.7. Extraction of $\sin(2\beta+\gamma)$ in the B^0 System

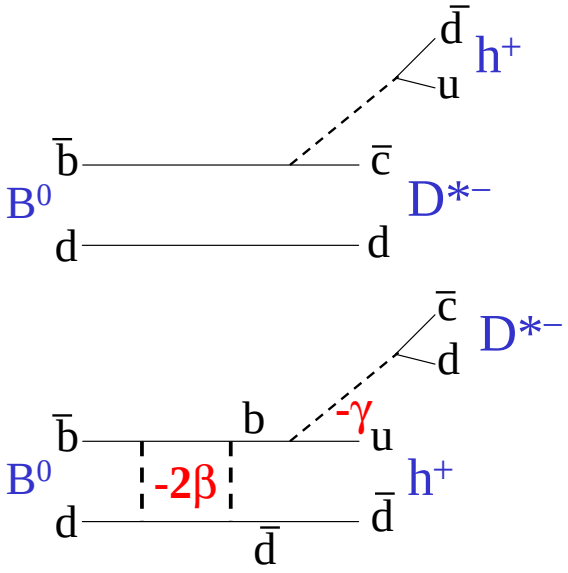

Figure 2.5: The Feynman diagram represent the two possible decay models of $B^0 \to D^{*-}h^+$.

The final states $D^{*-}h^+$ where h can be $\pi, \rho, a1$ meson can be produced both in the B^0 and $\overline{B}^0$ decays as shown in Fig. 2.5. The $B^0 \to D^{*-}\rho^+$ mode has been studied in detail in [26]. The interference through mixing and decay leads to $\mathcal{CP}$ violation.

Recall that

$$\lambda = \frac{q}{p}\frac{\bar{A}}{A} \quad = \frac{q}{p}\frac{\bar{A}(\overline{B}^0 \to f)}{A(B^0 \to f)}. \tag{2.56}$$

The $\frac{q}{p}$ part comes from the B^0 mixing process as shown by the bottom diagram in fig. 2.5 and is given by

$$\frac{q}{p} = e^{-2i\beta}. \tag{2.57}$$

At present the most precisely measured CKM angle is the angle β. It is determined using modes such as $B^0 \to J/\Psi K_s^\circ$. The value as measured by the *BABAR* experiment is [25] $\sin(2\beta) = 0.79 \pm 0.11$.

For the decays $B^0 \to D^* h$, λ is given by

$$\begin{aligned} \lambda_{D^{*+}h^-} &= \frac{q}{p}\frac{V_{ud}^* V_{cb}}{V_{cd}^* V_{ub}}\frac{\bar{M}_f}{M_f} = \quad \frac{1}{|\lambda_{D^{*+}h^-}|}e^{-i(2\beta+\gamma)}, \\ \lambda_{D^{*-}h^+} &= \frac{q}{p}\frac{V_{ub}^* V_{cd}}{V_{cb}^* V_{ud}}\frac{\bar{M}_{\bar{f}}}{M_{\bar{f}}} = \quad |\lambda_{D^{*-}h^+}|e^{-i(2\beta+\gamma)}. \end{aligned} \tag{2.58}$$

Where $\bar{M}_f, M_f$ are the strong hadronic matrix elements.

As seen from Eq. 2.58 the decay $B^0 \to D^{*+}h^-$ is suppressed by a factor λ^2 compared to the Cabibbo allowed mode of $B^0 \to D^{*-}h^+$, hence a lot of events are needed to do a significant measurement of $2\beta + \gamma$. This can be done using partial

reconstruction techniques described in Chapter 3.

Thus if one measures the corresponding $\mathcal{CP}$ asymmetries, both $\lambda(B \to f)$ and $\lambda(B \to \bar{f})$ can be determined up to discrete ambiguities (due to the unknown strong phases) providing for a theoretically clean determination of $2\beta + \gamma$ from

$$\lambda(B \to f)\lambda(B \to \bar{f}) = e^{-2i(2\beta+\gamma)}. \tag{2.59}$$

Since 2β is measured from other measurements, one can extract γ.

Chapter 3

The *BABAR* Detector

3.1. Introduction

The *BABAR* detector at SLAC was designed and built by a large international team of scientists and engineers, including members of the Colorado State University High Energy Physics group. A detailed description of the *BABAR* detector and PEP-II can be found in [15; 28; 59]. In this chapter we shall provide an overview of PEP-II and the various sub-detectors of *BABAR*. All figures in this chapter are taken from [28]. As the author had direct experience and operational responsibility of the DIRC sub-system, we provide a more detailed description of it in Appendix A.

The primary motivation for constructing an asymmetric B-factory at the PEP-II electron (e^-) and positron (e^+) storage ring operating at the $\Upsilon(4S)$ resonance, is to probe the Standard Model.

Even though the expected $\mathcal{CP}$ asymmetries in the Standard Model for the B meson system are large the branching fractions of the channels used in the measurement are only on the order of 10^{-4}. This places challenging requirements on the accelerator and the detector. The accelerator must provide a very high luminosity with low backgrounds. After three years of operation, the PEP-II design luminosity of $3 \times 10^{33}\,\mathrm{cm}^{-2}\mathrm{s}^{-1}$ has been achieved and surpassed. The detector was required to have a large and uniform acceptance, charged particle tracking down to a momentum transverse to the beam direction, p_t, approximately 60 MeV/c, detection of photons over a range of roughly 20 MeV $< E <$ 5 GeV, particle identification, particularly of kaons and pions up to 4 GeV, and a very good vertex resolution, both in the transverse and parallel direction to the beam. Though the design of the detector was optimized for $\mathcal{CP}$ measurements it has proven to be well suited for other physics topics as well.

3.2. PEP-II and the Interaction Region (IR)

PEP-II [1] is an e^+e^- storage ring. The High Energy Ring (HER) stores 9 GeV electrons and the Low Energy Ring (LER) stores 3.1 GeV positrons. Thus PEP-II operates at a center of mass energy of 10.58 GeV, the mass of the $\Upsilon(4S)$ resonance which is moving with respect to the laboratory frame. The cross-section for the

[1] PEP is an acronym for Positron Electron Project

production of fermion pairs at the $\Upsilon(4S)$ is shown in Table. 3.1. Approximately 12 % of the data are taken 40 MeV below the peak of the resonance to provide a sample of non-resonant background called continuum, ($e^+e^- -> q\bar{q}$, where $q = u, d, s, c$).

Table 3.1: Production cross-sections at the $\Upsilon(4S)$ resonance.

$e^+e^- \rightarrow$	Cross-section (nb)
$b\bar{b}$	1.05
$c\bar{c}$	1.30
$s\bar{s}$	0.35
$u\bar{u}$	1.39
$d\bar{d}$	0.35
$\tau^+\tau^-$	0.94
$\mu^+\mu^-$	1.16
e^+e^-	~ 40

The asymmetric energies produce a boost of $\beta\gamma = 0.56$ in the laboratory frame for the resulting B meson. As a consequence, the decay points of the B mesons produced in the $\Upsilon(4S)$ resonance are separated by approximately 250 μm on average along the beam axis, taken as the z axis in the *BABAR* coordinate system. Selecting the boost for an optimal physics performance required balancing two conflicting effects: a) The average B decay vertex separation in z is related to $\gamma\beta c\tau$, where τ is the lifetime of the B. Thus increasing the boost would result in an increase in the separation of the B decay vertex making it easier to resolve the two decay vertices. b) However, the greater the boost the tracks will all be boosted in the forward direction therevy

worsening the z resolution. Also choosing too large a boost would degrade the physics performance by allowing too many particles to escape undetected through the dead region.

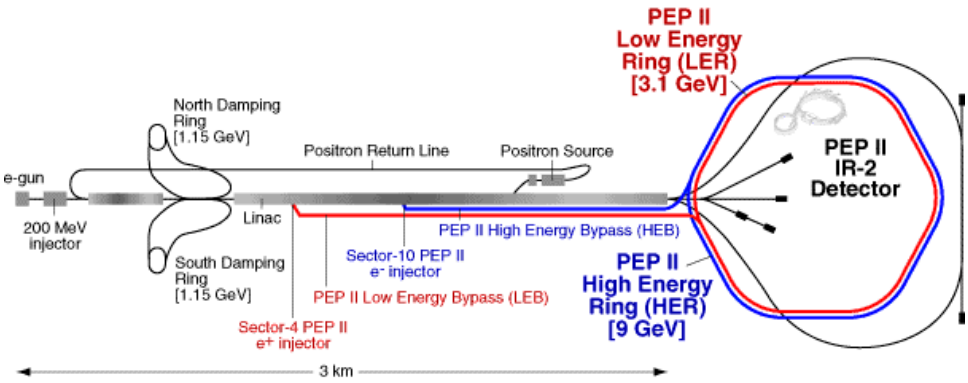

Figure 3.1: A schematic representation of the acceleration and storage system at the PEP-II.

A schematic representation of the acceleration and the storage system is shown in Fig. 3.1. An electron gun is used to create two electron bunches that are accelerated to approximately 1 GeV before entering one of the damping rings, whose purpose is to reduce the dispersion in the beams. After that those electrons are accelerated in the Linac. The other bunch is diverted to collide with a tungsten target and to create a positron beam, which in turn passes through the damping ring and is accelerated in the Linac.

On reaching the design energies at the end of the Linac, the electron and the positron beams are fed into the PEP-II storage rings, here they collide at the interaction region as shown in Fig. 3.2. A primary impediment to achieve currents of the

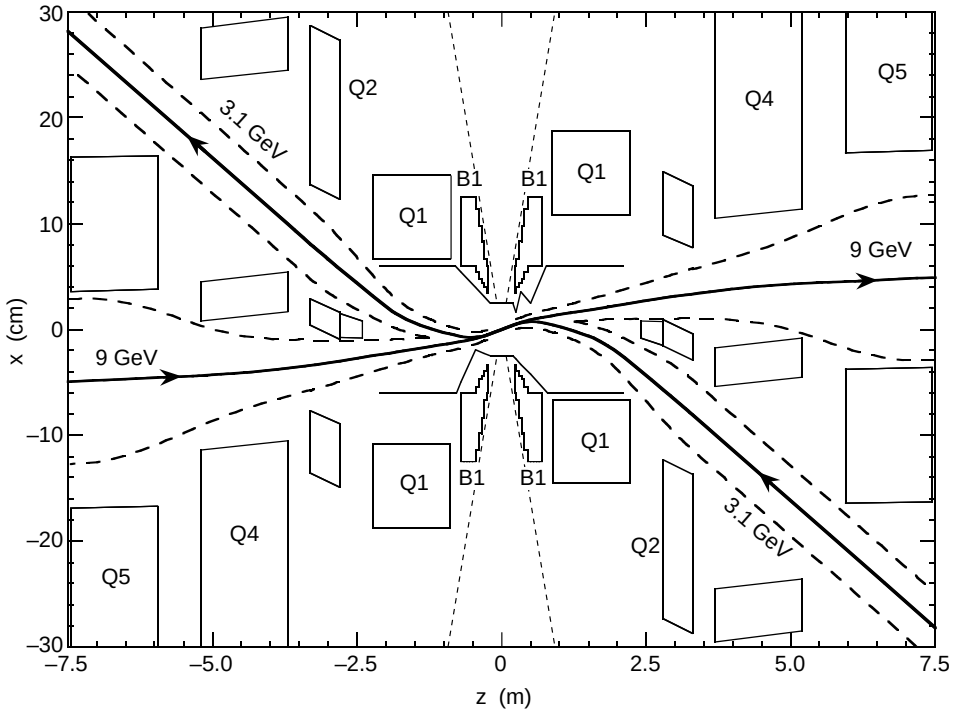

Figure 3.2: A plan view of the interaction region. The vertical scale is exaggerated. The beams collide head-on and are separated magnetically by the B1 dipole magnets. The focusing of the beams is achieved by using the quadrupole magnets,Q1,Q2,Q4 and Q5 The dashed lines indicate the beam stay-clear region and the detector acceptance cutoff at 300mrad.

required magnitude are beam-beam interference and related beam instabilities. After collision at the interaction point, IP, the beams are separated by the dipole magnet B1, located at ± 21 cm on either side of the IP, the two beams are separated within 62 cm of the IP, thus avoiding spurious collisions between out of phase bunches. To achieve this the B1 magnets had to be located entirely within the *BABAR* detector volume. The strong focusing of the beam is achieved by using an array of quadrupole magnets. The innermost focusing magnet (Q1) is common to both beams and partially enters the detector volume. The support tube of the Q1 magnets runs through

the center of the detector between the drift chamber and the silicon vertex tracker. Q2 is used to focus only the LER whereas Q4 and Q5 are used only for the HER. Both Q1 and B1 are permanent magnets while Q2, Q4 and Q5 are standard iron electro-magnets. The IP is surrounded by a water-cooled Beryllium pipe with an outer radius of 2.8 cm, presenting about 1.08 % of a radiation length to particles at normal incidence.

The impressive luminosity of $4.5 \times 10^{33}\,\mathrm{cm}^{-2}\mathrm{s}^{-1}$ was achieved by using high beam currents, a multi-bunch mode and strong focusing of the beams with magnets. Within three years of its operation PEP-II has not only achieved its design luminosity of $3.3 \times 10^{33}\,\mathrm{cm}^{-2}\mathrm{s}^{-1}$ but has also surpassed it by about 30%.

The high luminosity of PEP-II has important implications in terms of acceptable background levels for the proper functioning of the detector. Background sources include synchrotron radiation, interactions between the beam and the residual gas in the rings, and electro-magnetic showers produced in beam-beam collisions. Bremsstrahlung and Coulomb scattering of the beam particles off the residual gas in the rings dominate the Level 1 trigger rate, the instantaneous silicon vertex detector dose rates, and the total drift chamber current. Energy-degraded beam particles resulting from such interactions are bent by the separation dipole magnets horizontally into the beam pipe, resulting in occupancy peaks for almost all of the *BABAR* subdetectors in the horizontal plane. The rate of this background is proportional to the product

of the beam currents and the gas pressure in the rings. At higher luminosities the background from radiative Bhabha scattering is expected to be crucial.

3.3. Detector Overview

A layout of the *BABAR* detector is shown in (Fig. 3.3)

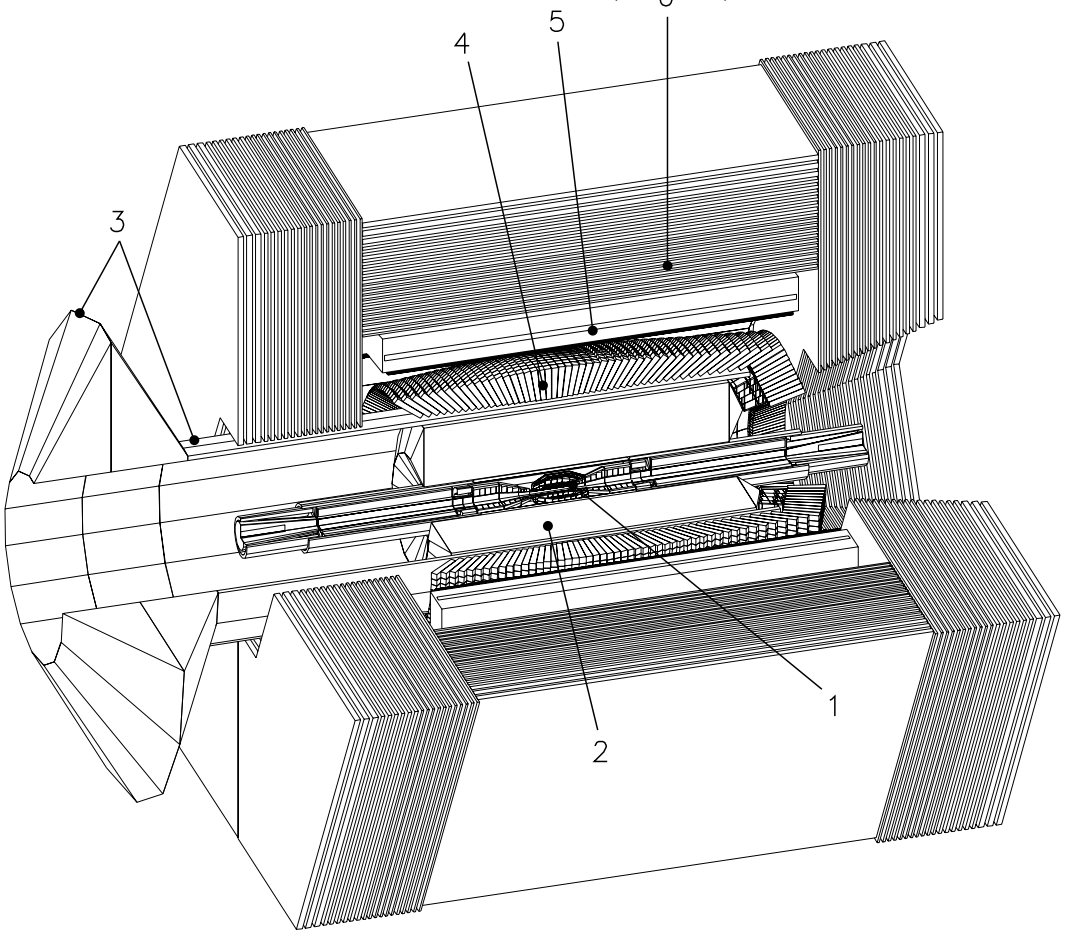

Figure 3.3: Layout of the *BABAR* detector, see text for key.

Trajectories of charged particles are measured in the Silicon Vertex Tracker (1) which is surrounded by a cylindrical wire chamber, the Drift Chamber (2). A novel

Cherenkov detector (3) used for charged particle identification surrounds the drift chamber. The electromagetic showers of electrons and photons are detected by the CsI crystals of the Electromagnetic Calorimeter (4) which is located just inside the solenoidal coil of the super-conducting magnet (5). Muons and hadrons are detected by arrays of resistive plate chambers that are inserted in the gaps of the iron flux return of the magnet (6). The detector acceptance is $17^\circ < \theta_{\rm lab} < 150^\circ$ in the laboratory frame (-0.95 $< \cos\theta_{\rm CM} <$ 0.87 in the center of mass frame) where θ is the polar angle.

3.4. The Silicon Vertex Tracker (SVT)

The device most critical to this thesis analysis is the SVT. The SVT was designed to provide precise reconstruction of charged particle trajectories and decay vertices near the interaction region. Good vertexing is crucial for $\mathcal{CP}$ violation studies, it is imperative to measure the mean spatial position of each B meson decay vertex along the z axis with better than 80 μm in resolution. As many of the decay products of the B have a low p_T, the SVT must also provide track reconstruction for particles with p_T, less than 120 MeV/c, as these tracks do not reach the drift chamber. As it is the detector closest to the beams, it must also withstand an integrated dose of 2 MRad of ionizing radiation. A radiation monitoring system capable of aborting the beam is needed to ensure that the device is not exposed to radiation that would

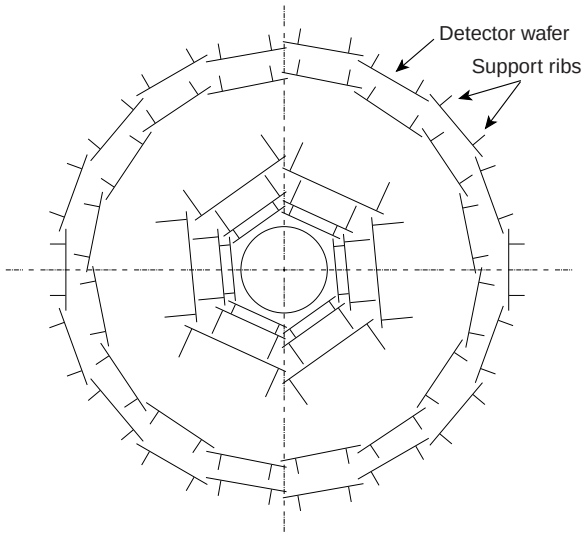

Figure 3.4: SVT layout in $x - y$ view. Only barrel wafers are shown.

exceed the design tolerance within the anticipated lifetime of the experiment. As the SVT is inaccessible during normal running, robustness and reliability are essential.

3.4.1. Silicon Vertex Tracker Overview

The SVT is a five layer double-sided silicon micro-strip detector. Fig. 3.4 shows the layout of the detector in the $x - y$ plane and Fig. 3.5 shows an $r - z$ view of the upper half. The acceptance of the device is $17.2^\circ < \theta < 150^\circ$ in the laboratory frame. To reduce the effect of multiple scattering on the determination of the track impact parameters, it is important to minimize the amount of material between the interaction-point and the first measuring plane and to place the first layer of the SVT

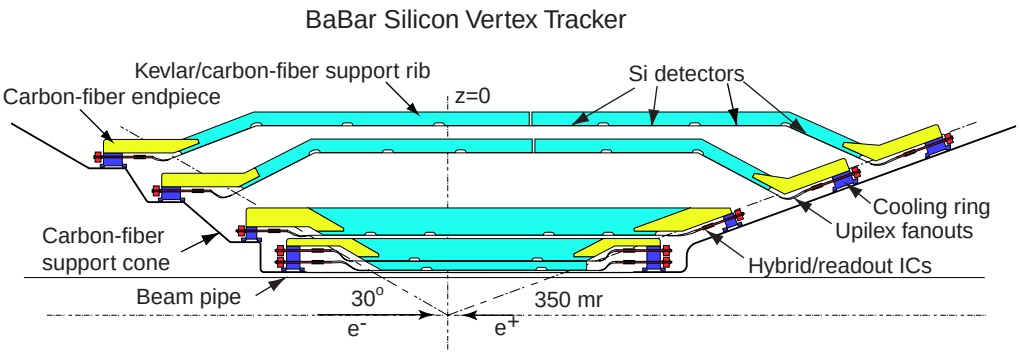

Figure 3.5: SVT layout: cross-section view of the upper half. The first layer radius is 3.3 cm, and the maximum fifth layer radius is 14.4 cm. The outer layers have an arch structure to minimize the amount of silicon needed for the solid angle coverage and to reduce large incidence angles.

as close as possible to the beam pipe.

The first three layers are arranged in a barrel structure, divided into sextants. Their primary goal is to provide precision angle (azimuthal angle ϕ and the polar angle θ) and impact parameter measurements. The outer layers are needed for pattern recognition and stand-alone tracking. Within each layer, silicon wafers are combined into modules. There are 6 modules in the first three layers. The modules have 4 wafers each in the first two layers and 6 wafers each in the third layer. Layers 4 and 5 have 16 and 18 modules with 7 and 8 wafers per module, respectively. The total number of wafers is 340. This design was chosen to minimize the amount of silica required to cover the solid angle, while not compromising on efficiency. Each module is divided into two halves, forward and backward. To measure the z coordinate there are strips on the inner sides of the detector that run perpendicular to the beam direction while the strips on the outer sides run orthogonal to the z strips in order to measure the ϕ coordinate.

As the SVT is the closest sub-detector to the interaction point, the radiation doses are constantly monitored with 12 silicon photo-diodes, located at a radius of 3 cm from the beam pipe. Even though the instantaneous dose can be very high during beam injection, the lifetime of a detector subsystem is determined not by the instantaneous rates, but by the total integrated radiation dose.

3.4.2. Performance

The SVT hit resolution can be calculated by comparing the number of associated hits to the number of tracks crossing the active area. The combined hardware and software efficiency as a function of the track incident angle, for each of the five layers is about 97%. The measured charged particle energy loss as it passes through the silicon, $\mathrm{d}E/\mathrm{d}x$ is used for particle identification and achieves a 2σ separation between kaons and pions up to a momentum of 500 MeV/c and between kaon and proton beyond 1 GeV/c.

The SVT has been operating efficiently since its installation in the *BABAR* experiment and has satisfied the original goal for vertex and low transverse momentum hit resolution.

3.5. Drift Chamber (DCH)

The most important sub-system of the experiment is the Drift Chamber, DCH. The central tracking device of *BABAR* is the DCH, which provides trajectory information for charged particle with momenta greater than approximately 100 MeV/c. It also complements the silicon vertex tracker in the measurements of the impact parameter and momentum of charged particle. The DCH is used for particle identification through the measurement of ionisation loss ($\mathrm{d}E/\mathrm{d}x$) and it is the central component of the charged particle trigger (L1).

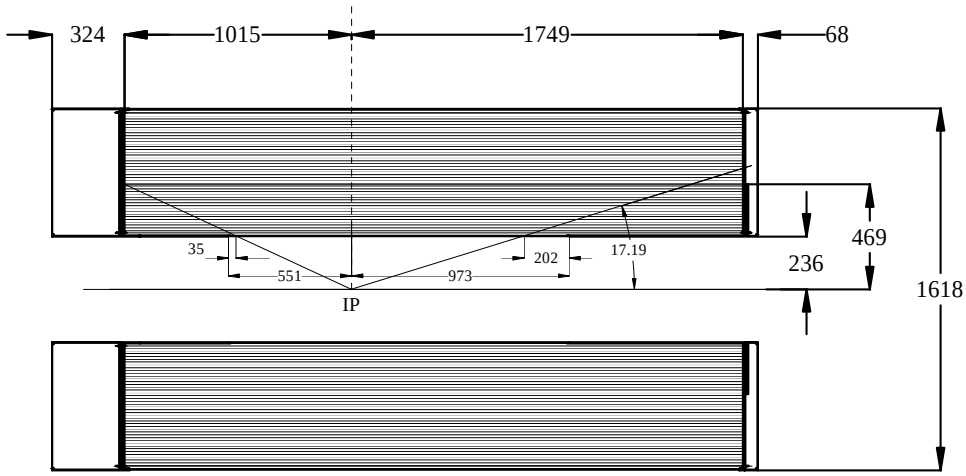

Figure 3.6: Longitudinal section of the DCH with principle dimensions in mm.

3.5.1. Drift Chamber Overview

A longitudinal section of the DCH is shown in Fig. 3.6. It primarily consist of a 280 cm long concentric cylinders with the end-plates made of aluminum, strung with low-mass aluminum wires and filled with a 80:20 mixture of helium:isobutane. A low density helium-based gas mixture is used to reduce multiple scattering. It achieves a dE/dx resolution of approximately 7.5%.

The inner radius is 23.6 cm. The outer radius is 80.9 cm. The forward-backward coverage is $-1.11 < z < 1.66$ m due to the $\Upsilon(4S)$ boost along the z axis. In order to facilitate track matching between the silicon vertex tracker and the DCH and reduce photon conversion, the DCH cylinder walls were made as thin as possible. The inner cylinder is 1 mm of beryllium or 0.28 % radiation length and the outer cylinder consist of 2 layers made of carbon fiber on a nomex core of 1.5 % of radiation length. The

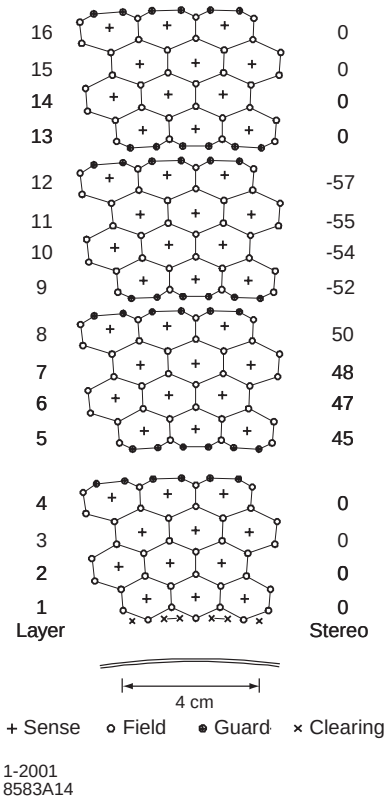

Figure 3.7: Schematic layout of the drift chamber layer arrangement. The layers are arranged into 10 super-layers of 4 layers each.

total thickness of the DCH is approximately 1.08 % of radiation length at normal incidence.

The wires are organized into 40 layers of small hexagonal cells, subdivided into 10 super-layers in an alternating axial (A) and stereo (U,V) pattern, as shown in Fig. 3.7. The stereo angle increases radially from ± 45 mrad to ± 76 mrad. The stereo measurements are used for extracting the longitudinal (z) position information. There are a total of 7,104 small drift cells typically 1.2 x 1.9 cm^2 in size. Each cell contains a 20 μm gold-plated tungsten-rhenium sense wire, surrounded by a grid of

gold-plated aluminum field wires which are 120 μm and 80 μm thick. Near the sense wire, isochrones are circular; however, they become distorted close to the field wires. A potential of 1900-1960 V is applied to the sense wires, while the field wires are grounded. This potential difference gives an avalanche gain of about 5×10^4. The cells are designed to provide an average intrinsic spatial resolution better than 40 μm.

The DCH meets the design expectations. It contributes primarily to the measurement of the momentum transverse to the beam, p_T, while the angle and position measurement near the interaction point is dominated by the silicon vertex tracker. The data is well represented by the following formula:

$$\frac{\sigma_{p_t}}{p_t} = (0.13 \pm 0.01)\%\ p_t + (0.45 \pm 0.03)\% \tag{3.1}$$

3.5.2. Tracking Performance

Charged tracks are defined by five parameters (d_0, ϕ_0, ω, z_0, and $\tan\lambda$). These parameters are measured at the point of closest approach to the axis, d_0 and z_0 are the distance of this point from the origin of the coordinate system in the x-y plane and along the z axis, λ is the dip angle relative to the transverse plane, $\omega = \frac{1}{p_t}$ is its curvature, ϕ_0 is the azimuth of the track. Track reconstruction in *BABAR* can be performed independently by the silicon vertex tracker and the DCH, thus making it

possible to determine the absolute tracking efficiency of the DCH to the number of tracks detected by the silicon vertex tracker, provided that corrections for fake tracks found in the silicon vertex tracker and scattering of the tracks from the support tube are applied. A small additional correction needs to be applied to account for the fact that the two tracking subsystems are linked together at one stage by a common track finding algorithm. This method of estimating tracking efficiencies is applied to both the Monte Carlo and Data sample, Fig. 3.8 shows the tracking efficiency as a function of transverse momentum and polar angle for a sample of multi-hadron events. During the years 1999-2000 the data was taken with two different voltage settings of 1900 V and 1960V. The tracking efficiency at 1960 V was measured to be $(98 \pm 1)\%$ for tracks with $p_T > 200$ MeV/c and polar angle $\theta > 500$ mrad, at 1900 V, the efficiency is slightly lower, by about 5%, for tracks at normal incidence. The resolutions of the five track parameters are monitored using Bhabhas and dimuon events. The resolutions in the coordinates, d_0 and z_0 are dependent on the transverse momentum, which are obtained using multi-hadron events and are about 25 μm and 40 μm respectively at p_T of 3 GeV/c.

The estimated error in the measurement of the difference along the z axis between the decay vertices of the two neutral B meson where one B^0 is fully reconstructed while the other is partially reconstructed is shown in Fig. 3.9. The rms width of 190 μm is dominated by the reconstruction of the partially reconstructed B^0 (170 μm)

while the rms for the resolution for the fully reconstructed B^0 is 70 μm.

3.6. Detection of Internally Reflected Cherenkov Light (DIRC)

The device that plays a significant role in the flagship $\mathcal{CP}$ analysis is the DIRC. Good particle identification is crucial for measurements that depend on the need to identify the favor of the B^0 meson or to identify kaon and pion with high purity and efficiency. Kaon pion separation up to momenta of 0.7 GeV/c is obtained by measuring the ionisation energy loss, dE/dx, in the silicon vertex detector and the drift chamber. The DIRC provides the particle identification for higher momentum tracks that are important to many analyses..

3.6.1. DIRC Overview

A schematic of the DIRC geometry to illustrate the principles of light production, transportation, and imaging is shown in Figure 3.10. The DIRC uses thin, long rectangular bars made of synthetic fused silica (quartz) [29] (H $\times$ W $\times$ L = 17 mm $\times$ 35 mm $\times$ 4900 mm) both as Cherenkov radiators and light guides (refractive index $n \approx 1.47$). The 144 bars are arranged in a 12-sided polygonal barrel with a radius of about 84 cm around the beam axis. The DIRC bars extend 178 cm forward from the interaction point of *BABAR* covering 87% of the polar solid angle in the center-of-mass frame. Each set of 12 bars are housed in a bar box surrounded

by nitrogen at NTP (refractive index $n \approx 1$). The Cherenkov angle is given by the familiar relation

$$\cos\theta_c = 1/n\beta. \tag{3.2}$$

where $\beta = \frac{v}{c}$, v = speed of the particle, c = speed of light. Since the refractive index of the radiator bar is larger than $\sqrt{2}$, a certain fraction of the Cherenkov photons produced by a relativistic charged particle traversing the quartz bar will undergo total internal reflection, regardless of the incidence angle of the tracks, and propagate along the length of the bar. Only one end is instrumented, so a mirror (reflectivity $\approx 92\%$) is placed perpendicular to the bar axis on the other end. Photons exiting the bar in downward direction, or with large angles in radial direction, are partly recovered into the instrumented area by a prism at the readout end. The prism reduces the required photon-sensitive area by more than a factor of two, with little complexity to the image reconstruction.

A thin (9 mm) quartz window separates the prism from the so called standoff box (SOB), a water tank filled with 6000 liters of purified water (index $n \approx 1.33$) built in a toroidal shape. The backplane of the SOB is divided into 12 sectors, each equipped with 896 conventional photo-tubes of approximately 25% detection efficiency at 400 nm wavelength (spectral range: 250 nm – 650 nm) pointing to the exit of a corresponding bar box.

3.6.2. Performance

The overall single photon resolution is about 9.6 mrad, dominated by the track reconstruction and the chromatic aberrations. The resolution on a track scales as $\sigma_\gamma/\sqrt{N_\gamma}$, where σ_γ is the resolution of a single photon and N_γ is the number of detected photons. N_γ is about 30 for normal incidence tracks. The average track Cherenkov angle resolution, measured in dimuon events, turns out to be 2.5 mrad, which leads to a approximately 4 σ separation between kaons and pions at 3.3 GeV/c momenta.

3.7. Electromagnetic Calorimeter (EMC)

The electromagnetic calorimeter (EMC) of *BABAR* is designed to measure the energy in the electromagnetic showers with excellent efficiency, energy and angular resolution over the energy range of 20 MeV to 9 GeV. This capability allows for reconstruction of π^0 and η mesons and for the separation of photons, electrons and positrons from charged hadrons. The active elements are thallium-doped cesium iodide (CsI(Tl)) crystals.

3.7.1. Electromagnetic Calorimeter Overview

The EMC as shown in Fig. 3.11 and consists of a cylindrical barrel and a conical forward end-cap. The range of coverage in the center of mass solid angle is $-0.916 \leq$

$\cos\theta \leq 0.895$, the backward-forward asymmetry reflecting the boost of the collision in the laboratory frame. The barrel section covers the center of mass solid angle of $-0.916 \leq \cos\theta \leq 0.715$ and has an inner radius of 91 cm. It contains 5760 barrel crystals, arranged in 48 θ rows, each row having 120 identical crystals around ϕ. Each crystal is held in a 250 μm thick carbon fiber composite compartment, that are grouped into 2804 modules of 3 crystals wide and 7 crystals long. The forward end-cap is a conic section and covers a center of mass solid angle of $0.718 \leq \cos\theta \leq 0.895$. It contains 820 end-cap crystals grouped into 20 modules of 41 crystals each.

The crystals have a trapezoidal shape with typical dimensions of $47 \times 47\,\mathrm{mm}^2$ at the front face and $60 \times 60\,\mathrm{mm}^2$ and ranges from 17.5 to 16 radiation length thickness in the forward and the end-cap part. The emission of the scintillation light produced in the crystals permits the use of silicon photo-diodes which are attached to the back faces of the crystals. The signal is amplified and sent to the data acquisition board and to the Level 1 trigger system. The average light yield per crystal is 7300 photo-electrons/ MeV varying between 5000 and 10000 over an electronic noise of the order of 900 photo-electrons.

3.7.2. Performance

The calorimeter has an efficiency of more that 96% for detecting photons, above a minimum measurable energy of about 20 MeV. The limit is largely determined

by beam and event related backgrounds and the amount of material in front of the calorimeter. At low energy, the energy resolution of the EMC is measured periodically with a radioactive source. At high energy the energy resolution is measured from Bhabha scattering events and is parameterized by :

$$\frac{\sigma_E}{E} = \frac{(2.32 \pm 0.30)\%}{E(\text{ GeV})^{\frac{1}{4}}} \oplus (1.85 \pm 0.12)\% \tag{3.3}$$

where E is the photon energy in GeV. At lower energies the resolution is dominated by fluctuations in photon statistics and by beam generated backgrounds and at higher energies(> 1 GeV) by the non-uniformity in light collection from leakage or absorption in the material between or in front of the crystals. The reconstructed π^0 mass has a width of 6.9 MeV/c^2 and is shown in Fig. 3.12. The mass resolution is dominated by the energy resolution at lower energies (below 2 GeV). At higher energies, the mass resolution is dominated by the angular resolution. The latter is determined primarily by the transverse crystal size. The angular resolution can be found from analyses of π^0 and η decays. The angular resolution can be parameterized by

$$\sigma_\theta = \frac{3.87 \pm 0.07}{\sqrt{E(\text{ GeV})}} \oplus (0.00 \pm 0.04) \text{ mrad} \tag{3.4}$$

3.8. Instrumented Flux Return (IFR)

The Instrumented Flux Return was designed to identify muons with high efficiency and good purity and to detect neutral hadrons over a wide range of angles and momenta.

Data from this sub-system was not central to the analysis described in this thesis but a brief description is included for completeness

3.8.1. Instrumented Flux Return Overview

The IFR, shown in Fig. 3.13, consists of three parts: the barrel and the forward and backward endcaps. All of them are subdivided into sextants. The active detectors are 806 Resistive Plate Chambers (RPC) [30], located in the gaps between the layers of steel. There are 19 RPC layers in the barrel, and 18 layers in the endcaps. Additionally, there are two layers of cylindrical RPCs between the EMC and the magnet. The thickness of the steel layers ranges from 2 cm in the inner 9 layers to 10 cm in the outermost layers. RPCs are gas chambers enclosed between bakelite (which is a phenolic polymer) plates. In both the planar and cylindrical RPCs, the gap between the bakelite sheets is 2 mm, and the sheets themselves are 2 mm thick. One of the plates is kept at approximately 8 kV, and the other is grounded, so that an ionizing particle crossing the gas gap will produce a quenched discharge. The gas used is a mixture of 56.7% Argon, 38.8% Freon-134a, and 4.5% isobutane.

3.8.2. Performance

The efficiencies of the RPCs are routinely evaluated for both colliding beam events and cosmics. 75% of the RPCs are over 90% efficient. The average RPC efficiencies during the 1999-2000 data taking run were $\sim$ 78% in the barrel and $\sim$ 87% in the forward endcap region.

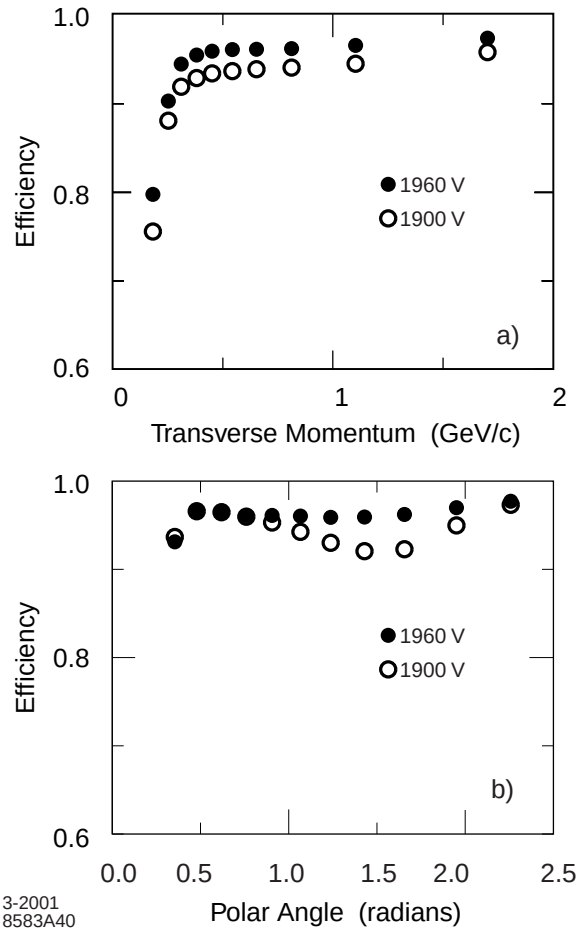

Figure 3.8: The track reconstruction efficiency in the DCH at operating voltage of 1900 V and 1960 V as a function of a) transverse momentum and b) polar angle. The measurement at the DCH voltage of 1900 V(open circle) and 1960 V (solid circle) are shown.

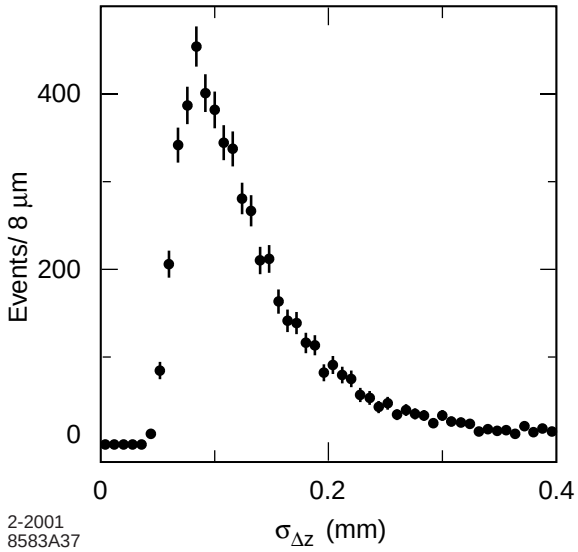

Figure 3.9: Estimated error in the difference Δz between the B^0 meson decay vertices for a sample of events in which one B^0 is fully reconstructed.

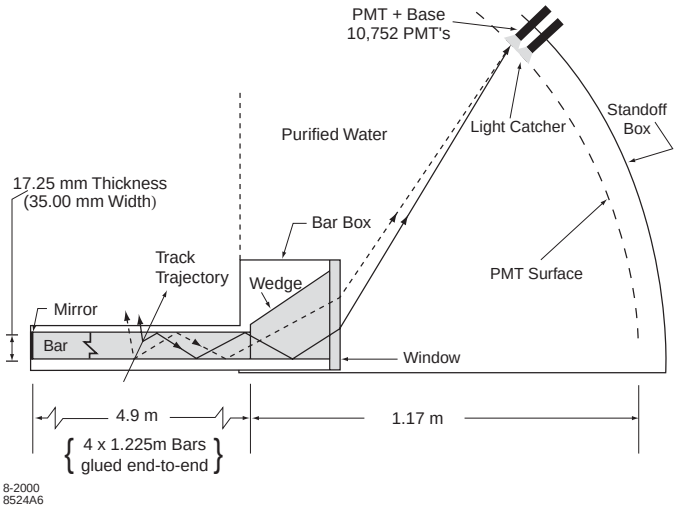

Figure 3.10: Schematic of the DIRC fused silica radiator bar and imaging region.

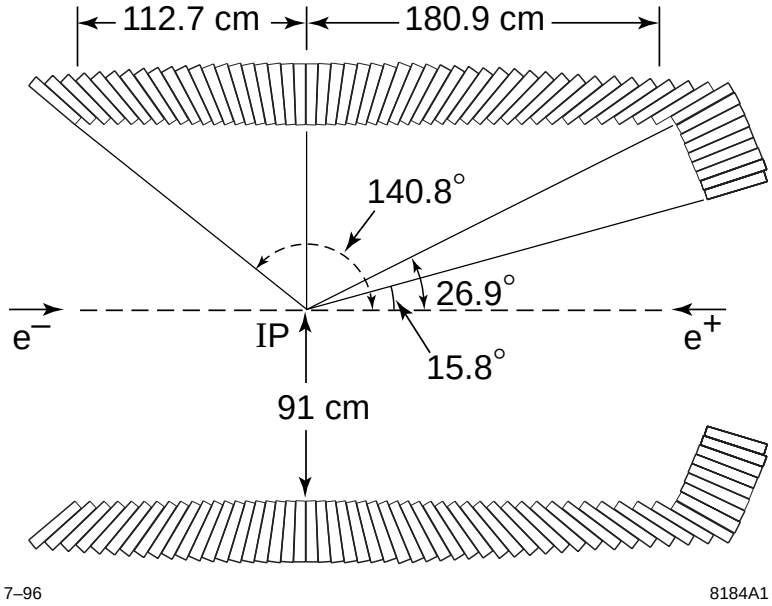

Figure 3.11: Layout of the EMC showing the barrel and the forward end-cap region.

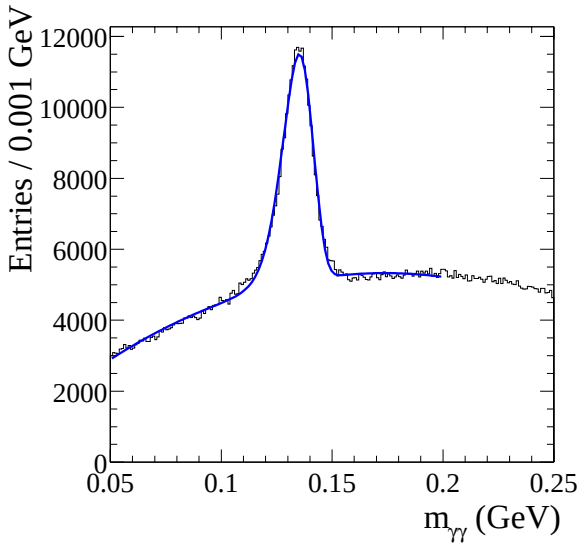

Figure 3.12: Invariant mass of two photons in a $B\overline{B}$ events. The energies of the photons and the π^0 are required to be between 30 MeV and 300 MeV. The solid line is the fit to data.

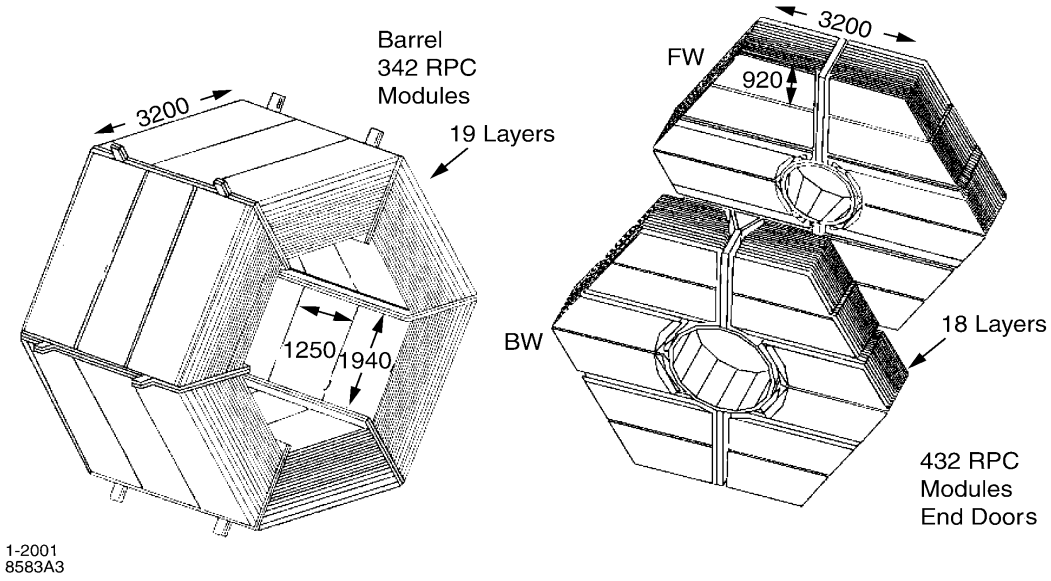

Figure 3.13: The Instrumented Flux Return consists of three sections: the barrel (left), containing 342 RPC modules between 19 layers of steel, and the forward and backward end-doors (right), with a total of 432 RPC modules in 18 layers. 32 more RPCs are placed in the two cylindrical layers (not shown here).

Chapter 4

Analysis Method

4.1. Introduction

The $\mathcal{CP}$ asymmetry in $B^0 \to D^{*-}h^+$ [1], where h can be a π, ρ, or an a_1 is expected to be small since the two interfering decays have very different amplitudes (Sec. 2.7). The technique of partial reconstruction has the potential to achieve an interesting sensitivity to the small $\mathcal{CP}$ asymmetry in these decays. In this chapter we describe the technique of "partial reconstruction" which has been used successfully by the CLEO collaboration to measure the $B^0 \to D^{*-}\pi^+$ branching ratio [31] and time-independent mixing analysis using $B^0 \to D^{*-}\rho^+$ and $B^0 \to D^{*-}\pi^+$ events [32]. This technique increases the acceptance for the sequence $\Upsilon(4S) \to B^0\overline{B}^0$, $B^0 \to D^{*-}h^+$, $D^{*-} \to \overline{D}^0\pi^-$, by one order of magnitude compared to the usual technique of "full reconstruction", where all the particles in the final state are reconstructed. Using the

[1] charge conjugate decays are implied throughout the text

latter technique the CLEO collaboration reconstructed 248 data events while using the partial reconstruction they selected 2600 data events out of approximately 8700 possible $B^0 \to D^{*-}\pi^+$ candidate events. Thus the technique of partial reconstruction should provide a significant increase in the number of available events, albeit with a decrease in the purity of the selected event sample compared to full reconstruction.

4.2. Method of Partial Reconstruction

A schematic of the principle of partial reconstruction is shown in Fig. 4.1. Consider the decay chain $B^0 \to D^{*-}\rho^+$, followed by $D^{*-} \to \overline{D}^0\pi_s^-$ (the π_s has an average momentum of 200 MeV/c hence the sub-script s to indicate slow). The difference between the $\Upsilon(4S)$ mass and twice the B^0 mass is very small, hence the B^0 mesons are produced nearly at rest in the $\Upsilon(4S)$ rest frame, which is the Center of Mass (CM) frame. As the energy released in the D^* decay is small, the π_s from the decay will maintain approximately the same direction as that of the D^*. The $B^0 \to D^{*-}\rho^+$ decay can be fully described by 20 parameters, namely the four-momenta of the B^0, ρ, D^*, $\overline{D}^0$ and π_s. In partial reconstruction only the ρ and the π_s are "observed"; their four-momentum are measured, while the four-momentum of the "missing" $\overline{D}^0$, labeled as D_{miss}, is not measured. As there are twelve unmeasured parameters, twelve constraints are used to describe the decay namely: the energy-momentum conservation in the B^0 and the D^* decay (eight constraints); the masses

of the B^0, the D^* and the D_{miss} (three constraints); and the energy of the B^0 in the CM frame which is equal to half the machine CM energy (one constraint). The

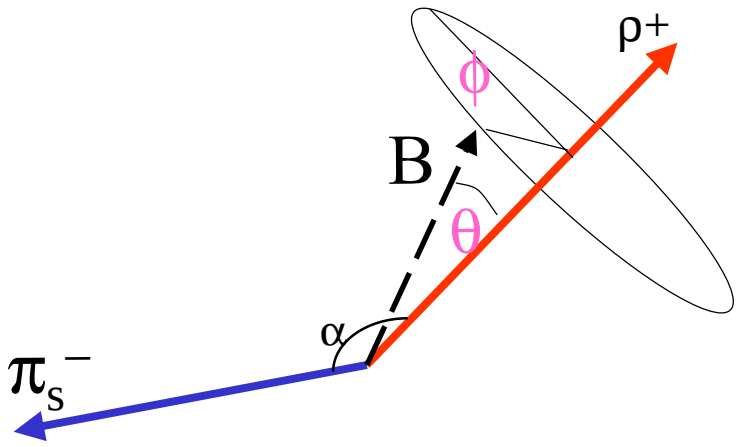

Figure 4.1: A schematic drawing to represent the decay $B^0 \to D^{*-}\rho^+$. ρ is the daughter of the B^0 and the π_s is the daughter of the D^*. The momentum of the B^0 is known up-to an angle θ with respect to the ρ momentum.

constraints are applied as follow:

We designate $\vec{p}_q$, M_q, E_q, as the momentum, mass and energy of the particle q, where q is either: π_s, ρ, D^*, $\overline{D}^0$, B^0 respectively, in the CM frame.

From four-momentum conservation in the decay of the B^0 we obtain:

$$\vec{p}_B = \vec{p}_\rho + \vec{p}_{D^*}. \tag{4.1}$$

$$E_B = E_\rho + E_{D^*}. \tag{4.2}$$

Using the above equations one can calculate the angle between the momenta of the

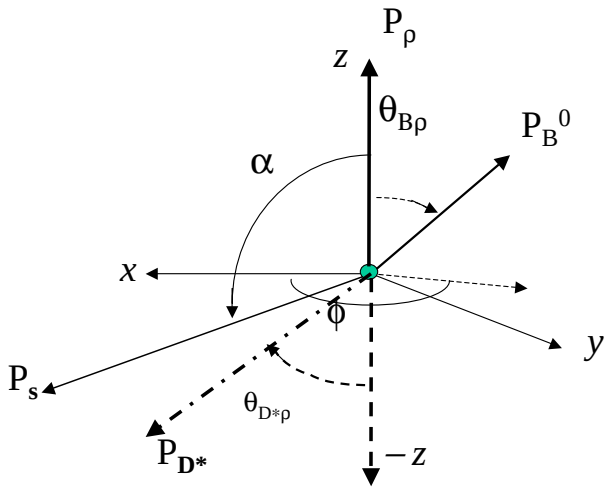

Figure 4.2: Definition of the coordinate system $\vec{x}$, $\vec{y}$, $\vec{z}$, with $\vec{z}$ parallel to the direction of $\vec{p}_\rho$ and $\vec{p}_B$ lies in a cone of half angle $\cos\theta_{B\rho}$ about ρ and the angle ϕ is unknown. $\vec{x}$ lies in the plane defined by $\vec{p}_\rho$ and $\vec{p}_\pi$

B^0 and the ρ to be:

$$\cos\theta_{B\rho} = \frac{M_{D^*}^2 - M_B^2 - M_\rho^2 + 2E_B E_\rho}{2|\vec{p}_B||\vec{p}_\rho|}. \tag{4.3}$$

Knowing the CM energy, $\sqrt{s}$, the energy and mass of the B^0, E_B and $|\vec{p}_B|$ is obtained from :

$$E_B = \frac{\sqrt{s}}{2}. \tag{4.4}$$

$$|\vec{p}_B|^2 = E_B^2 - M_B^2. \tag{4.5}$$

The four-momentum of the missing $\overline{D}^0$, $P_{D_{\rm miss}}$, can be obtained from the four-momentum conservation in the decay of the $\overline{D}^0$ and the D^*:

$$P^2_{D_{\rm miss}} = M^2_B + (P_\rho + P_\pi)^2 - 2(E_B(E_\rho + E_\pi) + \vec{p}_B \cdot (\vec{p}_\rho + \vec{p}_\pi)). \tag{4.6}$$

where P_ρ and P_π are the four-momentum of the ρ and π_s respectively. Introducing a system of coordinates: $\vec{x}$, $\vec{y}$, $\vec{z}$, with $\vec{z}$ parallel to $\vec{p}_\rho$ and $\vec{x}$ lies in the plane defined by $\vec{p}_\rho$ and $\vec{p}_\pi$ (see Fig. 4.2), the B^0 momentum can be expressed as $\vec{p}_B = |\vec{p}_B|(\cos\theta_{B\rho}\vec{z} + \sin\theta_{B\rho}\cos\phi\vec{x} + \sin\theta_{B\rho}\sin\phi\vec{y})$. The only term in Eq. 4.6 that depends on the direction of the B^0 momentum is the last term, which can be re-written as

$$\vec{p}_B \cdot (\vec{p}_\rho + \vec{p}_\pi) = |\vec{p}_B||\vec{p}_\rho|\cos\theta_{B\rho} + |\vec{p}_B||\vec{p}_\pi|\cos\theta_{B\rho}\cos\alpha + |\vec{p}_B||\vec{p}_\pi|\sin\theta_{B\rho}\sin\alpha\cos\phi. \tag{4.7}$$

where α is the angle between the $\vec{p}_\rho$ and $\vec{p}_\pi$. The angle ϕ is unknown. Thus for a given value of ϕ, the ϕ-dependent missing mass is calculated as :

$$m(\phi) = \sqrt{P_{D_{\rm miss}}(\phi) \cdot P_{D_{\rm miss}}(\phi)}. \tag{4.8}$$

We define a parameter to represent the missing $\overline{D}^0$ mass referred to as the missing mass, $m_{\rm miss}$:

$$m_{\rm miss} \equiv \frac{m(\phi_{\rm max}) + m(\phi_{\rm min})}{2}. \tag{4.9}$$

Where $\phi_{\rm max}$ ($\phi_{\rm min}$) is the value of ϕ for which $m(\phi)$ obtains a maximal (minimal) possible value. As seen from signal Monte Carlo events $m_{\rm miss}$ distribution peaks

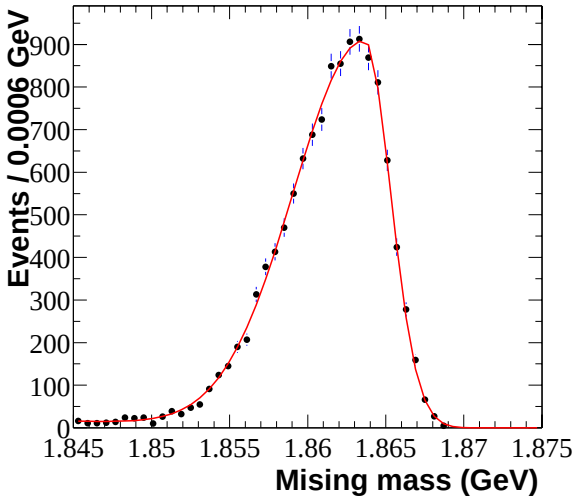

Figure 4.3: $m_{\rm miss}$ distribution for signal, $D^*\rho$, Monte Carlo events.

around the nominal mass of the $\overline{D}^0$, 1.864 GeV/c^2, shown in Fig. 4.3. The error introduced by the use of this parameter is not large since both $|\vec{p}_B|$ and $\vec{p}_\pi$ are small with respect to other terms in Eq. 4.6. The smearing in the $m_{\rm miss}$ is due to the averaging over ϕ and is much larger than the errors due to reconstruction of the π and ρ tracks. The spread in $m_{\rm miss}$ is about 3.5 MeV/c^2 for signal events. Background events have a different $m_{\rm miss}$ distribution as shown in Fig. 4.4. Thus $m_{\rm miss}$ is used as a variable to separate signal from background events.

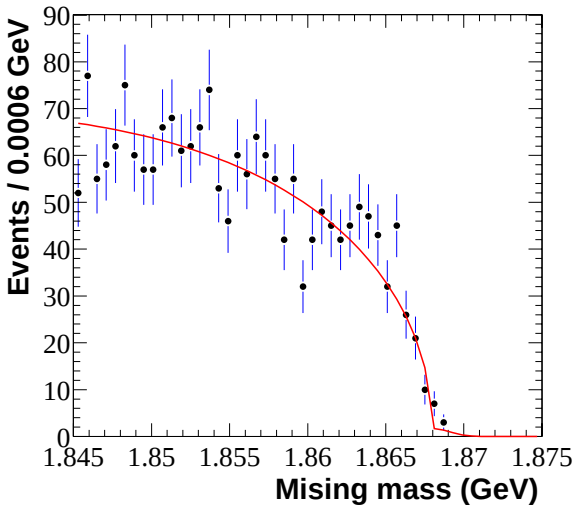

Figure 4.4: $m_{\rm miss}$ distribution for (combinatoric $B\bar{B}$) background Monte Carlo events.

4.3. Event Selection

The two steps used for event selection in data and Monte Carlo are described in this section. In the first step, a very rough selection of events is made to reduce the large size of the data sample. This process is done automatically as part of the standard reconstruction procedure (skim). For example in 20.6 fb^{-1} of data there are roughly 270 million events [33]. Of these roughly 120,000 events satisfy the pre-selection criteria. To these selected events a signal selection algorithm is applied and tighter selection criteria are applied to get a sample of $B^0 \to D^{*-}\rho^+$ events.

4.3.1. Pre-Selection Criteria

A very loose selection is done by looking at quantities relating to the whole event and to specific tracks in the event. To discriminate the more spherical $B\bar{B}$ events from the more jet-like continuum events as shown in Fig. 4.5 we use an event topology variable called the Fox-Wolfram moment, [34], defined as :

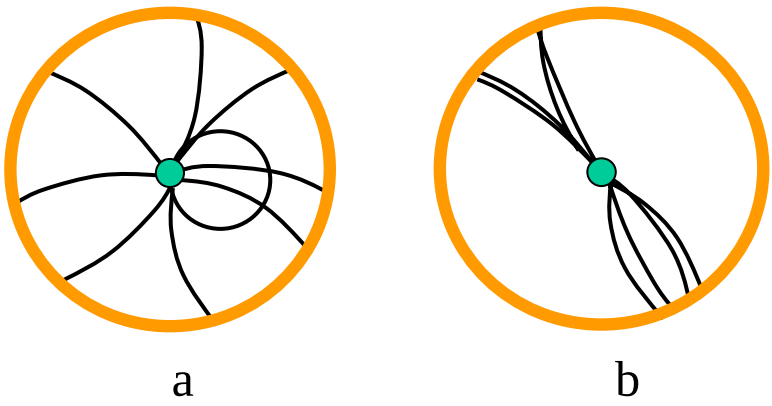

Figure 4.5: A schematic to show charge particle trajectories for (a) typical $B\bar{B}$ and (b) continuum event.

$$H_l = \sum_{i,j} \frac{|\vec{p}_i||\vec{p}_j|}{s} P_l(\cos(\phi_{ij})). \tag{4.10}$$

where $\vec{p}_i$, $\vec{p}_j$ is the momenta of the i^{th} and the j^{th} particle in the event and ϕ_{ij} the angle between them. $P_l(\cos(\phi_{ij}))$ are the Legendre polynomials and $\sqrt{s}$ is the center-of-mass energy. Only charged tracks are used in this definition.

An event is required to have a value of the ratio of the Fox-Wolfram moment,

$$R2 = \frac{H_2}{H_0}, \tag{4.11}$$

to be less than 0.35. H_2 and H_0 are the Fox-Wolfram moment of order two and moment of order zero respectively.

An event is also required to have at-least one π_s and one ρ candidate, where the ρ decays into a π^0 and π_f (where the average momentum of the π_f is 1.0 GeV/c, hence the subscript f to indicate fast). The ρ candidate is selected from a standard list (RhoCdefaultList) that consists of ρ candidates that are obtained by applying selection criteria on the difference between the reconstructed (m_ρ) and the nominal ρ mass $M_\rho = 770 \pm 0.8$ MeV/c^2 and the cosine of the helicity angle, $\cos\theta_\rho$. It is required that the daughter π^0 of the ρ is selected from a standard list (Pi0AllLooseList) that consists of the π^0 candidates that are obtained by applying selection criteria to its daughter photons ($\pi^0 \rightarrow \gamma + \gamma$), the minimum merged energy of the photons, the photon polar angle, θ_γ and the minimum energy of both the photons, $E_{min-\gamma}$. The selection criteria are summarized in Table 4.1. In addition to these requirements the ρ candidate must also satisfy the following criteria:

- $1.95\,\mathrm{GeV/c} \leq |\vec{p_\rho}| \leq 2.45$ GeV/c.
- $|(m_{\pi^0} - M_{\pi^0})| < 0.025$ GeV/c^2.
- $|\vec{p}_{\pi^0}| \geq 0.200$ GeV/c.

where m_{π^0} is the reconstructed π^0 and $M_{\pi^0} = 134 \pm 0.001$ MeV/c^2 is the nominal mass of the daughter π^0 and $|\vec{p}_G|$ is the magnitude of the CM momentum of the particle G which can be either a ρ or a π^0. The π_s candidate is selected from another standard list (GoodTracksVeryLooseList). This list consists of tracks that are obtained by applying selection criteria to (1) the transverse momentum of the track, p_T; (2) the number of hits of the track in the drift chamber; (3) the absolute value of the closest distance between the track and the beam spot in the $x - y$ plane, $|x_0|$; (4) and the absolute value of the closest distance between the track and the beam spot in the z direction, $|z_0|$. The cuts are summarized in Table 4.2. The momentum of the π_s in the CM frame is required to be between 0.05 GeV/c and 0.8 GeV/c. A charged track that satisfies the π_s requirement is then checked to make sure that it is not also consistent with being a π_f that comes from the decay of the ρ. If it fails to meet this requirement, the track is rejected. The two charged tracks, π_f and π_s, are then checked to make sure that they are not consistent with tracks that satisfy either the e, μ or K hypothesis. This is done by checking for a match between this track and a track that belongs to the XMicroTight list, where X is e, μ, or K. The requirements for a track to belong to the XMicroTightlist are described in Sec.4.3.5.

Table 4.1: The selection criteria used for a track to belong to the standard ρ list (RhoCDefaultList).

Variable	cut
$\lvert m_\rho - M_\rho \rvert$	< 0.380 GeV/c^2
$\lvert \cos\theta_\rho \rvert$	< 1
$\frac{m(\rho)-M_\rho}{\sigma_{m(\rho)}}$	< 0.001
π^0	Pi0AllLooseList

Variable	cuts (Pi0AllLooseList)
Minimum merged energy	1
Polar angle of the photons	$0.6 < E_{gamma} < \pi - 0.6$ rad
Minimum energy of the photons	$E_{min-\gamma} > 3$ MeV

Table 4.2: The selection criteria for a track to belong to the standard track list (GoodTracksVeryLoose) .

Variable	GoodTracksVeryLoose
no. of DCH hits	> 0
$\lvert x_0 \rvert$	< 1.5 cm
$\lvert z_0 \rvert$	< 10.0 cm

4.3.2. Final Selection Criteria

Events that satisfy the pre-selection criteria are subject to tighter conditions. Of the 120,000 events that satisfy the pre-selection criteria only 59,000 events satisfy the final selection criteria.

The requirements on the daughter π^0 of the ρ are tightened:

- $|m_{\pi^0} - M_{\pi^0}| \leq 20$ MeV/c^2.
- $|\vec{p_{\pi^0}}| \geq 0.400$ GeV/c in the CM frame.

To obtain a cleaner reconstructed signal events we require the candidates obtained from applying partial reconstruction technique to the ρ and the π_s satisfy the following criteria:

- $|\cos\theta_{B\rho}| \leq 1$, where $\theta_{B\rho}$ is the CM angle between the ρ and the B^0, calculated using Eq. (4.3).
- The absolute value of the closest distance between the track and the beam spot in the $x-y$ plane ≤ 1.5 cm.
- The absolute value of the closest distance between the track and the beam spot in the z direction ≤ 6 cm.
- $m_{\rm miss} \geq 1.845$ GeV/c^2.
- If multiple candidates are found in an event, we select the candidate with the smallest value of $m_{\rm miss} - M_{D^0}$, where M_{D^0} is the nominal mass of the D^0 .

We define the D^* helicity angle, θ_{D^*}, Eq. 4.12 to be angle between the directions of the $\overline{D}^0$ and the B^0 in the D^* rest frame.

$$\cos\theta_{D^*} = \frac{-\beta_{D^*}(E^*_{\pi_s} - E^*_{D^0})}{2P^*_{\pi_s}} + \frac{|\vec{p}_{\pi_s}|^2 - |P_{D^0}|^2}{2\gamma^2_{D^*}\beta_{D^*}M_{D^*}P^*_{\pi_s}}. \tag{4.12}$$

where E_q^* and P_q^* is the energy and momentum of q in the D^* rest frame and γ_r and β_r is the Lorentz boost factor and velocity of r in the CM frame, obtained from the kinematics of the decay. Similarly we define the ρ helicity [2] angle, θ_ρ to be angle between the directions of the π^0 and the CM frame in the ρ rest frame. Since the longitudinal polarization in the $B^0 \to D^{*-}\rho^+$ decay [35] is $(87.8 \pm 4.5)\%$, the $\cos\theta_\rho$ and $\cos\theta_{D^*}$ distributions of signal events peak close to ± 1 (Fig. 4.6). By applying the D^0 mass constraint the $\cos\theta_{D^*}$ is computed. It is possible for background events to have $|\cos\theta_{D^*}|$ greater than one. Signal events can also have $|\cos\theta_{D^*}|$ greater than one due to detector resolution. Due to the characteristic shape of the signal and background in the helicity angle distribution, as shown in Fig. 4.6, it is a useful variable to separate signal from background events. We apply the following criteria to reject background events.

- $|\cos\theta_\rho| > 0.3$, where θ_ρ is the angle between the momenta of the π^0 and the $\Upsilon(4S)$ in the ρ rest frame.

- $|\cos\theta_{D^*}| > 0.3$, where θ_{D^*} is the angle between the momenta of the $\overline{D}^0$ and the B^0 in the D^* rest frame, calculated as in Eq. (4.12.)

- Events are rejected if they satisfy $\cos\theta_\rho > 0.3$ and $\cos\theta_{D^*} < -0.3$. The corner of the $(\cos\theta_{D^*}, \cos\theta_\rho)$ plane that contain a lot of $B\overline{B}$ background (Fig 4.6) are cut off.

[2] here we use a different convention for helicity

The total efficiency for all the criteria that are used to select signal events is $(4.35 \pm 0.09)\%$ where the error is purely due to Monte Carlo statistics.

4.3.3. Fisher Discriminant

We do not cut on the Fisher discriminant in this analysis but use it in the fit as described in Sec. 7.1.

To further suppress continuum background, seven event shape variables are combined into a Fisher discriminant, $\mathcal{F}$ [36]. To select particles that are produced by the decay of the other B^0 meson in the event these variables are calculated using two sets of tracks and calorimeter cluster: Set 1: All tracks and calorimeter clusters excluding the ρ and π_s. Set 2 : Created from Set 1 by removing particles that are consistent with originating from the decay of the $\overline{D}^0$. Here we take advantage of the fact that the $\overline{D}^0$ has a substantial boost in the CM frame, hence its decay products tend to lie in a cone around its direction of flight Sec.5.2.2. Particles that lie within a 1.25 rad cone around $\vec{P}_{D^0}$ are removed from Set 2 . The variables used in $\mathcal{F}$ are:

- The CM energy flow in nine, 10°-wide cones around $\vec{p}_\rho$, computed with Set 1.
- The sphericity of Set 1.
- $|\cos\theta_{sp}|$, where θ_{sp} is the angle between $\vec{p}_\rho$ and the sphericity axis of Set 2.
- The angle between $\vec{p}_\rho$ and the highest momentum particle in Set 2.

- The invariant mass of Set 2.
- The absolute momentum of Set 2.
- The angle between the total Set 2 momentum and $\vec{p}_\rho$.

The sphericity axis $\vec{s}$ of a set of momentum vectors, $\mathcal{P}$, is the unit vector for which the quantity $\sum_i |\vec{p} \times \vec{s}|^2$ is a minimum value.

Since continuum events typically contain two almost back-to-back jets Fig. 4.5, $|\cos\theta_{sp}|$ tends to be close to one. In $B\bar{B}$ events there is, in general, no correlation between the decay of the two B^0 meson distributions, thus these events are distributed more or less equally in all possible values of $|\cos\theta_{sp}|$.

None of the seven variables described above are a good discriminant between signal and background events by themselves, hence in order to enhance the discriminating power of these variables, they are combined into a Fisher discriminant. The Fisher discriminant is a linear combination of seven input variables: $\mathcal{F} = \sum_{i=1}^{7} \alpha_i x_i$, where the coefficients (or the weights) α_j are defined by [36]

$$\alpha_j \equiv \sum_{i=1}^{7} (U_{ij}^{\rm sig} + U_{ij}^{\rm bkg})^{-1} \times (\mu_i^{\rm bkg} - \mu_i^{\rm sig}). \tag{4.13}$$

where $U_{ij}^{\rm sig}$ and $U_{ij}^{\rm bkg}$ are the covariance matrices for the input variables for signal and background, respectively, and $\mu_i^{\rm sig}$ and $\mu_i^{\rm bkg}$ are the mean values of the x_i's.

The coefficients of the Fisher discriminant are determined using signal Monte Carlo

and off-resonance data to provide a background sample. The Fisher discriminant for signal and continuum events is shown in Fig. 4.7.

4.3.4. Event Selection for Fully Reconstructed Events

Fully reconstructed events are fit simultaneously with partially reconstructed events. Being a cleaner sample of events they help better distinguish a signal event from a background one. Fully reconstructed B^0 candidates are reconstructed in the $\overline{D}^0$ decay modes $K\pi$ and $K\pi\pi^0$ (see Sec. 7.1.6 for the reason for dropping the $K\pi\pi\pi$ mode). Two kinematic variables are calculated for each candidate event: the so called beam-energy substituted mass, $m_{\rm ES}$, and the energy difference, ΔE defined by:

$$\begin{aligned} m_{\rm ES} &\equiv \sqrt{\frac{\left(\frac{1}{2}s + \vec{p_0}\cdot\vec{p_1}\right)^2}{E_0^2} - p_1^2}, \\ \Delta E &\equiv \frac{2q_0\cdot q_1 - s}{2\sqrt{s}}, \end{aligned} \tag{4.14}$$

where $q_0 \equiv \{E_0, \mathbf{p_0}\}$ is the four-momentum of the initial state for the process $e^+e^- \rightarrow B\bar{B}$, $q_1 \equiv \{E_1, \mathbf{p_1}\}$ and $q_2 \equiv \{E_2, \mathbf{p_2}\}$ are the four-momenta of the B^0 mesons, and $s \equiv q_0^2 = (q_1 + q_2)^2$ is the CM energy squared. In the center of mass frame, $m_{\rm ES}$ and ΔE are given by:

$$m_{\rm ES} = \sqrt{(E^*_{\rm beam})^2 - (\sum_i \vec{p}^*_i)^2}$$

$$\Delta E = \sum_i \sqrt{m_i^2 + (\vec{p}_i^*)^2} - E^*_{\rm beam}. \quad (4.15)$$

where $E^*_{\rm beam}$, m_i and $\mathbf{p}^*_i$ are the beam energy, mass and momentum, respectively in the CM frame, of the i$^{\rm th}$ constituent particle of the B^0 candidate. For a properly reconstructed B^0 candidate, the beam-energy substituted mass, $m_{\rm ES}$, peaks at the B^0 mass with a resolution of the order of a few MeV/c^2, and ΔE peaks at zero with a resolution of approximately 20 MeV. These variables are discussed in detail in [37].

The fully reconstructed events are selected by applying the following selection criteria:

- $0.142\,{\rm MeV/c^2} < |m(D^{*+}) - m(D^0)| < 0.150$ MeV/c^2.
- $|\Delta E| < 50$ MeV.
- $m_{\rm ES} > 5.25$ GeV/c^2.
- It is required that π_f, the charged daughter of the ρ identified by partial reconstruction, be the same track identified by full reconstruction. No such requirement is applied to the π_s or π^0. Thus, although partial reconstruction may be imperfect for a fully reconstructed event, the identified π_f will point back to the decay point of the B^0 (see Sec. 5.1.3).

In events that contain more than one fully reconstructed candidate, the candidate with the smallest value of $|\Delta E|$ is chosen.

4.3.5. Particle Identification (PID)

Information on particle identification comes from several sub-systems. This is then put together by the experts belonging to the sub-systems by applying certain cuts to optimize the performance of the detector with respect to selecting a particle with as high an efficiency and as low a misidentification as possible. In the following subsections we present a very brief description of particle identification, and point to references for detailed reading.

Kaon Identification

The selection criteria used to separate kaons from pions and protons are:

$$\mathcal{L}_K > r_\pi \mathcal{L}_\pi \text{ and } \mathcal{L}_K > r_p \mathcal{L}_p. \tag{4.16}$$

where $\mathcal{L}_K$, $\mathcal{L}_\pi$, $\mathcal{L}_p$ is the total likelihood for the kaon, pion and proton hypothesis respectively. The values of r_π and other parameters used for "tight" kaon selection are summarized in Table 4.3. A detailed description of the kaon selector can be found in reference [38].

Electron Identification

The variables used to separate electrons from pions and muons are: the ratio of the energy, E, deposited in the calorimeter to the track momentum, p, E/p; the energy

Table 4.3: tight kaon identification requirements

Sub-System	Momentum range (GeV/c)
Silicon Vertex Tracker	< 0.7
Drift Chamber	< 0.7
Cherenkov detector	> 0.7
Momentum (GeV/c)	r_π
< 2.7	1
> 2.7	80
$0.5 < p < 0.7$	15

loss due to ionisation in the silicon vertex detector and the drift chamber per unit length, dE/dx; lateral energy distribution, LAT; Zernike moment, A_{42}; the measured Cherenkov angle, $\theta_{\rm C}$, of the e^+. The cuts are summarized in Table 4.4. A detailed description of the e selector can be found in reference [39].

Table 4.4: tight electron identification requirements.

Parameter	cuts
E/p	$0.75 < E/p < 1.3$
no. of crystals	> 3
dE/dx	$500.0 < dE/dx < 1000.0$
LAT	$0.1 <$ LAT < 0.6
A_{42}	$-10 < A_{42} < 10$
$\lvert\theta_{\rm C} - \theta_{\rm C}^{\rm exp}\rvert$	$< 3\sigma$

Muon Identification

The variables used to separate μ from e and π are: the energy deposited in the calorimeter, E; the number of IFR layers in a cluster matched to the muon candidate, $\mathrm{N_L}$; the measured and expected interaction lengths, λ and λ_{exp} and their difference $\Delta\lambda$; the average multiplicity of strips hit per layer of the instrumented flux return, $\overline{\mathrm{m}}$; its standard deviation, σ_{m}, the χ^2 of the track. The cuts are summarized in Table 4.5. A detailed description of the μ selector can be found in reference [40]:

Table 4.5: tight muon identification requirements.

Parameter	cuts
E	$0.05 < E < 0.4$ GeV
$\mathrm{N_L}$	≥ 2
$\Delta\lambda$	< 1
λ	> 2.2
χ^2_{trk}	< 5
χ^2_{fit}	< 3
$\mathrm{T_c}$	> 0.3
$\overline{\mathrm{m}}$	< 8
σ_{m}	< 4
K veto	tight

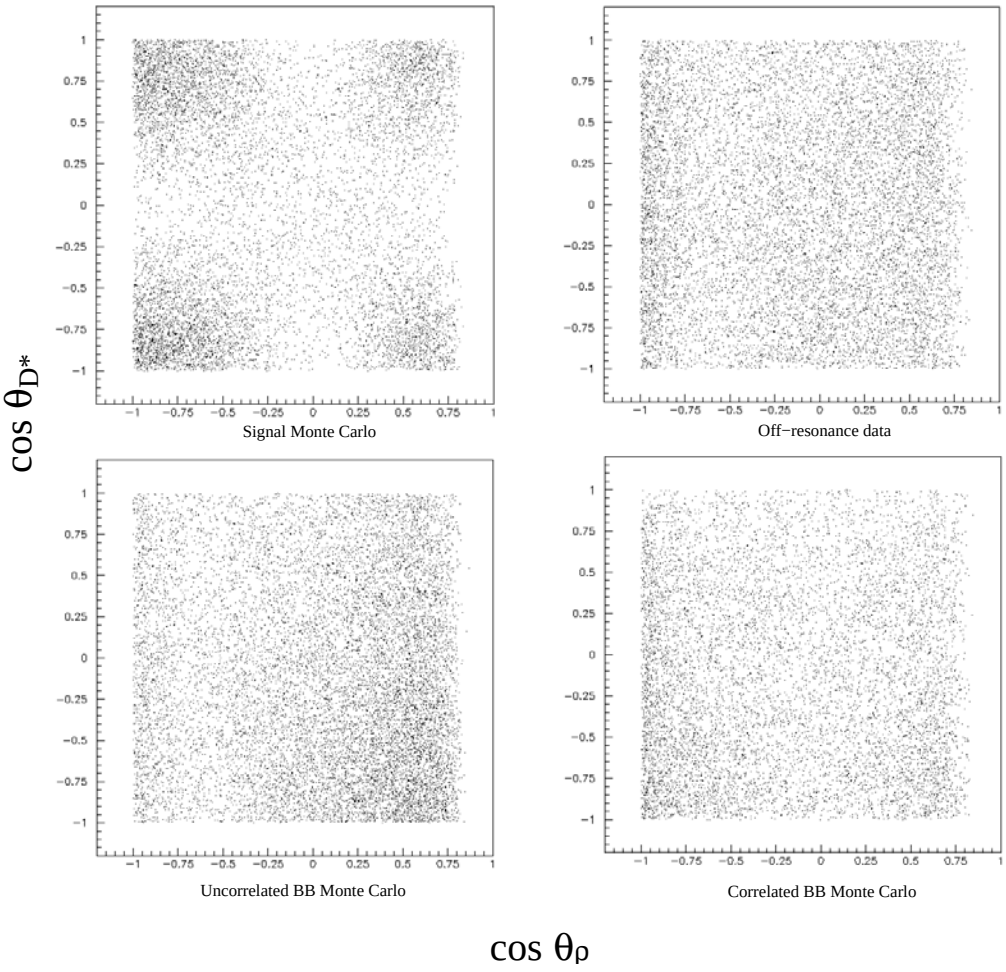

Figure 4.6: $\cos\theta_{D^*}$ *vs.* $\cos\theta_\rho$ distributions of (clockwise from top left) Monte Carlo signal events, off-resonance data, Monte Carlo correlated backgrounds (see section 6.4) and uncorrelated Monte Carlo generic $B\bar{B}$ events. $\cos\theta_\rho < 1$ due to the requirement $|\vec{p}_{\pi^0}| > 0.4$ GeV/c. The polarization generated in the signal Monte Carlo is based on the CLEO polarization measurement [35].

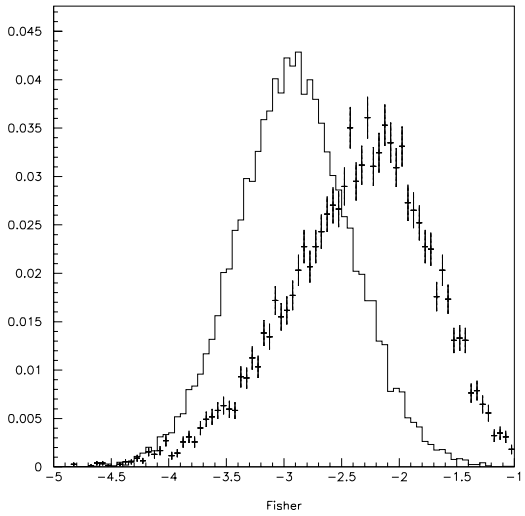

Figure 4.7: Fisher variable distribution for Monte Carlo signal (solid histogram) and continuum data (dotted histogram).

Chapter 5

Decay Time Difference

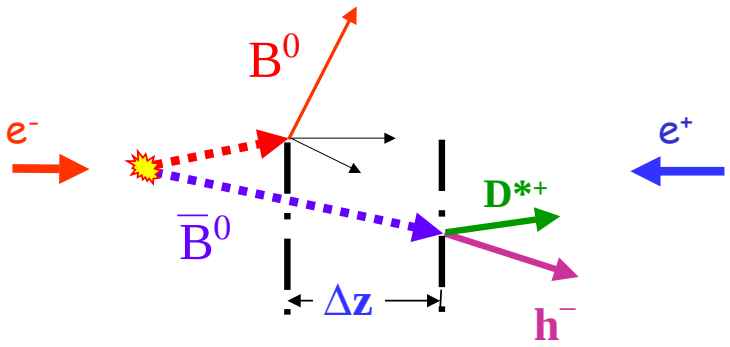

Figure 5.1: Event topology. Figure not drawn to scale.

The primary motivation for an asymmetric B factory is that the B mesons are Lorentz boosted. With the boost $\beta\gamma \approx 0.55$ their typical flight path along z is approximately 260 μm, compatible with the experimental resolution of 130 μm. If it were not for the boost the flight length of the B^0 with the small kinetic energy from

the $\Upsilon(4S)$ decay would be approximately 30 μm, much smaller than the experimental resolution. Hence to measure the $\mathcal{CP}$ asymmetries or the B^0 lifetime it is necessary to have an asymmetric e^+e^- collider. The $\Upsilon(4S)$ decays at some unknown point inside the beam spot, which has a spread along the z axis of 80 mm, the y axis of 35 μm and the x axis of 5 μm, to $B\bar{B}$ mesons, and the decay length of the individual B^0 meson is unknown. Therefore the lifetime of the B^0 meson is determined from the difference between the decay lengths of the two B^0 mesons. The topology of the events is sketched in Fig 5.1, it is not drawn to scale.

The z axis of the *BABAR* coordinate system is defined to be parallel to the magnetic field of the solenoid [41]. Suppose the boost is parallel to the z axis and the B^0 mesons are produced at rest in the CM frame. We define z_{rec} and z_{other} as the z coordinate of the decay points of the partially reconstructed B^0 and the other B^0 respectively. Then $\Delta z = z_{rec} - z_{other}$ is defined as the signed decay length difference. Under the above assumption, $\langle|\Delta z|\rangle = (\beta\gamma)c\tau_B$, where β is given by Eq. 5.18, and γ is calculated from β.

Complications arise for several reasons, for example: the energies of the beam fluctuate giving the $\Upsilon(4S)$ momenta a Gaussian distribution with a standard distribution of 6 MeV. The B^0 mesons are not produced at rest in the $\Upsilon(4S)$ frame ($\langle p_B^{CM}\rangle = \sqrt{E_{e^+} + E_{e^-} - M_B^2} \approx 340\,\mathrm{MeV}$) resulting in a non-vanishing opening angle (smaller than 215 mrad [15]) between the trajectories of the B^0 and the $\overline{B}^0$ mesons.

In practice, all these effects are small compared to the experimental resolution on Δz.

We reconstruct Δz and then calculate Δt for each event (see Sec. 5.3.1). From the Δt distribution the B^0 lifetime is extracted as explained in Sec. 7.1. In the following section we describe the reconstruction of z_{rec} and z_{other}.

5.1. Determination of Partially Reconstructed B^0 Decay Vertex, z_{rec}

5.1.1. General Vertexing Formalism

The algorithm used to reconstruct z_{rec} in *BABAR* (GeoKin algorithm) is based on a generalized least square method using the Lagrange Multiplier technique [42]. In this method it is assumed that the constraint equations can be linearized and represented by three matrices, $\tilde{A}, \tilde{B}, \vec{c}$.

Let $\vec{\eta}$ represent the measurable quantities(n-vectors). The actual measured quantities $\vec{y}$ (for example the measured track parameters) deviate from $\vec{\eta}$ by errors $\vec{\delta}$. We assume that these errors are normally distributed about the measured value. We then group the r unknowns (for example the vertex position) into a vector, $\vec{x}$. The m constraint functions that relate $\vec{x}$ and $\vec{\eta}$ are given by:

$$f_k(\vec{x}, \vec{\eta}) = f_k(\vec{x}, \vec{y} + \vec{\delta}) = 0, k = 1, .., m. \tag{5.1}$$

If the function f_k can be linearized at $\vec{x} = \vec{x}_0$ and $\vec{\eta} = \vec{\eta}_0$, then the χ^2 can be expressed

as [42].

$$\chi^2 = \delta^T \tilde{W}_y \delta + 2\mu^T(\tilde{A}\vec{\psi} + \tilde{B}\vec{\delta} + \vec{c}). \tag{5.2}$$

where μ is a vector of Lagrange multipliers, and

$$\vec{\psi} = \vec{x} - \vec{x}_0. \tag{5.3}$$

$$\vec{\delta} = \vec{\eta} - \vec{\eta}_0. \tag{5.4}$$

and $\tilde{W}_y$ is the weight matrix of the parameter, $\vec{y}$.

$$a_{kl} = (\frac{\partial f_k}{\partial x_l})_{\vec{x}_0,\vec{\eta}_0} = \tilde{A}. \tag{5.5}$$

$$b_{kl} = (\frac{\partial f_k}{\partial \eta_l})_{\vec{x}_0,\vec{\eta}_0} = \tilde{B}. \tag{5.6}$$

$$\vec{c}_k = f_k(\vec{x}_0, \vec{\eta}_0). \tag{5.7}$$

The matrices, $\tilde{A}$ and $\tilde{B}$, are the derivatives of the constraints with respect to the unknown ($\vec{x}$) and the parameter ($\vec{\eta}$) respectively, and are estimated at the point $\vec{x}_0$ and $\vec{\eta}_0$. $\vec{c}$, is a vector of values of the constraints at the point $\vec{x}_0$ and $\vec{\eta}_0$.

The χ^2 in Eq. 5.2 is minimized. As a first approximation, we take, $\vec{\eta}_0 = \vec{y}$, and also

require an expansion about $\vec{x}_0$. By doing so we estimate the initial vertex coordinate.

If Eq. 5.1 is a linear equation, the final solution can be calculated in a single iteration. In general, the constraints are not linear and hence a better approximation method is needed and several iterations are required before a satisfactory result is obtained. The calculated covariance matrix has a physical meaning and can be used to estimate errors on any of the vertex fit parameters.

A detailed description of the algorithms used for vertexing can be found in reference [43].

5.1.2. Constraint

The only constraint condition used in the fit to the z_{rec} vertex in this analysis is the beam spot constraint which is a χ^2 constraint.

Beam Spot Constraint: The vertex position in the transverse (x,y) plane, is constrained to be compatible with the beam-spot position

$$(x - x_{BS})^2 + (y - y_{BS})^2 = 0. \tag{5.8}$$

As this is a χ^2 constraint, (x_{BS}, y_{BS}) are introduced as additional parameters in the fit, so that their covariance matrix can be used to account for the actual size of the beam.

5.1.3. Reconstruction of the $B^0 \to D^{*-}\rho^+$ Vertex

The z_{rec} vertex is obtained by using the charged pion daughter of the ρ, the π_f, and the beam spot constraint. As this constraint is applied to the B^0 decay point rather than the $\Upsilon(4S)$ decay point, the beam spot calculation takes into account the small transverse flight of the B^0 in the CM frame due to the finite lifetime of the B^0 and the small energy release in $\Upsilon(4S) \to B^0\overline{B}^0$ decay. (The beam-spot is obtained using `event-Info->beamSpotBFlight()`.) The fit for the z_{rec} vertex is done using the GeoKin algorithm, as described in Sec. 5.1.1 thus yielding the z position of the partially reconstructed B^0 meson.

The π_s from the decay of the D^* is not used in the vertex fit because signal events may be misreconstructed if the π_f or the π_s, or both, may be misidentified. If both of these tracks are used to fit for the vertex, it will result in a complicated variety of misreconstruction effects on the measured lifetime, thus using only the π_f simplifies the treatment of these effects, as outlined in Sec. 6.4. In addition, due to the low momentum of the π_s (approximately 200 MeV in CM frame) the effects of multiple scattering are large. The resolution of z_{rec} determined from Monte Carlo is 130 μm. It is obtained by fitting the residue, $\Delta z_{rec} = z_{rec} - z_{rec-truth}$ to the sum of two Gaussians as shown in Fig. 5.2. To check for consistency between the measured resolution and the per-event error in the measurement of z_{rec}, σ_{zrec}, we define the pull of z_{rec} as $\frac{\Delta z_{rec}}{\sigma_{zrec}}$, and is shown in Fig. 5.3. As Δz_{rec} is a measure of σ_{zrec}, for a properly

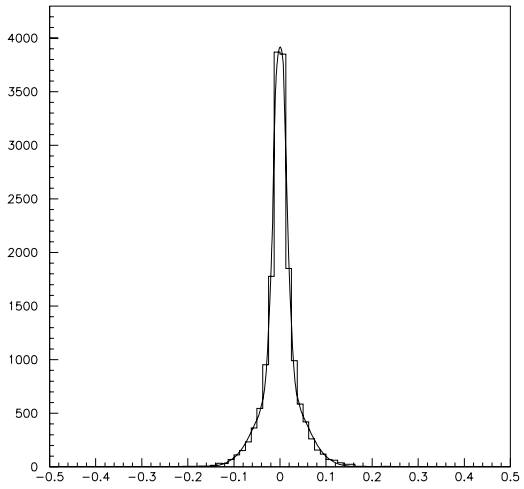

Figure 5.2: Resolution of the z_{rec} vertex obtained from Monte Carlo.

reconstructed vertex one expects the pull of the z_{rec} distribution to be approximately one. This distribution is fit to the sum of two Gaussians, where approximately 89 % of the events lie in the core Gaussian. The core Gaussian has a width of 0.91 as expected, thereby validating the procedure for the reconstruction of the z_{rec} vertex.

5.2. Determination of the Other B^0 Vertex, z_{other}

5.2.1. Vertex Algorithm for the Other B^0

The other B^0 decay vertex labeled as z_{other} is reconstructed with the charged tracks in the event excluding those that belong to the partially reconstructed B^0, B_{rec}. To retain high efficiency the other B^0 is reconstructed using partial reconstruction. The other B^0 vertex reconstruction is difficult because secondary tracks from short

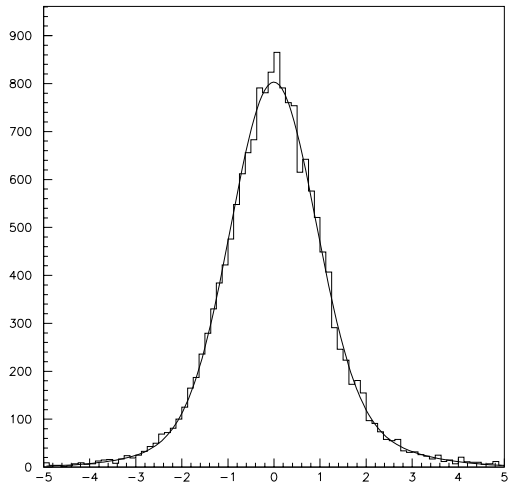

Figure 5.3: Pull of the z_{rec} vertex obtained from Monte Carlo.

and long lived particles tend to bias the vertex position. The algorithm tries to minimize this effect by using the following strategy: start with a list of charged tracks in the event, except those that come from B_{rec} decay; remove charged tracks from reconstructed composites (V^0) such as K^0_S and Λ to reduce the bias in the vertex and outliers in the resolution; retain only those V^0 that decay close to the IP; fit for z_{other} using the GeoKin algorithm, Sec 5.1.1, to a common vertex; if the fit is bad, ($\chi^2 > \chi^2_{cut}$) remove the candidate that contribute the largest to the χ^2 and try the fit again. The algorithm that does this in *BABAR* is called VtxTagBtaSelFit

The parameters used in this procedure are :

- position and momentum of other B^0 candidates : $(x, y, z, p_x, p_y, p_z)_i$,i=1,.....,n, where n is the total number of recoiling candidates.

- position of the interaction point in the transverse plane : $(x_{\Upsilon(4S)}, y_{\Upsilon(4S)})$.
- the three-momenta of the beams: $(p_{x,e^-}, p_{y,e^-}, p_{z,e^-}), (p_{x,e^+}, p_{y,e^+}, p_{z,e^+})$.

The unknowns are : position and momentum of the other B^0 :

- $(x_{other}, y_{other}, z_{other}, p_{x,other}, p_{y,other}, p_{z,other})$.

The only constraint that is used is the beam-spot constraint.

The iterative procedure is applied until no track has a contribution of more than six units to the χ^2 or only n tracks remain, where n (which can be zero) is a parameter that can be tuned. In general, n should be greater than 1, as studies have shown that a large fraction of the poorly reconstructed vertices contributing to a worse Δz resolution is due to events that were reconstructed using a single track.

5.2.2. Rejection of D^0 Tracks

The other B^0, B_{other}, vertex z_{other} is reconstructed from the tracks in the event that do not belong to the partially reconstructed B^0, B_{rec}. Since the D^0 in $B^0 \to D^{*-}\rho^+$ decay is not reconstructed it is necessary to remove the tracks coming from the D^0 decay before reconstructing z_{other} vertex. Inclusion of the D^0 tracks in z_{other} vertex reconstruction may pull the z_{other} vertex close to the z_{rec} vertex thereby biasing Δz, and hence the lifetime to smaller values.

In order to remove the tracks that belong to the decay of the D^0, without full reconstruction of the D^0 decay, an assumption that all the decay products are pro-

duced in a cone around the momentum direction of the D^0 in the CM frame is made. The size of this cone determines the efficiency and purity of the method of partial reconstruction. Thus $\vec{p}_{D^0}$ needs to be calculated. We define an angle $\theta_{D^*\rho}$ of the D^* direction with respect to the opposite direction of the ρ, about the $-\vec{z}$ axis, Fig. 4.2. By applying four-momentum conservation to the decay of the B^0 we get

$$\cos\theta_{D^*\rho} = \frac{-(M_B^2 - M_{D^*}^2 - M_\rho^2 - 2E_B E_\rho)}{2|\vec{p}_{D^*}||\vec{p}_\rho|}. \tag{5.9}$$

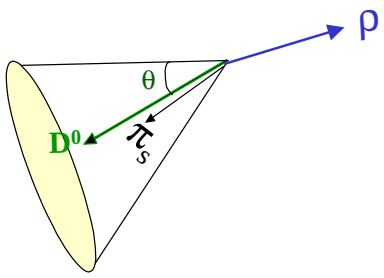

Figure 5.4: A schematic representation of the cone-cut. In this analysis we use $\theta = 1$ rad.

This gives a cone of possible D^* direction around the $-\vec{z}$ axis. Applying four-momentum conservation in the decay of the D^* we get:

$$\vec{p}_{D^0} = \vec{p}_{D^*} - \vec{p}_{\pi_s}. \tag{5.10}$$

and again from Fig. 4.2 we have :

$$\vec{p}_{\pi_s} = |\vec{p}_{\pi_s}|(\cos\alpha\vec{z} + \sin\alpha\vec{y}). \tag{5.11}$$

$$\vec{p}_{D^*} = |\vec{p}_{D^*}|(-\cos\theta_{D^*\rho}\vec{z} + \sin\theta_{D^*\rho}\cos\phi_{D^*}\vec{x} + \sin\theta_{D^*\rho}\sin\phi_{D^*}\vec{y}). \tag{5.12}$$

By squaring Eq. 5.10 and using Eq. 5.11 and Eq. 5.12 we get :

$$\sin\phi_{D^*} = \frac{\frac{M^2_{D^0} - M^2_{D^*} - M^2_\pi + 2E_{D^*}E_\pi}{2|\vec{p}_{D^*}||\vec{p}_\pi|} - \cos\theta_{D^*\rho}\cos\alpha}{\sin\theta_{D^*\rho}\sin\alpha}. \tag{5.13}$$

Thus from Eq. (5.13) and

$$\cos\phi_{D^*} = \pm\sqrt{1 - \sin\phi^2_{D^*}}. \tag{5.14}$$

there are two solutions for $\vec{p}_{D^*}$, which then yields two possible directions for $\vec{p}_{D^0}$, Eq. (5.10).

We exclude all tracks that lie within a one-rad cone around the two directions of D^0. This cut is referred to as the "cone-cut". A pictorial representation of a cone-cut is shown in Fig. 5.4. For stability studies we use four other cone-cuts that have values: 0.6, 0.8, 1.2, 1.4 rad

5.2.3. Reconstruction of the Other B^0 Vertex

The selection of tracks used in the determination of z_{other} is described in Sec. 5.2.2. The z_{other} vertex is obtained using the standard *BABAR* module, VtxTagBtaSelFit.

The resolution of the z_{other} depends on the number of tracks used by the fit. To achieve a high vertex quality it is required that the fit be performed with at-least two tracks, i.e. $n \geq 2$.

A possible background arises from the tracks from the decay of the charm hadrons. These tracks are generally at large z due to the charm hadron lifetime and the boost, and their net effect is to produces a bias in the mean value of z_{other} coordinate on the order of 20 μm. The resolution of z_{other} determined from Monte Carlo is

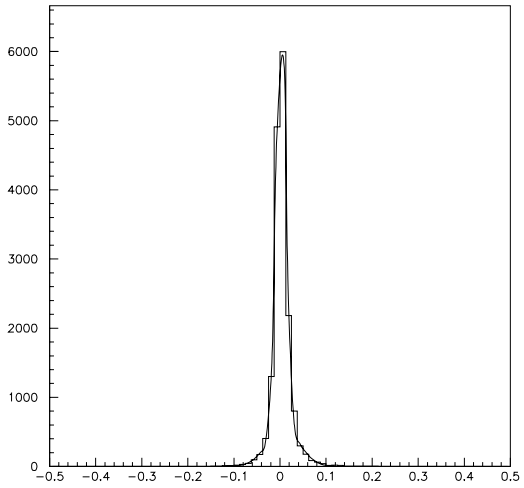

Figure 5.5: Resolution of the z_{other} vertex obtained from Monte Carlo.

108 μm. It is obtained from a fit to the residue, $\Delta z_{other} = z_{other} - z_{other-truth}$ to the

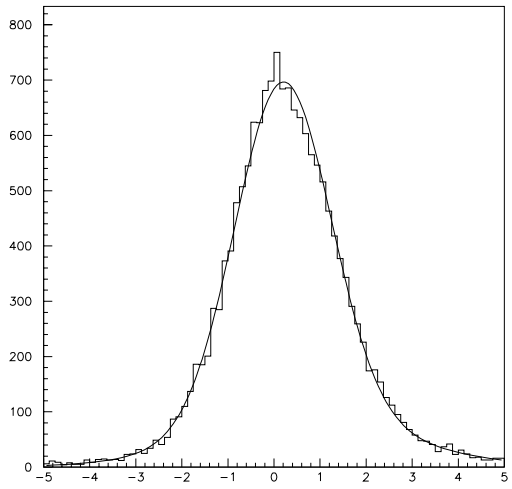

Figure 5.6: Pull of the z_{other} vertex obtained from Monte Carlo.

sum of two Gaussians as shown in Fig. 5.5. To check for consistency between the measured resolution and the per-event error in the measurement of z_{other}, σ_{zother} we define the pull of z_{other} as $\frac{\Delta z_{other}}{\sigma_{zother}}$ and is shown in Fig. 5.6. This distribution is fit to the sum of two Gaussians, where approximately 90% of the events lie in the core Gaussian which has a width of 1.04 as expected, thereby validating the procedure for the reconstruction of the z_{other} vertex.

5.3. Δz and Δt Reconstruction

Having obtained the vertex of the partially reconstructed B^0 and the other B^0, we define the decay length difference as

$$\Delta z = z_{rec} - z_{other}. \tag{5.15}$$

and from Δz the decay length time difference is calculated.

In order to optimize the resolution on Δt further cuts are applied:

- The π_f-beam-spot vertex probability be greater than 1%.
- The decay length time difference between the two B^0 mesons, $|\Delta t| < 15$ ps.
- The per-event error on Δt, $0.3 < \sigma_{_{\Delta t}} < 4$ ps.

Less that a percent of events had $\sigma_{_{\Delta t}} < 0.3$. It is possible that the per-event error calculation of these vertices are wrong, hence as a pre-caution we require $\sigma_{_{\Delta t}} > 0.3$.

5.3.1. Δz to Δt Transformation

In order to estimate Δt for each event, we note that the distance Δz can be written in terms of t_{rec} and t_{other} as [43]:

$$\Delta z = \beta\gamma\gamma^*_{rec}c(t_{rec} - t_{other}) + \gamma\beta^*_{rec}\gamma^*_{rec}\cos\theta^*_{rec}c(t_{rec} + t_{other}). \tag{5.16}$$

γ^*_{rec}, β^*_{rec} and $\cos\theta^*_{rec}$ are respectively, the boost factor, velocity and angle with respect to the beam direction of the fully reconstructed B^0 in the $\Upsilon(4S)$ frame. The derivation of the above expression uses the fact that the two B^0-mesons are back-to-back in the CM frame.

As $t_{rec} + t_{other}$ are unknown on an event by event basis, some average value must be used. However under the assumption that the experiment has no polar angle bias and neglecting the event-by-event variation of $t_{rec} + t_{other}$ (due to changes in Δt), $\langle \cos\theta^*_{rec} \rangle = 0$, so on average the second term in Eq. 5.16 vanishes. If we also neglect the small kinetic energy release in $\Upsilon(4S) \to B\bar{B}$ decay, we have $\gamma^*_{rec} = 1$. Using these two assumptions we get :

$$\Delta t = \Delta z / \gamma\beta c. \tag{5.17}$$

where γ is the boost factor of the $\Upsilon(4S)$ in laboratory frame and β its velocity calculated using the beam energies:

$$\beta = \frac{E_e - E_p}{E_e + E_p}. \tag{5.18}$$

where E_e is the energy of the electron beam (9 GeV) and E_p is the energy of the positron beam (3.1 GeV).

Compared to the experimental resolution on Δz, the effects on Δt produced by the approximation (Eq: 5.17) is small. The bias and the systematic error introduced

by this approximation has been studied in [44] and [45]. In particular, [45] has shown analytically that for B^0 lifetime measurements the bias introduced by this approach is about 0.4 %, which is small compared to the other systematic errors in this analysis, Sec. 10.1.

The error introduced in the measurement of the lifetime due to the variations in the beam energies used in the calculation of the boost is discussed in Sec. 10.1.9.

5.3.2. Δt Per-Event Error

In addition to providing a measurement of Δz, the algorithm described above also provides an error estimate for Δz, $\sigma_{\Delta z}$. The distributions of $\sigma_{\Delta t}$ for data, is shown in Fig. 5.7. It is fit to a Crystal Ball function [46] plus a Gaussian. A Crystal Ball function is a Gaussian signal peak matched to a power law tail. Time-dependent studies using fully reconstructed B^0 [47] have shown that $\sigma_{\Delta t}$ is correlated with the width of the residual $(\Delta t - \Delta t_{true})$ distribution as shown in Fig. 5.8. A similar correlation is also expected in this analysis. To account for this dependence on $\sigma_{\Delta t}$, the resolution function (Sec.7.1.5) parameterization of Δt for each event should depend on both Δt and $\sigma_{\Delta t}$, $\mathcal{R}(\Delta t, \sigma_{_{\Delta t}})$.

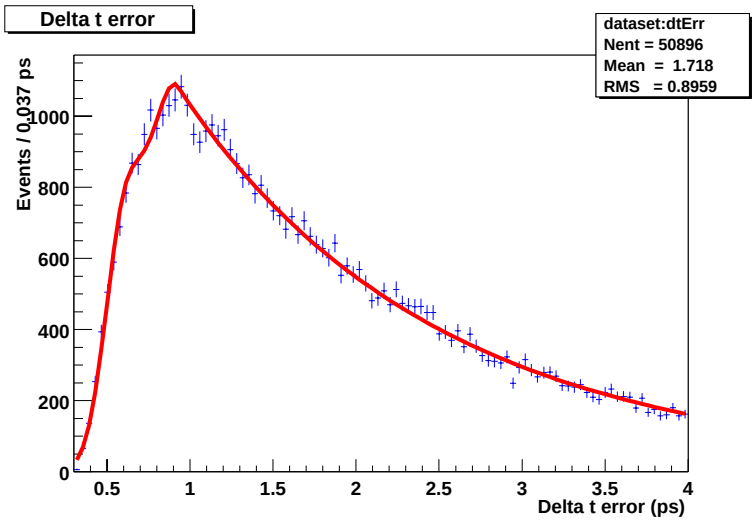

Figure 5.7: Distribution of $\sigma_{\Delta t}$ for data. The solid line is a fit to $\sigma_{\Delta t}$ using the Crystal Ball function plus Gaussian.

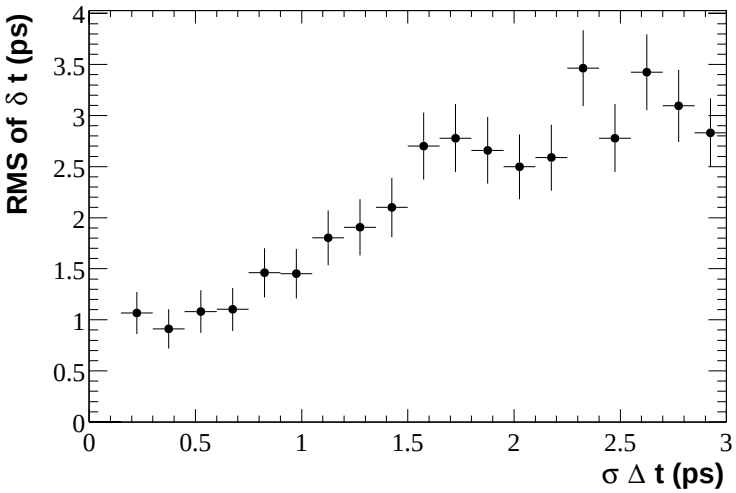

Figure 5.8: RMS of the residual $(\Delta t - \Delta t_{true})$ distribution plotted for various bins of $\sigma_{\Delta t}$.

Chapter 6

Data and Monte Carlo Samples

6.1. Introduction

This chapter contains a description of data and Monte Carlo simulation samples used in this analysis. It also contains the definitions of the various event types referred to in this analysis.

6.2. Data Sample

The data set used for this analysis was collected during the 1999-2000 data taking period, referred to as the "Run 1" data. *BABAR* divides its data into runs, defined as periods of three hour duration or less during which the beam and detector conditions are judged stable. This period consisted of 3371 runs with run numbers in the range 9931-17106. The total integrated luminosity, $\mathcal{L}$, ($\mathcal{L} = \frac{\#events}{cross-section}$) of the sample taken on the $\Upsilon(4S)$ peak, known as "on-resonance" data, is $(22.7 \pm 0.4) \times 10^6$ $B\bar{B}$

pairs [48]; this corresponds to 20.6 fb^{-1} of data. This data is divided into two blocks according to the drift chamber high voltage settings, which was raised from 1900 V to 1960 V, approximately in the middle of the Run1 data taking period. Table 6.1 lists the integrated luminosity for each block. Some data was taken 40 MeV below the peak of the $\Upsilon(4S)$ resonance, known as the "off-resonance" data, to provide a sample of continuum data ($e^+e^- \to q\bar{q}$, where $q = u, d, s$ or c). The integrated luminosity of this off-resonance sample is 2.6 fb^{-1}.

The data (on and off the $\Upsilon(4S)$ peak) is sub-divided into four sets according to the four software alignment configurations of the silicon vertex tracker. These configurations were necessary to remove the misalignment of the silicon vertex tracker with respect to the drift chamber in the track reconstruction stage. This optimizes the tracking and vertexing performance of the sub-detectors. These sets are referred to as Alignment Sets A, C, D, E. Table. 6.2 gives the break up of the Run-1 data in these four alignment sets.

Only good runs, as flagged by the *BABAR* data quality monitoring processes, are used in this analysis. The main criteria for the goodness of a run is the status and performance of all the sub-detectors, the running condition of the beams, and the total luminosity of the run.

Table 6.1: The composition of the 1999-2000 on-peak data sample. Roughly half of the data was taken with the high voltage (HV) of the drift chamber set at 1900 V, and the other half, with the voltage raised to 1960 V.

Block	DCH HV	$\mathcal{L}$ (fb^{-1})
1	1900 V	11.2
2	1960 V	9.4
TOTAL		20.6

Table 6.2: Break-down of the data into different alignment sets. The distribution of the data taken during the year 1999-2000 into different alignments sets.

	on-resonance	off-resonance
Alignment Set	$\mathcal{L}$ (pb^{-1})	
A	452	0
C	3163	332
D	5688	555
E	11361	1690

6.3. Monte Carlo Samples

The GEANT3-based [49] Monte Carlo simulation used in this analysis was produced in a simulation cycle called Simulation Production # 3 (SP3). It will be often referred to as the "SP3 Monte Carlo simulation" or just the "Monte Carlo simulation".

The generic SP3 Monte Carlo samples include $B\bar{B}$ events, with approximately equal number of $B^0\bar{B}^0$ and B^+B^- events; continuum $c\bar{c}$ events; and continuum uds events. These samples are used extensively to perform data/simulation comparisons.

For this purpose, the Monte Carlo samples need to be scaled to data luminosity. The scaling factor F_{sc} is calculated in the following way. If N_{sam} is the number of Monte Carlo events in a given sample (*e.g.*, the number of generic $B\bar{B}$ events), then:

$$F_{sc} = \frac{\sigma_{sam}\,\mathcal{L}}{N_{sam}}, \tag{6.1}$$

where $\mathcal{L}$ is the integrated luminosity and σ_{sam} is the cross-section for the process in question. The number of events in each generic SP3 Monte Carlo sample, as well as the scaling factors and the cross-sections used in Eq. 6.1, are listed in Table 6.3.

Table 6.3: Number of events in the generic Monte Carlo samples and scaling factors for data/Monte Carlo comparison. The number of events in the generic $B\bar{B}$ and continuum *udsc* SP3 Monte Carlo. Cross-sections σ and scaling factors F_{sc} used for data/Monte Carlo comparison are also given.

SP3 Sample	no. of Events	σ (nb)	F_{sc}
Generic $B\bar{B}$	8,436,700	1.11	2.72
Continuum $c\bar{c}$	12,086,400	1.35	2.54
Continuum *uds*	19,475,900	2.04	2.41

6.4. Event Types

The high level of the background constitutes the greatest complication to this analysis. Signal and background event types are classified according to their contribution to the B^0 lifetime measurement and the availability of data control samples.

The various events types are classified as follows:

- Signal $B^0 \rightarrow D^{*-}\rho^+$ events. This may include some non-resonant $B^0 \rightarrow D^{*-}\pi^+\pi^0$ events. In some of these events the π^0 and/or π_s is mis-reconstructed, but they are considered "signal" because they peak in the $m_{\rm miss}$ region and their fast pion, π_f (the daughter of the ρ), correctly points to the decay point of the B^0, B_{rec}.

- $B^0 \rightarrow D^{*-}a_1^+$ events. They constitute about 11.6% of the $B^0 \rightarrow D^{*-}\rho^+ + B^0 \rightarrow D^{*-}a_1^+$ sample. Since they come from a B^0 they have the correct lifetime information, hence these events are used along with the signal events to determine the B^0 lifetime.

- Peaking $B^0\overline{B}^0$ background. They are $B^0 \rightarrow D^{*-}\rho^+$ or $B^0 \rightarrow D^{*-}a_1^+$ events, in which the track associated with the fast pion, π_f, actually originates from the other B, B_{other}. This results in the measurement of a zero decay distance, $\Delta z = 0$. Due to the kinematics of these events they peak in the signal region of the missing mass distribution.

- Combinatoric $B\overline{B}$ background: These events do not peak in the signal region of the missing mass distribution but due to random combinations they satisfy the kinematic requirement for signal events. These events are potentially the most dangerous background as they have a lifetime which is compatible to the

lifetime as measured from $B^0 \to D^{*-}\rho^+$ events.

- $\overline{B} \to D^{**}\rho^+$: These events are $B^0 \to D^{**}\rho$ where the $D^{**} \to D^*X$. If X is not reconstructed these events will fake signal events. These events peak in the signal region of the missing mass distribution.

- Continuum background. These events are light quark initiated events which satisfy the criteria for signal events and do not peak in the signal region of the missing mass distribution.

Chapter 7

Unbinned Maximum Likelihood Fit

7.1. Introduction

The technique to measure the B^0 meson lifetime, τ_B, is outlined in Sec. 5. We reconstruct Δt for each of the selected events and extract τ_B from the Δt distribution using an unbinned maximum likelihood fit. The fits were performed using the standard *BABAR* fit package, RooFitPackage [46], that uses MINUIT [50] to perform the maximization of the likelihood function numerically. If the likelihood involves several convolutions the maximization is done analytically.

The general philosophy of the time-dependent fits is to obtain τ_B from the Δt event distribution by simultaneously fitting the off-resonance events and the fully reconstructed on-resonance events with the partially reconstructed on-resonance events. The Δt distribution for all the $B\overline{B}$ background types, except $\overline{B} \to D^{**}\rho^+$, is obtained from control samples, Sec. 7.1.7. The fit procedure is described in detail in Sec. 7.1.8.

The probability density function (PDF) for each event type (see Sec. 6.4) per event is the product of probability density functions of four variables: Δt, $m_{\rm miss}$, $m(\rho)$, and $\mathcal{F}$.

The three kinematic variables $\{m_{\rm miss}, m(\rho), \mathcal{F}\}$ are used to distinguish between the various event types. A fifth variable, $m_{\rm ES}$, is used only with fully reconstructed events.

The total likelihood for the partially reconstructed on-resonance event is :

$$\begin{aligned}\mathcal{P}(\vec{x}) &= f_s\,\mathcal{P}_s(\vec{x}) + f_{D^*a_1}\,\mathcal{P}_{D^*a_1}(\vec{x}) \\ &+ f_{{\rm peak}B^0}\,\mathcal{P}_{{\rm peak}B^0}(\vec{x}) + f_{B\overline{B}}\,\mathcal{P}_{B\overline{B}}(\vec{x}) \\ &+ f_{D^{**}}\,\mathcal{P}_{D^{**}}(\vec{x}) + f_{qq}\,\mathcal{P}_{qq}(\vec{x}). \qquad (7.1)\end{aligned}$$

where $\vec{x} \equiv \Delta t, \sigma_{_{\Delta t}}, m_{\rm miss}, m(\rho), \mathcal{F}$ and the fractions f_i are constrained to add up to unity, and the six terms correspond to the six event types as described in Sec. 6.4.

The PDF for the off resonance events is $\mathcal{P}_{qq}(\vec{x})$ of Eq. (7.1). From Monte Carlo we find a small number of events from the various background event types also satisfy the requirements for fully reconstructed signal events as seen from Fig. 7.1. The PDF for the fully reconstructed events is given by :

$$\begin{aligned}\overline{\mathcal{P}}(\vec{y}, m_{_{\rm ES}}) &= \overline{f}_{\,s}\,\mathcal{P}_s(\vec{y})\,G(m_{_{\rm ES}}) \\ &+ \overline{f}_{\,D^*a_1}\,\mathcal{P}_{D^*a_1}(\vec{y})\,A_1(m_{_{\rm ES}})\end{aligned}$$

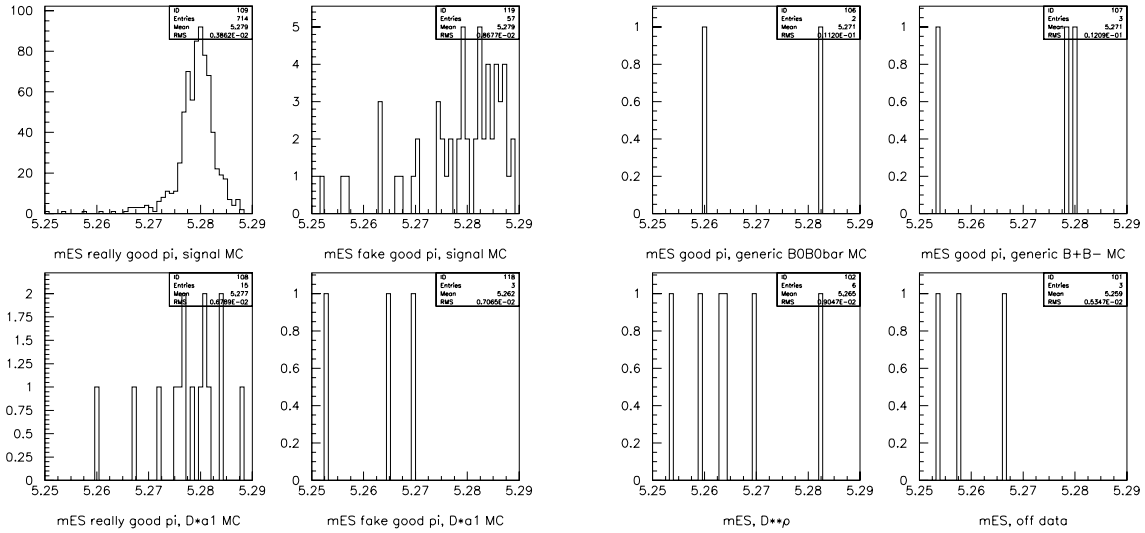

Figure 7.1: The $m_{\rm ES}$ distributions of fully reconstructed events. From left to right, top row: Signal, peaking $B^0\overline{B}^0$, combinatoric $B^0\overline{B}^0$, combinatoric B^+B^-. Bottom row: $B^0 \to D^{*-}a_1^+$, $B^0 \to D^{*-}a_1^+$ reconstructed as peaking $B^0\overline{B}^0$ (see Sec. 6.4), $\overline{B} \to D^{**}\rho^+$, off-resonance data.

$$
\begin{aligned}
&+ \quad \overline{f}_{{\rm peak}B^0}\,\mathcal{P}_{{\rm peak}B^0}(\vec{y})\,A_1(m_{\rm ES}) \\
&+ \quad \overline{f}_{B\overline{B}}\,\mathcal{P}_{B\overline{B}}(\vec{y})\,A_2(m_{\rm ES}) \\
&+ \quad \overline{f}_{D^{**}}\,\mathcal{P}_{D^{**}}(\vec{y})\,A_2(m_{\rm ES}) \\
&+ \quad \overline{f}_{qq}\,\mathcal{P}_{qq}(\vec{y})\,A_2(m_{\rm ES}). \qquad (7.2)
\end{aligned}
$$

where $\vec{y} \equiv \{m_{\rm miss}, m(\rho), \Delta t, \sigma_{\Delta t}\}$, which is the same as $\vec{x}$, but without the Fisher discriminant, $\mathcal{F}$. As seen from Fig. 7.2, both Monte Carlo and data show the distribution of the Fisher discriminant for the fully reconstructed events is different from the Fisher discriminant for which the events were partially reconstructed. The low-

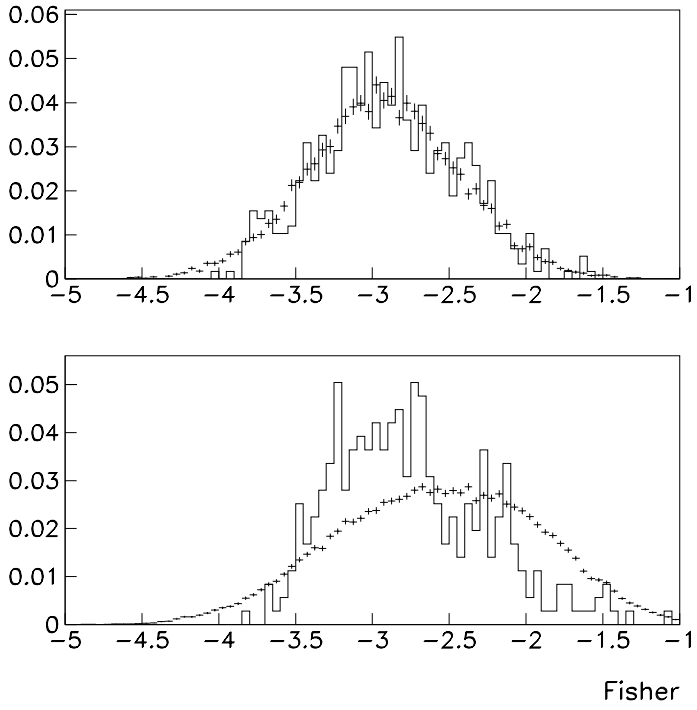

Figure 7.2: A comparison of the normalized distribution of the Fisher discriminant between the partially reconstructed events (error bars) and fully reconstructed events (histogram) in Monte Carlo (top) and data (bottom).

multiplicity of the reconstructed D^0 modes, tend to increase the jetiness of the fully reconstructed event as compared to the partially reconstructed event. For this reason the Fisher discriminant is not used with fully reconstructed events. $G(m_{\rm ES})$ is a Gaussian, and $A_1(m_{\rm ES})$, $A_2(m_{\rm ES})$, are ARGUS functions [51] with two different sets of parameter values. The ARGUS function is defined as

$$A(m_{\rm ES};\epsilon,M_A) \propto m_{\rm ES}\sqrt{1-(m_{\rm ES}/M_A)^2}\ \exp\left[\epsilon\left(1-(m_{\rm ES}/M_A)^2\right)\right]\ \Theta(M_A-m_{\rm ES}). \tag{7.3}$$

where ϵ is the ARGUS exponent, M_A is the end point, and the Θ function ensures that $A(m_{\rm ES}) = 0$ for $m_{\rm ES} > M_A$. This function was first used by the ARGUS collaboration to describe combinatoric $B\bar{B}$ and continuum background. All the fractions $\overline{f}_i$ are obtained from Monte Carlo, except for $\overline{f}_{qq}$ which is obtained from a fit to the fully reconstructed data, Sec. 7.1.4.

The following subsections describe the functional dependence of the different variables of the PDF.

7.1.1. ρ Mass, $m(\rho)$, Distribution

The $m(\rho)$ distribution is fit to a function of the form

$$\mathcal{R}(m(\rho)) = f_B B(m(\rho)) + (1 - f_B) P(m(\rho)). \tag{7.4}$$

where P is a second-order polynomial and

$$B(m(\rho)) \propto \frac{M_\rho^4}{\left(M_\rho^2 - m(\rho)^2\right)^2 + m(\rho)^2 \Gamma(m(\rho))^2}. \tag{7.5}$$

is a relativistic p-wave Breit-Wigner, where

$$\Gamma(m(\rho)) = \frac{M_\rho^2 p_0^3}{m(\rho)^2 p_\pi^3} \Gamma. \tag{7.6}$$

p_π is the momentum of a pion in the ρ rest frame. $p_0 = p_\pi$ when $m(\rho) = M_\rho$. Both P and B are normalized between the $m(\rho)$ fit range of 0.4 GeV/c^2 and 1.1 GeV/c^2.

The parameters, M_ρ and Γ are floating in the fit, and are identical for all the event types as they describe a true ρ meson. However, the parameters of the polynomial (which describes the combinatoric background in the ρ mass window) and the fraction, f_B, are different for each of the event types. They are obtained from the fit to the respective background Monte Carlo for all the background events except continuum. For the continuum events f_B was obtained from the simultaneous fit to the off-resonance data and partially reconstructed on-date. The $m(\rho)$ distribution of Monte Carlo and off-resonance data events is shown in Fig. 7.3 and Fig. 7.4 The $m(\rho)$ PDF parameters obtained from Monte Carlo are summarized in Tables. 7.1 through 7.4. Parameters obtained from data are summarized later, in Tables. 8.1.

7.1.2. Missing Mass, $m_{\rm miss}$, Distributions

The $m_{\rm miss}$ distribution is fit to a function of the form :

$$\mathcal{R}(m_{\rm miss}) = F_{BG}(BG(m_{\rm miss})) + (1 - F_{BG})A(m_{\rm miss}). \tag{7.7}$$

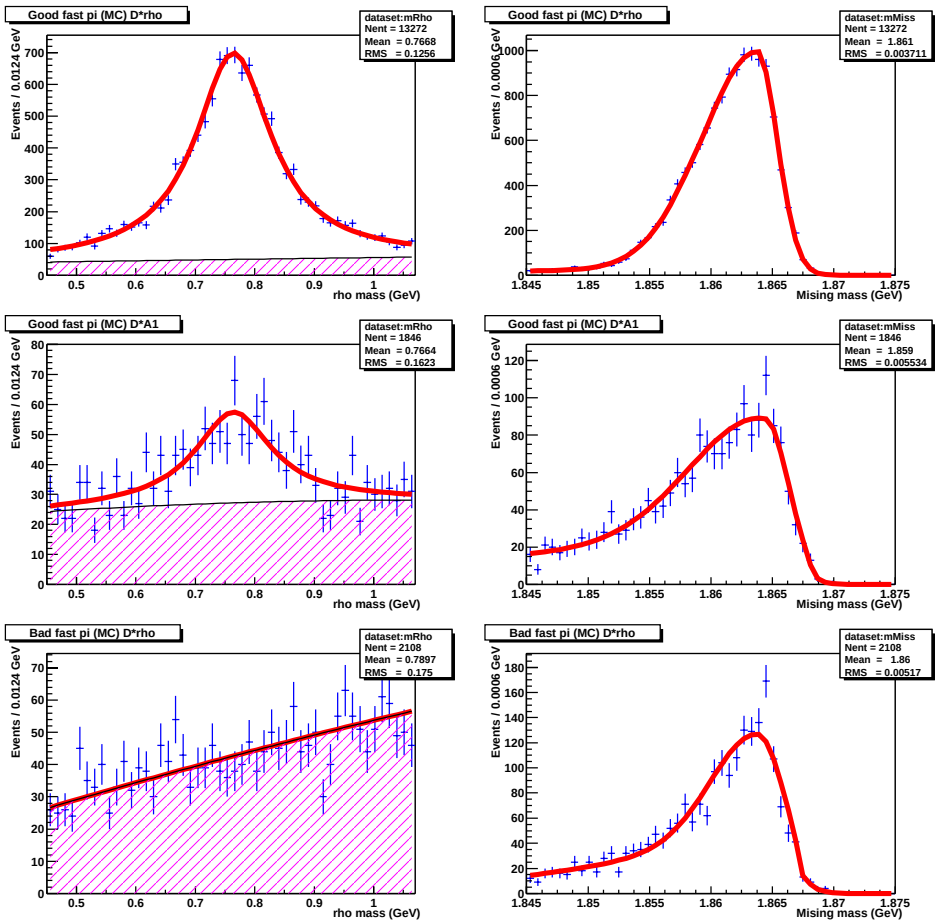

Figure 7.3: $m(\rho)$ and $m_{\rm miss}$ distributions (from top to bottom) of Monte Carlo signal, $B^0 \to D^{*-} a_1^+$, peaking $B^0\overline{B}^0$, The shaded region in the $m(\rho)$ plots shows the polynomial component of the fit.

where $A(m_{\rm miss})$ is an ARGUS function defined in Eq. 7.3, replacing $m_{\rm ES}$ by $m_{\rm miss}$ and $BG(m_{\rm miss})$ is a bifurcated Gaussian :

$$BG(m_{\rm miss}) \propto \begin{cases} \exp\left[-(m_{\rm miss}-\mathcal{M})^2/2\sigma_L^2\right], & m_{\rm miss} < \mathcal{M} \\ \exp\left[-(m_{\rm miss}-\mathcal{M})^2/2\sigma_R^2\right], & m_{\rm miss} > \mathcal{M} \end{cases}. \tag{7.8}$$

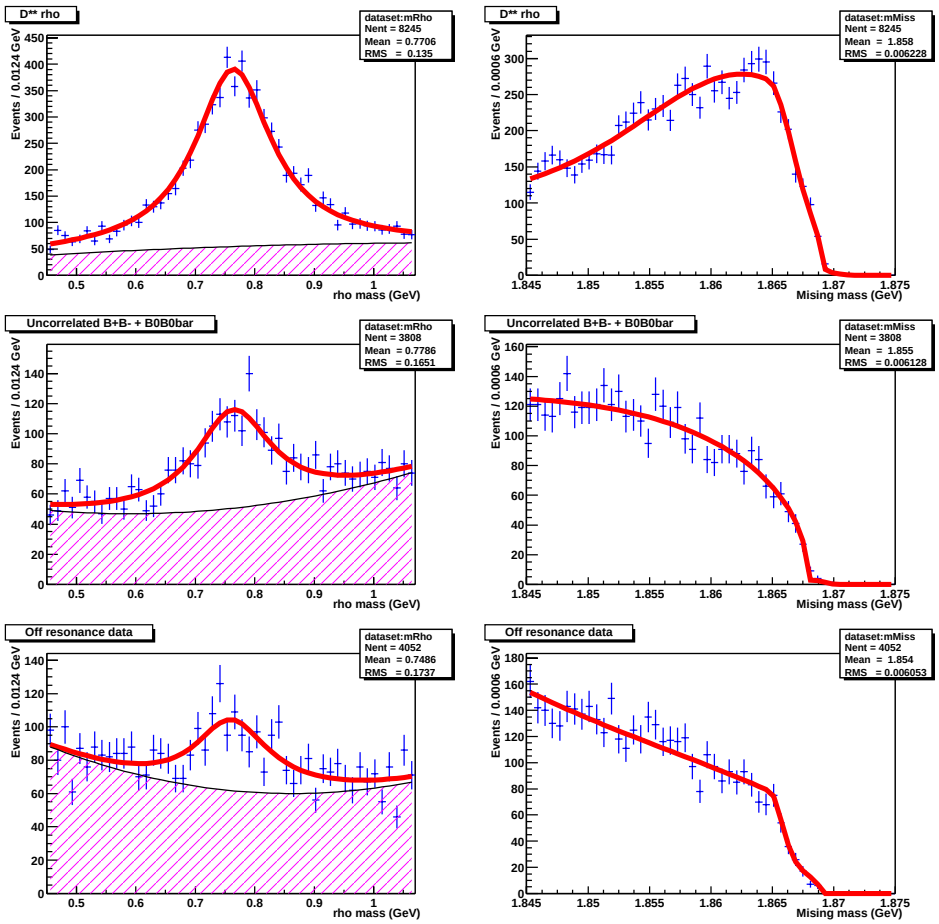

Figure 7.4: $m(\rho)$ and $m_{\rm miss}$ distributions (from top to bottom) of $\overline{B} \to D^{**}\rho^+$ (Monte Carlo), and combinatoric $B\overline{B}$ events (Monte Carlo) , and off-resonance data. The shaded region in the $m(\rho)$ plots shows the polynomial component of the fit.

The $m_{\rm miss}$ distributions of the various event types are shown in Fig. 7.3 and Fig. 7.4. For signal events F_{BG} is equal to one; for misreconstructed signal, $B^0 \to D^{*-}a_1^+$, and $\overline{B} \to D^{**}\rho^+$ events the ARGUS function describes the left-side plateau. Continuum and combinatoric $B\overline{B}$ events are mostly described by the ARGUS function, the bifurcated Gaussian component accounts for the small tail beyond the ARGUS end point. This bifurcated Gaussian typically has σ_R in the order of $1-3$ MeV/c^2 and σ_L greater

than 10 MeV/c^2.

For all the background event types except continuum, the $m_{\rm miss}$ PDF parameters are obtained from Monte Carlo and are summarized in Tables. 7.1 through 7.4. Parameters obtained from data are summarized later, in Table. 8.1.

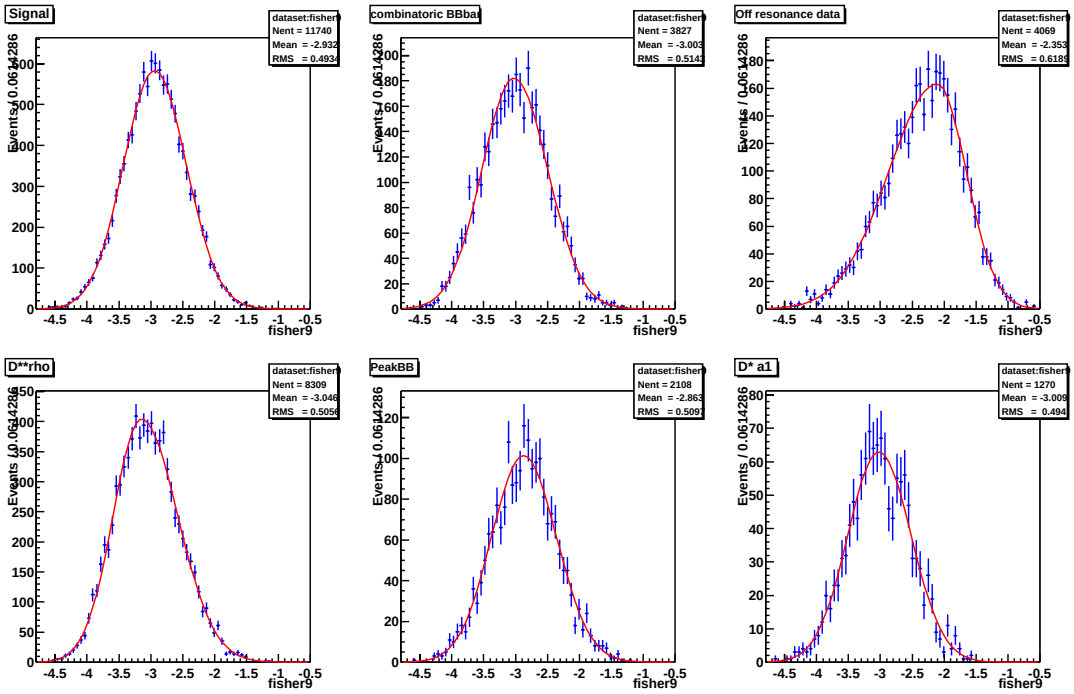

Figure 7.5: Fisher ($\mathcal{F}$) distributions of signal and various background events.

7.1.3. Fisher Discriminant, $\mathcal{F}$ Distributions

The variables used in the construction of the Fisher discriminant, $\mathcal{F}$ are different for each of the different event types, hence the $\mathcal{F}$ distribution is slightly different for each. The $\mathcal{F}$ distribution is parameterized by a bifurcated Gaussian and the parameters are obtained from Monte Carlo for all the $B\overline{B}$ event types. For continuum

Table 7.1: Results of $m_{\rm miss}$ and $m(\rho)$ fits to $B^0 \to D^{*-} a_1^+$ Monte Carlo.

No	Description	Value
$m(\rho)$ polynomial		
1	$m(\rho)$ coefficient	1.31 ± 0.20
2	$(m(\rho))^2$ coefficient	-0.61 ± 0.22
3	Fraction of Breit-Wigner area	0.273 ± 0.029
$m_{\rm miss}$		
4	ARGUS end point	1.86818 ± 0.00008 GeV/c^2
5	ARGUS exponent	-52 ± 26
6	Mean	1.86449 ± 0.00030 GeV/c^2
7	σ_L	0.0060 ± 0.0007 GeV/c^2
8	σ_R	0.00169 ± 0.00015 GeV/c^2
9	Fraction of ARGUS area	0.39 ± 0.12

events the parameters are obtained from a simultaneous fit to the off-resonance and on-resonance data. The $\mathcal{F}$ distributions are shown in Fig. 7.5, and the fit parameters obtained from Monte Carlo are summarized in Table. 7.5.

7.1.4. Energy Substituted Mass, $m_{\rm ES}$, Distributions

The $m_{\rm ES}$ PDFs of the fully reconstructed signal and background events are described by Eq. 7.2. The $m_{\rm ES}$ distributions of signal and background events are shown in Fig. 7.1. A 3-dimensional fit to the fully reconstructed data events is shown in Fig. 7.6.

Table 7.2: Results of $m_{\rm miss}$ and $m(\rho)$ fits to peaking $B^0\overline{B}^0$ background Monte Carlo.

No	Description	Value
$m(\rho)$ polynomial		
1	$m(\rho)$ coefficient	22938.5 ± 1.0
2	$(m(\rho))^2$ coefficient	-3256.3 ± 1.0
3	Fraction of Breit-Wigner area	0
$m_{\rm miss}$		
4	ARGUS end point	1.867230 ± 0.000041 GeV/c^2
5	ARGUS exponent	-100 ± 16
6	Mean	1.86389 ± 0.00024 GeV/c^2
7	σ_L	0.00375 ± 0.00048 GeV/c^2
8	σ_R	0.00190 ± 0.00014 GeV/c^2
9	Fraction of ARGUS area	0.52 ± 0.08

7.1.5. Δt Distributions

In measurements that use the decay length difference technique it is more difficult to disentangle the effects of the lifetime and the detector resolution than in an analysis where both the production point and the decay points are measured like in LEP and SLD experiments. In those experiments, the true proper decay times are described by a simple exponential. There can be no events at negative decay times so the width of negative part of the measured decay time distribution provides valuable information about the detector resolution. The positive part contains the combined effect of both the resolution and the lifetime. For the decay length difference Δt, theory predicts a distribution that is symmetric around zero. The width of the distribution is a result

Table 7.3: Results of $m_{\rm miss}$ and $m(\rho)$ fits to combinatoric $B\overline{B}$ background Monte Carlo.

No	Description	Value
$m(\rho)$ polynomial		
1	$m(\rho)$ coefficient	-1.61 ± 0.43
2	$(m(\rho))^2$ coefficient	1.36 ± 0.20
3	Fraction of Breit-Wigner area	0.287 ± 0.028
$m_{\rm miss}$		
4	ARGUS end point	1.86798 ± 0.00005 GeV/c^2
5	ARGUS exponent	-16.0 ± 2.9
6	Mean	1.8683 ± 0.0007 GeV/c^2
7	σ_L	0.036758 ± 0.13 GeV/c^2
8	σ_R	0.00078 ± 0.00039 GeV/c^2
9	Fraction of ARGUS area	0.972 ± 0.017

of the convolution between the theoretical distribution and detector resolution.

A detailed understanding of the resolution function is crucial for lifetime measurements using the decay length difference technique, and we need to learn as much as possible from data about the resolution function. There exists a strong correlation between the width of the residual and the event-by-event error in the measurement of Δt as seen in Sec. 5.3.2. This means that the resolution function $\mathcal{R}(\Delta t, \sigma_{_{\Delta t}})$, is a function of both the event-by-event error and Δt.

Table 7.4: Results of $m_{\rm miss}$ and $m(\rho)$ fits to $\overline{B} \to D^{**}\rho^+$ Monte Carlo.

No	Description	Value
$m(\rho)$ polynomial		
1	$m(\rho)$ coefficient	33000 ± 11000
2	$(m(\rho))^2$ coefficient	-14000 ± 6000
3	Fraction of Breit-Wigner area	0.679972 ± 0.014
$m_{\rm miss}$		
4	ARGUS end point	1.869290 ± 0.000026 GeV/c^2
5	ARGUS exponent	-29 ± 8
6	Mean	1.86462 ± 0.00023 GeV/c^2
7	σ_L	0.0090 ± 0.0009 GeV/c^2
8	σ_L	0.00189 ± 0.00012 GeV/c^2
9	Fraction of ARGUS area	0.52 ± 0.06

Signal Modeling

The Δt is described by a theoretical distribution $t(\Delta t)$, where $t(\Delta t) \propto exp\frac{-|\Delta t|}{\tau_B}$. To obtain the PDF $\mathcal{T}_s(\Delta t)$ for the reconstructed Δt, we form a convolution of the theoretical distribution $t(\Delta t)$ and the resolution function $\mathcal{R}(\Delta t, \sigma_{\Delta t})$. Thus:

$$\mathcal{T}_s(\Delta t) = \int_{-\infty}^{\infty} t(\Delta t - \bar{\Delta} t) \cdot \mathcal{R}(\bar{\Delta} t, \sigma_{\Delta t})\, d(\bar{\Delta} t). \tag{7.9}$$

There is no *a priori* reason for choosing a particular parameterization for the resolution function, hence some functional form is assumed. In this analysis, the resolution function was obtained from the best fit to the Δt pull distribution and is parameter-

Table 7.5: Results of fits to Fisher distributions in Monte Carlo.

No	Description	Value
$B^0 \to D^{*-}\rho^+$		
1	Mean	-2.934 ± 0.010
2	σ_L	0.490 ± 0.007
3	σ_R	0.503 ± 0.007
$B^0 \to D^{*-}a_1^+$		
4	Mean	-3.023 ± 0.036
5	σ_L	0.486 ± 0.023
6	σ_R	0.503 ± 0.023
Peaking $B^0\overline{B}^0$		
7	Mean	-2.876 $\pm$ 0.028
8	σ_L	0.502 ± 0.018
9	σ_R	0.518 ± 0.018
Combinatoric $B\overline{B}$		
10	Mean	-3.135 ± 0.029
11	σ_L	0.495301 ± 0.015
12	σ_R	0.620 ± 0.035

ized by a sum of three Gaussians.

The lifetime PDF for $B^0 \to D^{*-}\rho^+$ and $B^0 \to D^{*-}a_1^+$ events is:

$$\begin{aligned} \mathcal{T}_s(\Delta t, \sigma_{\Delta t}) &= \left[f_n\, G_n(\Delta t, \sigma_{\Delta t}) + (1 - f_n - f_o)\, G_w(\Delta t, \sigma_{\Delta t}) + f_o\, G_o(\Delta t, \sigma_{\Delta t}) \right] \\ &\otimes \frac{1}{\tau_B} e^{-|\Delta t|/\tau_B}. \end{aligned} \tag{7.10}$$

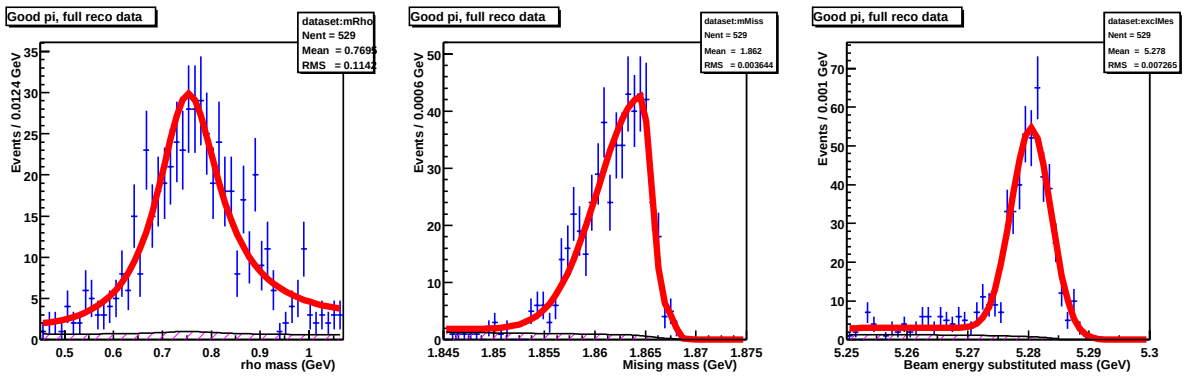

Figure 7.6: A 3-dimensional kinematic fit to fully reconstructed data. The shaded histograms show the continuum contribution. All $m(\rho)$, $m_{\rm miss}$ and $m_{\rm ES}$ parameters of signal events were allowed to float in the fit. $m(\rho)$ and $m_{\rm miss}$ parameters of the backgrounds were fixed from fits to Monte Carlo or off-resonance data. The parameters of the $m_{\rm ES}$ distributions of the backgrounds ($A_1(m_{\rm ES})$ and $A_2(m_{\rm ES})$ of Eq. (7.2)) were also allowed to float. The fractions of all backgrounds, except the continuum background, were fixed by the Monte Carlo yields (Fig. 7.1). The continuum fraction was allowed to float in the fit.

where G_n, G_w, and G_o are the narrow, wide, and outlier Gaussians, of the form

$$G(\Delta t, \sigma_{\Delta t}; b, s) \equiv \frac{1}{\sqrt{2\pi} s\sigma_{\Delta t}} \exp\left(-\frac{(\Delta t - b)^2}{2(s\sigma_{\Delta t})^2}\right). \tag{7.11}$$

Fig. 7.8 shows that this PDF fits well to the pull distribution of signal Monte Carlo events. As the parameters of the resolution function are strongly correlated to τ_B they are left floating while fitting for τ_B in order to avoid the need to extract them from Monte Carlo distribution. However fitting simultaneously for correlated parameters increases the statistical error on all the parameters, hence a trade off between statistical and systematic errors needs to be made. To do so the parameters

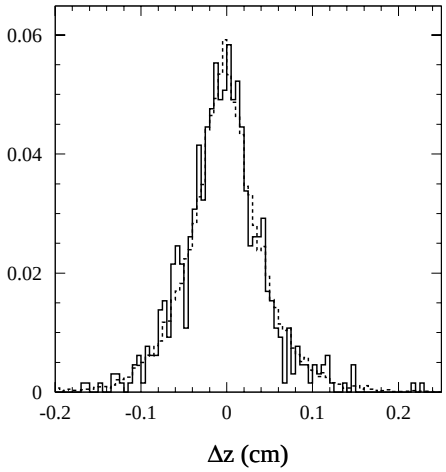

Figure 7.7: The Δz distribution of fully reconstructed signal Monte Carlo events (histogram) and inclusively reconstructed signal Monte Carlo events (dotted line).

of the third Gaussian, G_o are fixed: $b = 0$ ps and $s = 8$ ps; G_o describes the fraction of poorly reconstructed Δt events, such events are called as outlier events. As described in Sec. 10.1.5 the systematic error introduced by fixing the third Gaussians parameters is approximately 1 % of the total systematic error in this analysis.

Background Modeling

The Δt distribution for the backgrounds events need not be necessarily symmetric about zero due to biases from vertex reconstruction for the background events.

The Δt PDF that best describes the combinatoric $B\overline{B}$ background events have the form:

$$\mathcal{T}_b(\Delta t, \sigma_{\Delta t}) = \left[f_n \, G_n(\Delta t, \sigma_{\Delta t}) + (1 - f_n) \, G_w(\Delta t, \sigma_{\Delta t}) \right]$$

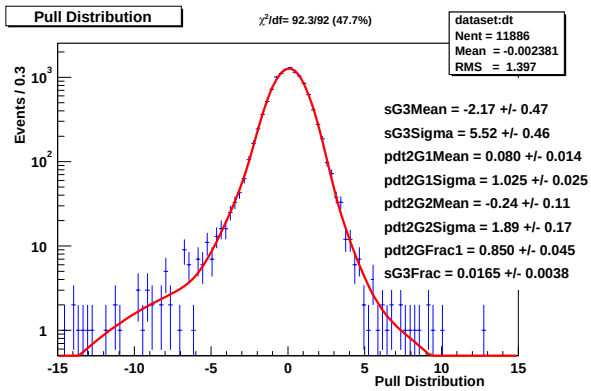

Figure 7.8: Pull distribution of signal Monte Carlo events, using the PDF of Eq. (7.10).

$$\otimes \quad \left[f_\tau \, \frac{1}{\tau} e^{-|\Delta t|/\tau} + (1 - f_\tau)\, \delta(\Delta t) \right]. \tag{7.12}$$

a 2-Gaussian resolution function convoluted with an exponential decay term ("lifetime") plus a prompt decay term (zero lifetime component). The parameter τ is phenomenological in nature, and is in general different from the B^0 lifetime, τ_B.

The PDF of the peaking background have the same functional form, except that it has $f_\tau = 0$, leaving only the prompt decay term. This reflects the fact that this type of background is due to events in which the π_f originates from the other B^0 vertex hence $z_{rec} - z_{other} = 0$

The continuum PDF is functionally the same as Eq. (7.12), plus an outlier term

that does not use per-event errors, thus:

$$\mathcal{T}_{qq}(\Delta t, \sigma_{\Delta t}) = (1 - f_o)\mathcal{T}_b(\Delta t, \sigma_{\Delta t}) + f_o G_o(\Delta t\,; b, s). \tag{7.13}$$

where

$$G_o(\Delta t\,; b, s) \equiv \frac{1}{\sqrt{2\pi}s} \exp\left(-\frac{(\Delta t - b)^2}{2s^2}\right). \tag{7.14}$$

Note that despite the functional similarity, there is no relation between the parameter values used for the PDFs of the different event types.

The PDF of $\overline{B} \to D^{**}\rho^+$ events is that of Eq. (7.12), with the parameter values taken from Monte Carlo and is only used to evaluate systematic errors (see Sec. 10.1.4).

7.1.6. Use of Fully Reconstructed Events

The simultaneous fit of fully reconstructed events with the partially reconstructed events is intended to help the fit extract the signal parameters from a clean signal sample. Therefore, Δt is calculated for fully reconstructed events in exactly the same way as for partially reconstructed events (see Sec. 5.1.3), without using the better knowledge of the B_{rec} decay position offered by full reconstruction.

Fully reconstructed events do their job if their Δt distribution agrees with that of partially reconstructed signal events. This only happens if both event samples have

a similar distributions of the number of $D_{\rm miss}$ daughter tracks assigned to the other B^0 vertex, $N_{\rm tr}^D$,

The distributions of $N_{\rm tr}^D$ in partially and fully reconstructed Monte Carlo for different cone cuts is shown in Fig. 7.9. It can be seen that the high multiplicity in the $K3\pi$ mode results in values of $N_{\rm tr}^D$ which are significantly higher than those observed in the partially reconstructed events while the $K\pi$ and $K\pi\pi^0$ modes agree much better with partially reconstructed events, especially at our selected cone cut of 1 rad, hence the $K3\pi$ mode is not used. From signal Monte Carlo we find that for the Δt distribution the Kolmogorov-Smirnov [52; 53] confidence level of the fully and partially reconstructed events to originate from the same distribution is 75%. The Fig. 7.7 compares the Δz of the fully and partially reconstructed events. Thus partially reconstructed events that are also fully reconstructed in these two D^0 decay modes are expected to have the same Δt distribution and $z_{\rm rec}$ bias as the generic partially reconstructed events, and can be used in the final simultaneous fit. The $K3\pi$ mode is not used. The good agreement between the $N_{\rm tr}^D$ distributions of fully reconstructed data and fully reconstructed signal Monte Carlo, for all cone cuts is shown in Fig. 7.10

Validation of Use of Fully Reconstructed Events

To check for a possible bias that the fully reconstructed events may introduce to the lifetime fit, we compared fits of signal Monte Carlo events, including and

excluding fully reconstructed events for the 5 cone cuts. The average difference in the lifetime between the two cases was 0.001 ps. It is seen that the addition of the fully reconstructed events does not significantly bias the lifetime or the resolution parameters.

7.1.7. $B\overline{B}$ Backgrounds Control Sample Validation

As described in Sec. 7.1.5, it is important that the parameters of the resolution function are obtained from data. If the parameters of the background resolution function do not properly describe the background events, the parameters of the signal resolution function will absorb the discrepancy, and the measured lifetime will be biased. As it is not possible to float the parameters of the signal and the $B\bar{B}$ background resolution function simultaneously due to correlations between the parameters, we need control samples, obtained from data, that can be used to obtain the resolution function parameters of the background. It is important that Δt have the same distribution in both the control sample region and the signal region.

As described in Sec. 7.1.8, the Δt distributions of the combinatoric and peaking $B\bar{B}$ backgrounds are obtained from the $m_{\rm miss}$ sideband region (events which satisfy $1.8 < m_{\rm miss} < 1.84$ GeV/c^2) and the wrong-sign events (where π_s and π_f have the same charge), respectively. Monte Carlo events were used to determine that the control sample distributions agree with the signal region distributions. These distributions

are overlayed in Fig 7.11. The Kolmogorov-Smirnov confidence level for the control sample and signal region Δt to originate from the same distribution is 60% for the combinatoric $B\overline{B}$ and 56% for the peaking $B^0\overline{B}^0$ events.

7.1.8. Fit Procedure

The fits are conducted in several steps:

1. Obtain kinematic parameters from Monte Carlo distributions:

   - The kinematic variable PDF parameters of $B^0 \to D^{*-}a_1^+$, combinatoric $B\overline{B}$ and peaking $B\overline{B}$ are determined by fitting the individual Monte Carlo. See Tables. 7.1 through Table. 7.5.
   - The Fisher PDF parameters of $B^0 \to D^{*-}\rho^+$ are also obtained from Monte Carlo (see Table. 7.5).
   - By counting how many Monte Carlo events of each type pass the cuts, we determine $f_{D^*a_1}$, and $f_{\mathrm{peak}B^0}$ of Eq. (7.1), Table. 7.6.

   Obtain initial values of parameters to be determined later from simultaneous data fits:

   - Initial values of all PDF parameters of continuum events are determined by fitting off-resonance data.

- Initial values of the Δt, $m_{\rm miss}$, $m(\rho)$ and $m_{\rm ES}$ PDF parameters of signal are obtained from the fully reconstructed sample.

2. The combinatoric $B\overline{B}$ Δt distribution is parameterized by fitting the $m_{\rm miss}$ sideband (See Sec. 7.1.7 for the validity of using this control sample). Only two event types populate the sideband: Combinatoric $B\overline{B}$ and continuum. Consequently, we fit in only two variables: Fisher and Δt. The fit is done simultaneously for on- and off-resonance data, in 2 steps:

   - Kinematic fit: We float the Fisher PDF parameters of the continuum and the fraction of $B\overline{B}$ events. All other fractions are fixed at 0.
   - Float the Δt PDF parameters of the combinatoric $B\overline{B}$ and the continuum, everything else is fixed. The fraction of non-prompt continuum events is fixed at 0.

3. The peaking $B^0\overline{B}^0$ Δt distribution is parameterized by fitting the wrong-sign events in the normal $m_{\rm miss}$ range (referred to as the signal region). The only event types populating this sample are continuum, combinatoric $B\overline{B}$ and peaking $B^0\overline{B}^0$. The on-resonance and off-resonance data samples are fit simultaneously. This fit is again done in two steps:

   - Kinematic fit: We float the Fisher, $m(\rho)$ and $m_{\rm miss}$ PDF parameters of the continuum, as well as the fractions of combinatoric $B\overline{B}$ and continuum

events. Floating the continuum kinematic parameters improves their determination, which would otherwise be done using only the low-statistics off-resonance data sample.

- The Δt PDF parameters of the peaking $B^0\overline{B}^0$ and the continuum are allowed to float, everything else is fixed. The combinatoric $B\overline{B}$ Δt PDF parameters are taken from the sideband fit. The fraction of non-prompt continuum events is fixed at 0.

4. Fit to right-sign signal-region on-resonance data, simultaneously with off-resonance data and fully reconstructed data, done again in two steps:

   - Kinematic fit: We float the $m_{\rm miss}$, $m(\rho)$ and $m_{\rm ES}$ PDF parameters of signal events, the kinematic variable PDF parameters of continuum, and the fractions of combinatoric $B\overline{B}$ and continuum events. The fraction of $\overline{B} \to D^{**}\rho^+$ events is initially set to 0. All other fractions are determined in step 1.

   - The Δt PDF parameters of continuum and signal float. To improve stability, we fix the values of the mean and width of the continuum outlier, and the mean and the width of the signal outlier. They are later varied to evaluate systematic errors (Sec. 10.1.5).

Table 7.6: Fractions of events obtained by counting the number of events, N, in Monte Carlo and then used in the fit. See Eq. (7.1) for parameter definitions, and Secs. 10.1.4, 10.1.6, and 10.1.7 for systematic error variation in these parameters.

No	Description	Value
1	$f_{D^{**}} = N_{D^{**}}/(N_{D^{**}} + N_{B\overline{B}})$	0
2	$f_{D^*a_1} = N_{D^*a_1}/(N_{D^*a_1} + N_{D^*\rho})$	0.116
3	$f_{\mathrm{peak}B^0} = N_{\mathrm{peak}B^0}/(N_{\mathrm{peak}B^0} + N_{D^*a_1} + N_{D^*\rho})$	0.0965

7.1.9. Monte Carlo Validation of the Δt Fit Procedure

The entire fit procedure described in Sec. 7.1.8 was carried out on Monte Carlo data. In order to obtain a more realistic fraction of continuum events in the Monte Carlo sample, off-resonance data events were used alongside continuum Monte Carlo. One eighth of the continuum sample obtained this way was labeled as "off-resonance" for the purpose of conducting the fit, and seven eighths were added to the $B\overline{B}$ Monte Carlo to serve as the continuum component of the "on-resonance" sample. $\overline{B} \to D^{**}\rho^+$ events were excluded from the "on-resonance" sample (See Sec. 10.1.4).

Projections of the PDF onto the 4 fit variables are shown in Fig. 7.12. The fit results are shown in Table. 7.7. The value of τ_B obtained is in good agreement with the generated value of 1.548 ps, as well as the Monte Carlo truth fit value of 1.534 ps (Sec. 8.1.3). The other fit parameters appear reasonable as well. The large statistical errors reflect the low Monte Carlo statistics.

It may be worthwhile to note that doing the kinematic fit on data would take

anywhere between one to two CPU hours to obtain a convergent fit and between two and four hours to do the lifetime fit. The fit sometimes would not converge due to local minima that would cause MINUIT to crash and the fit had to be restarted with slightly different parameters and/or constraints.

Table 7.7: Results of the fit to the validation sample containing signal and background events. The value of $\tau_{_B}$ obtained in the fit is $0.51\,\sigma$ away from the Monte Carlo truth value of 1.534 ps (Sec. 8.1.3). See Eqs. (7.10-7.11).

Parameter	Fit value
b of G_o	9.4 ± 3.5 ps
s of G_o	6.3 ± 5.1
f_o	0.0002 ± 0.0012
b of G_n	-0.31 ± 0.10 ps
s of G_n	0.888 ± 0.081
f_n	0.874 ± 0.039
b of G_w	-0.18 ± 0.73 ps
s of G_w	3.79 ± 0.63
$\tau_{_B}$	1.48 ± 0.11 ps

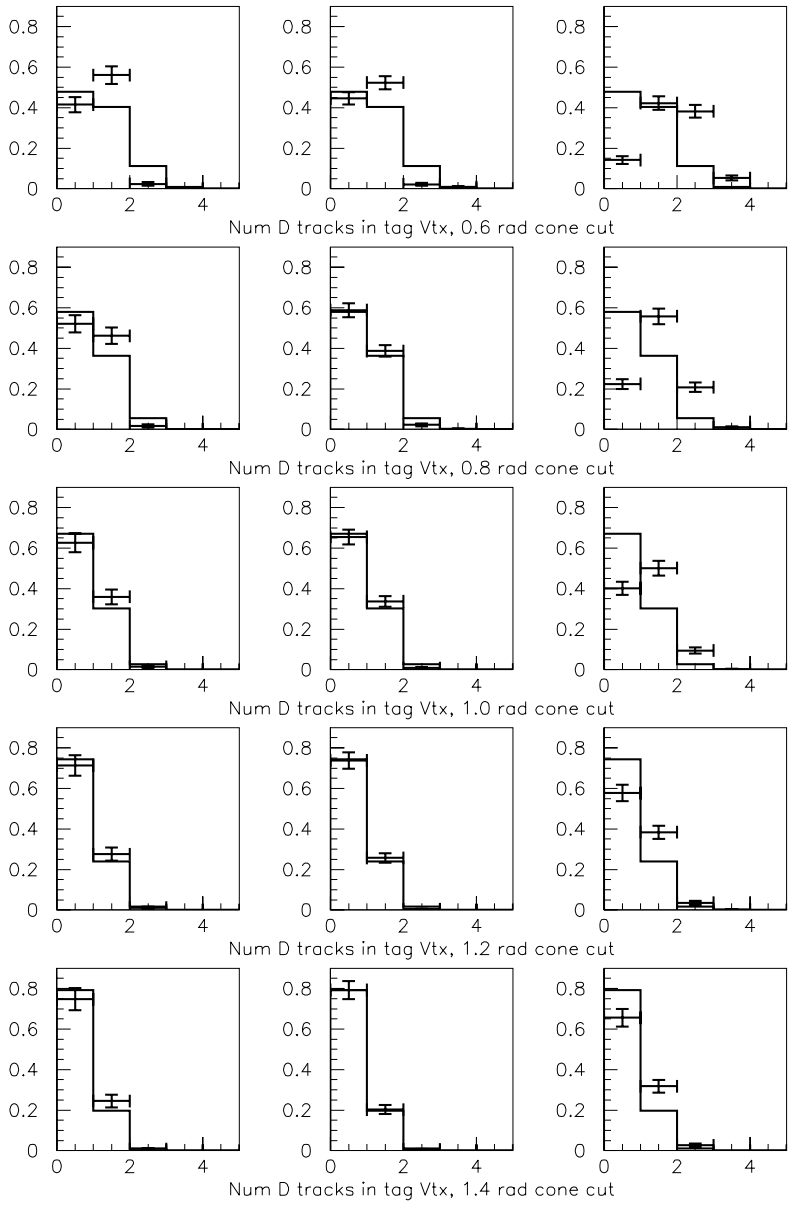

Figure 7.9: The number of $D_{\rm miss}$ daughter tracks wrongly assigned to the B_{other} vertex for cone cuts of (from top to bottom) 0.6, 0.8, 1.0, 1.2, and 1.4 rad. The histograms are from partially reconstructed Monte Carlo events. The data points are from fully reconstructed Monte Carlo in the modes (from left to right) $K\pi$, $K\pi\pi^0$, and $K3\pi$. All distributions are normalized to unit area.

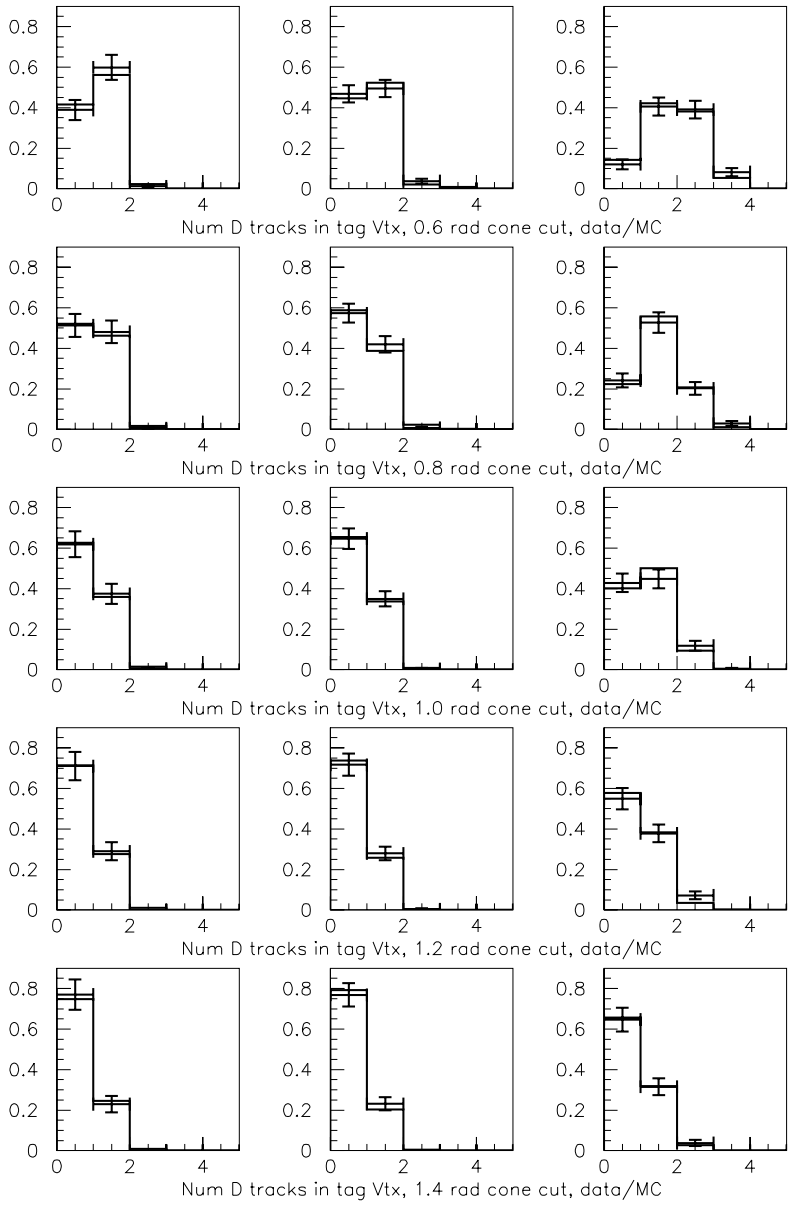

Figure 7.10: The number of $D_{\rm miss}$ daughter tracks wrongly assigned to the tag B vertex for cone cuts of (from top to bottom) 0.6, 0.8, 1.0, 1.2, and 1.4 rad. The histograms are fully reconstructed Monte Carlo events, and the data points are from fully reconstructed data in the modes (from left to right) $K\pi$, $K\pi\pi^0$, and $K3\pi$. All distributions are normalized to unit area.

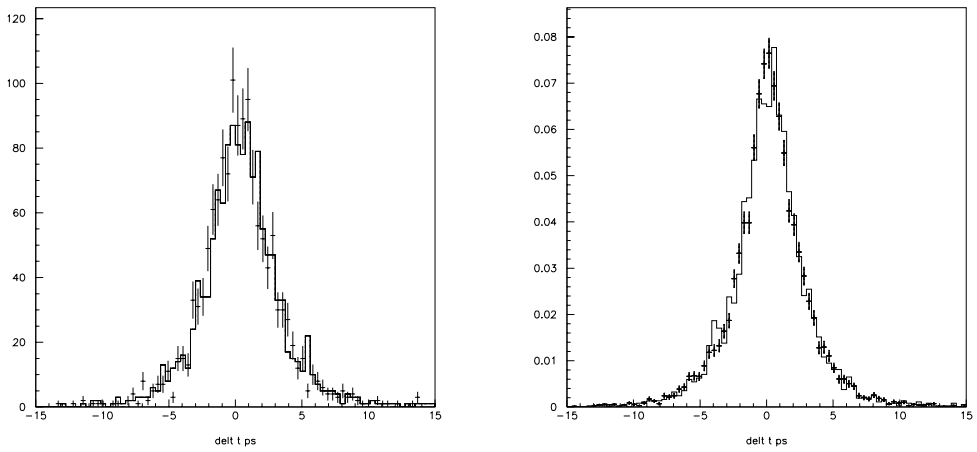

Figure 7.11: Left: The Δt distribution of peaking background Monte Carlo for right-sign (histogram) and wrong-sign (data points) events. Right: The Δt distribution of the combinatoric background Monte Carlo for sideband (data points) and signal region (histogram) events.

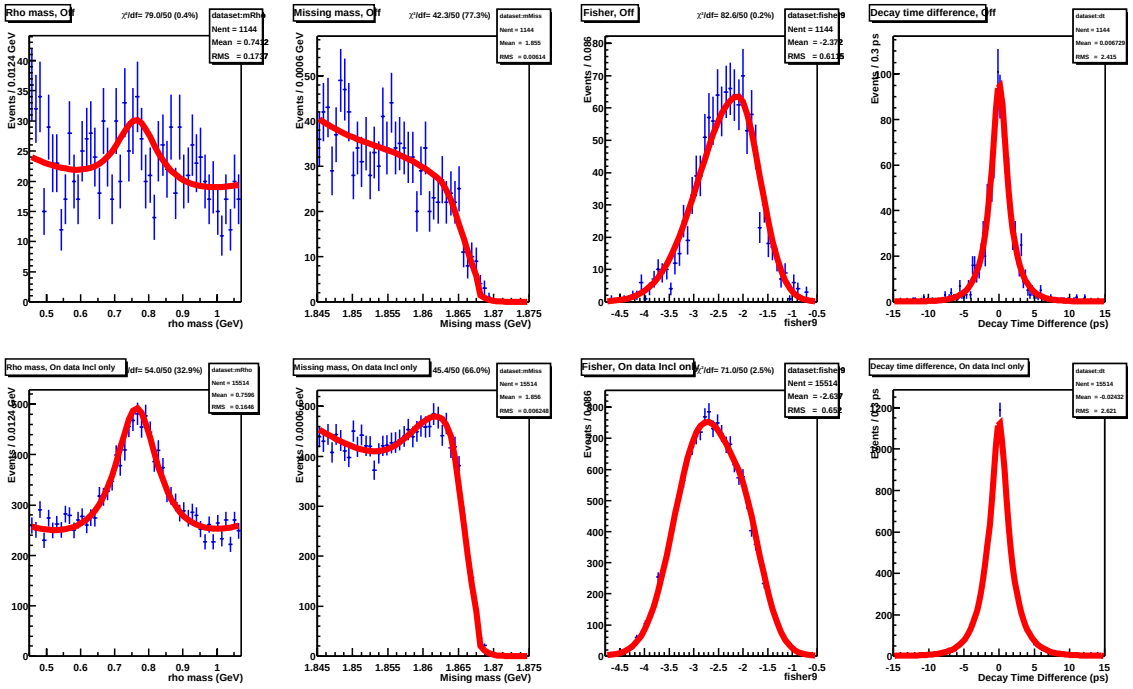

Figure 7.12: Projections of the PDF onto the right-sign Monte Carlo "off-resonance" sample (top) and "on-resonance" sample (bottom). The variables, from left to right, are $m(\rho)$, $m_{\rm miss}$, $\mathcal{F}$, and Δt.

Chapter 8

B^0 Lifetime Result

8.1. The Uncorrected Lifetime

The results of the kinematic fit are reported in Table. 8.1 and Table. 8.2, and projections of the PDFs onto the data are shown in Fig. 8.1. The numbers of events of the different types found in the on-resonance data sample are listed in Table. 8.3.

A branching ratio estimate can be made using the number of events, 7400 ± 171 without cuts on Δt or $\sigma_{\Delta t}$, the reconstruction efficiency is 0.0435 ± 0.009 and the total number of B^0, 22×10^6, corresponding to the integrated luminosity. This leads to

$$BR(B^0 \to D^{*-}\rho^+) \approx \frac{\text{No. of } B^0 \text{ decay to } B^0 \to D^{*-}\rho^+}{\text{efficiency}} / \text{total no. of } B^0, \qquad (8.1)$$

which is approximately $(0.78 \pm 0.014)\%$, where the error is only statistical. This number compares well to the PDG [55] value of $(0.73 \pm 0.15)\%$, the error is a combination

of statistical and systematic. Thus the kinematic fit does its job in identifying signal events. The results of the fit to the sideband data is shown in Table. 8.4 and Fig. 8.2. Projections of the kinematic fit to the wrong-sign data are shown in Fig. 8.3. Fig. 8.4 and Table. 8.5 show the results of the wrong-sign data Δt fit. Finally, the results of the Δt fit to the signal region data are shown in Fig. 8.5 and Fig. 8.6 and summarized in Table. 8.6.

By varying $\tau_{_B}$ from the fitted value we look at the change in the negative log likelihood. This was done to check whether the fitted value is at the true minima and they were no secondary minima in the distribution. From this scan of the negative log likelihood as a function of $\tau_{_B}$ it is seen that the fitted value is indeed at the true minima as shown in Fig. 8.7.

The uncorrected value of the lifetime obtained from the fit is

$$\tau_{_B}^{\rm raw} = 1.535 \pm 0.064(\text{stat})\,\text{ps}. \tag{8.2}$$

Studies done in Monte Carlo data show that the partial reconstruction procedure and the fit procedure have biases and hence the fitted $\tau_{_B}$ has to be corrected to take into account these biases. One may note that the corrections due to the biases are consistent with zero at a two sigma level. Thus it is conservative to add these biases to the final result. In the following section we shall describe these biases.

8.1.1. $B^0 \to D^{*-} a_1^+$ Bias

We assign the same Δt parameters, including $\tau_{_B}$, to both the $B^0 \to D^{*-}\rho^+$ and $B^0 \to D^{*-}a_1^+$ events in our data sample. Since the a_1^+ and $D_{\rm miss}$ are almost back-to-back, the cone cut is not effective in preventing the a_1^+ daughter tracks being assigned to the other B^0 vertex as shown in Fig. 8.8. As a result, the $B^0 \to D^{*-}a_1^+$ events reduce the value of the measured $\tau_{_B}$.

Fitting Monte Carlo events for signal plus $B^0 \to D^{*-}a_1^+$ yields a measured lifetime which is $\Delta t_{a_1}^{\rm bias} = 0.008 \pm 0.011$ ps smaller than the lifetime obtained with only signal events. The error is due to Monte Carlo statistics. We therefore correct the lifetime measured on data by adding 0.008 ps to it, with a systematic error of 0.011 ps.

8.1.2. D^0 Bias

The cone cut as described in Sec. 5.2.2 is not 100 % effective at removing all the D^0 tracks. These tracks have, on average the effect of reducing Δz to smaller values thereby biasing the lifetime $\tau_{_B}$ to smaller values compared to the true value. It is observed from Monte Carlo that a fit to the true Δt yields a value of 1.534 ps (Sec. 8.1.3) for the B^0 lifetime, while the fit to the reconstructed Δt yields 1.506 ± 0.033 ps. Thus in Monte Carlo the fitted lifetime should be corrected by a factor of $R_{D^0} = 0.982 \pm 0.022$. We assume the same correction factor for data with a systematic error of 0.036 ps due to Monte Carlo statistics.

8.1.3. Selection Bias

Our event selection cuts may bias the sample toward events that have a non-average lifetime. Fitting the true lifetime of our selected signal events to an exponential PDF convoluted with a Gaussian (to account for B^0 motion in the CM frame), we obtain a lifetime of 1.534 ± 0.013 ps. Since the Monte Carlo is generated with the value 1.548 ps, we apply a +0.014 ps correction to our final result, with a systematic error of 0.013 ps.

There is an additional bias due to the likelihood fit discussed in Sec. 9.1.2 of 0.031 ± 0.016 ps

8.1.4. Bias Correction Summary

Table. 8.7 provides the summary of the change in the B^0 lifetime after each bias correction.

The bias corrected B^0 lifetime is calculated as follows:

$$\tau_{_B} = \frac{\tau_{_B}(a_1) + \tau_{_B}(D^0)}{R_{D^0}} + \tau_{_B}(\text{SB}) + \tau_{_B}(\text{fit})\,\text{ps}. \tag{8.3}$$

The B^0 lifetime after correcting for all the biases is

$$\tau_{_B} = 1.616 \pm 0.064(\text{stat})\,\text{ps}. \tag{8.4}$$

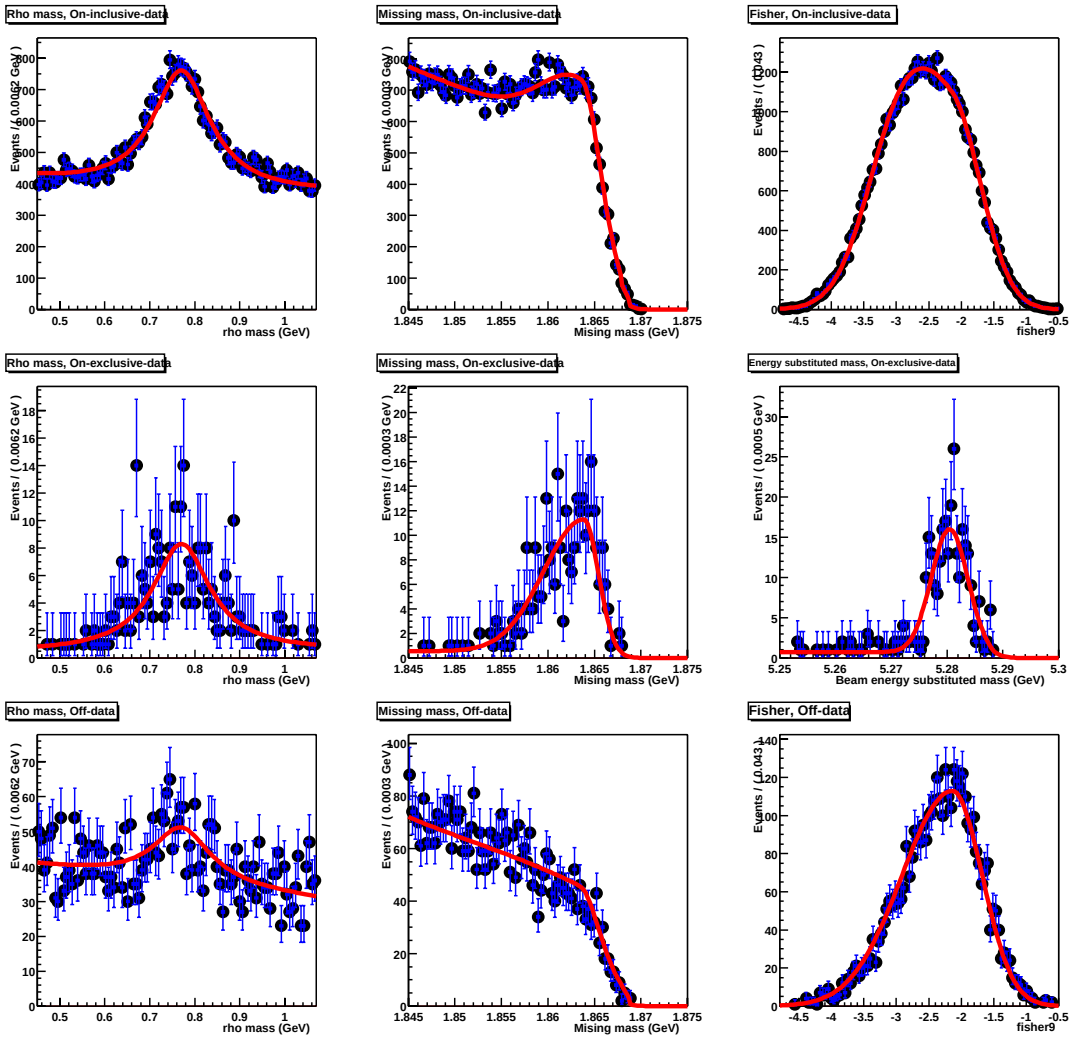

Figure 8.1: Projections of the kinematic variable PDF on the partially reconstructed on-resonance data (top), fully reconstructed on-resonance data (middle), and off-resonance data (bottom). All events are right-sign, signal region. The variables are, from left to right, $m(\rho)$, $m_{\rm miss}$, and Fisher (for partially reconstructed and off-resonance data), or $m(\rho)$, $m_{\rm miss}$, and $m_{\rm ES}$ (for fully reconstructed data).

Table 8.1: Results of the kinematic fit to data.

No	Description	Value
$m(\rho)$ parameters of true ρ^+		
1	Mean	0.7703 ± 0.0014 GeV/c^2
2	Width	0.1556 ± 0.0038 GeV
$B^0 \to D^{*-}\rho^+$ $m(\rho)$ polynomial		
3	$m(\rho)$ coefficient	1.1 ± 1.0
4	$(m(\rho))^2$ coefficient	0.5 ± 1.0
5	Fraction of Breit-Wigner area	1.00000 ± 0.00012
$B^0 \to D^{*-}\rho^+$ $m_{\rm miss}$		
6	ARGUS end point	1.8779 ± 0.0030 GeV/c^2
7	ARGUS exponent	-75 ± 83
8	Mean	1.86388 ± 0.00017 GeV/c^2
9	σ_L	0.00433 ± 0.00017 GeV/c^2
10	σ_R	0.00154 ± 0.00012 GeV/c^2
11	Fraction of ARGUS area	$8 \times 10^{-9} \pm 4 \times 10^{-6}$
Continuum $m(\rho)$ polynomial		
12	$m(\rho)$ coefficient	$-0.335 \pm .020$
13	$(m(\rho))^2$ coefficient	0.002 ± 0.015
14	Fraction of Breit-Wigner area	0.131 ± 0.008
Continuum $m_{\rm miss}$		
15	ARGUS end point	1.868820 ± 0.000021 GeV/c^2
16	ARGUS exponent	24.259 ± 0.040
17	Mean	1.86343 ± 0.00018 GeV/c^2
18	σ_L	0.0200 ± 0.0029 GeV/c^2
19	σ_R	0.00197 ± 0.00010 GeV/c^2
20	Fraction of ARGUS area	0.543 ± 0.033
Continuum Fisher		
21	Mean	-2.120 ± 0.010
22	σ_L	0.772 ± 0.007
23	σ_R	0.453 ± 0.005

Table 8.2: Fraction of events from Eq. 7.1.

24	$f_{B\overline{B}}/(f_{B\overline{B}} + f_{\mathrm{peak}B^0} + f_{D^*a_1} + f_s)$	0.616 ± 0.017
25	f_{qq}	0.660 ± 0.009

Table 8.3: Numbers of signal and background events found in the on-resonance data sample, as determined by the kinematic fit. The first error is statistical, reflecting only the statistical error in the fractions reported in Table. 8.1. All other fractions were fixed. Their variation is discussed in Secs. 10.1.4, 10.1.6, and 10.1.7. The second error is systematic, due only to the statistics in the Monte Carlo samples used to obtain the parameters reported in Table. 7.1 through 7.6, and evaluated using the method of Sec. 10.1.1.

Event type	Number of events
$B^0 \to D^{*-}\rho^+$	$5266 \pm 251 \pm 34$
$B^0 \to D^{*-}a_1^+$	$691 \pm 36 \pm 4$
Peaking $B^0\overline{B}^0$	$636 \pm 43 \pm 4$
Combinatoric $B\overline{B}$	$10034 \pm 392 \pm 310$
$\overline{B} \to D^{**}\rho^+$	0
Continuum	$34271 \pm 441 \pm 347$

Table 8.4: Results of the Δt fit to the sideband data. See Eqs. (7.11-7.12).

No	Description	Value
1	Lifetime of combinatoric $B\overline{B}$ events	1.389 ± 0.028 ps
2	b of G_n	-0.27 ± 0.06 ps
3	s of G_n	0.61 ± 0.05
4	f_n	0.68 ± 0.05
5	b of G_w	0.25 ± 0.13 ps
6	s of G_w	1.65 ± 0.10
7	f_τ	1.000 ± 0.011

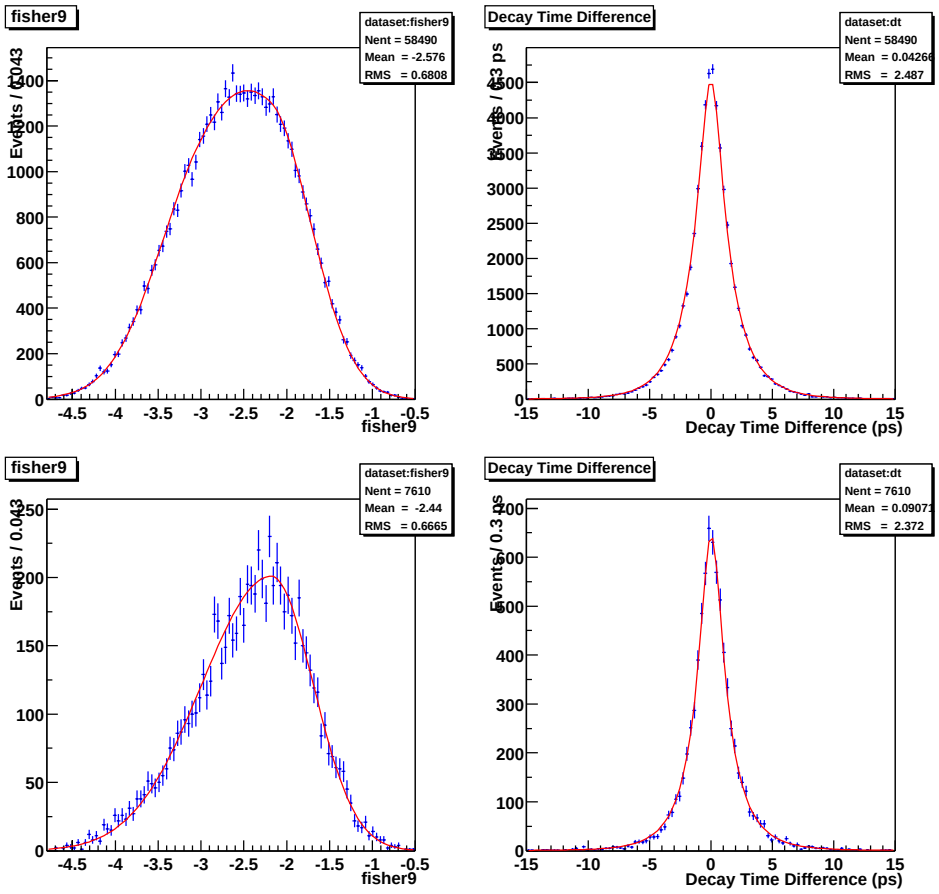

Figure 8.2: Projections of the sideband PDF on the on-resonance (top) and off-resonance (bottom) sideband data. The variables shown are the Fisher (left) and Δt (right).

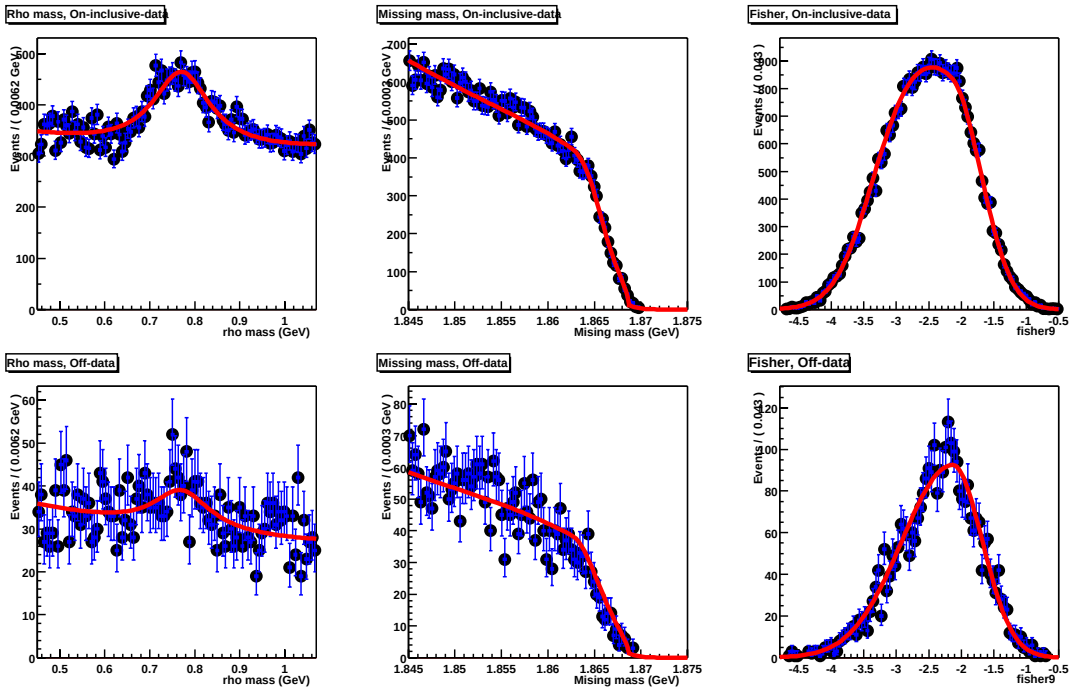

Figure 8.3: Projections of the wrong-sign kinematic variable PDF on the wrong-sign on-resonance (top) and off-resonance (bottom) data. The variables are, from left to right, $m(\rho)$, $m_{\rm miss}$, and the Fisher discriminant.

Table 8.5: Results of the Δt fit to the wrong-sign data. See Eqs. (7.11-7.12).

No	Description	Value
1	b of G_n	1.81 ± 0.23 ps
2	s of G_n	0.96 ± 0.16
3	f_n	0.61 ± 0.07
4	b of G_w	-1.5 ± 1.8 ps
5	s of G_w	11.3 ± 2.7

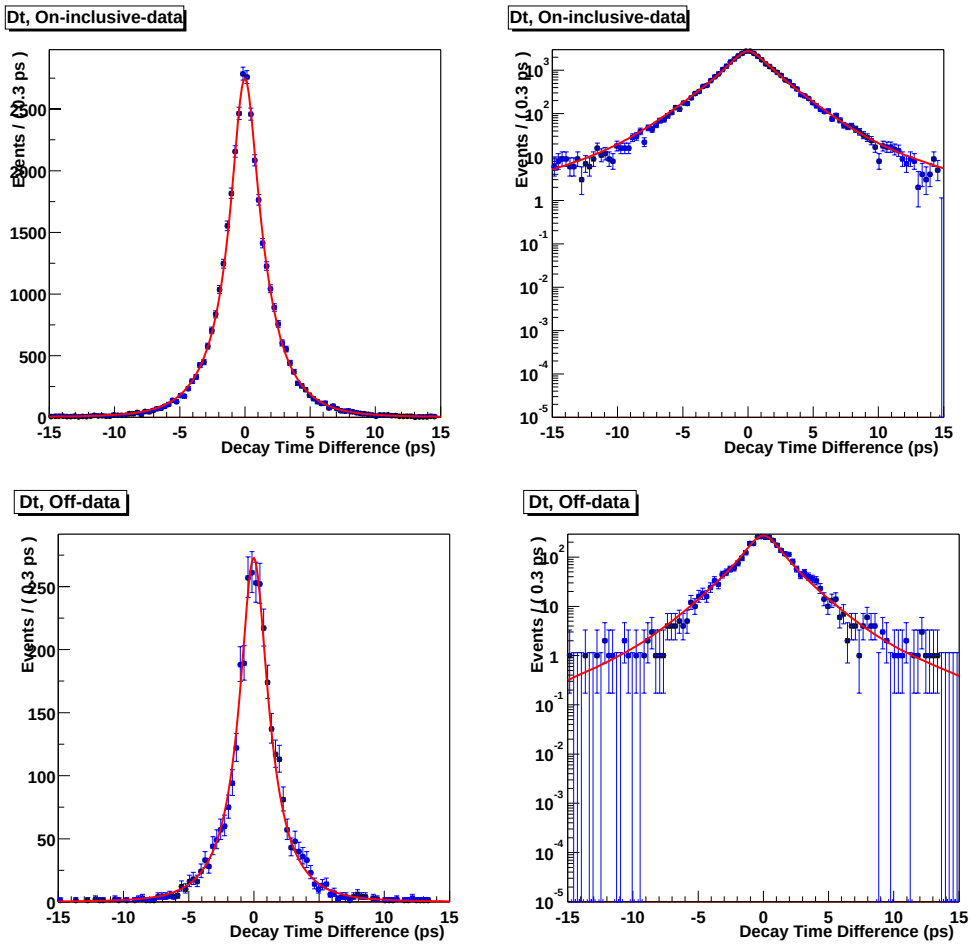

Figure 8.4: Projections of the wrong-sign Δt PDF on the wrong-sign on-resonance (top) and off-resonance (bottom) data. Both linear and log scales are shown.

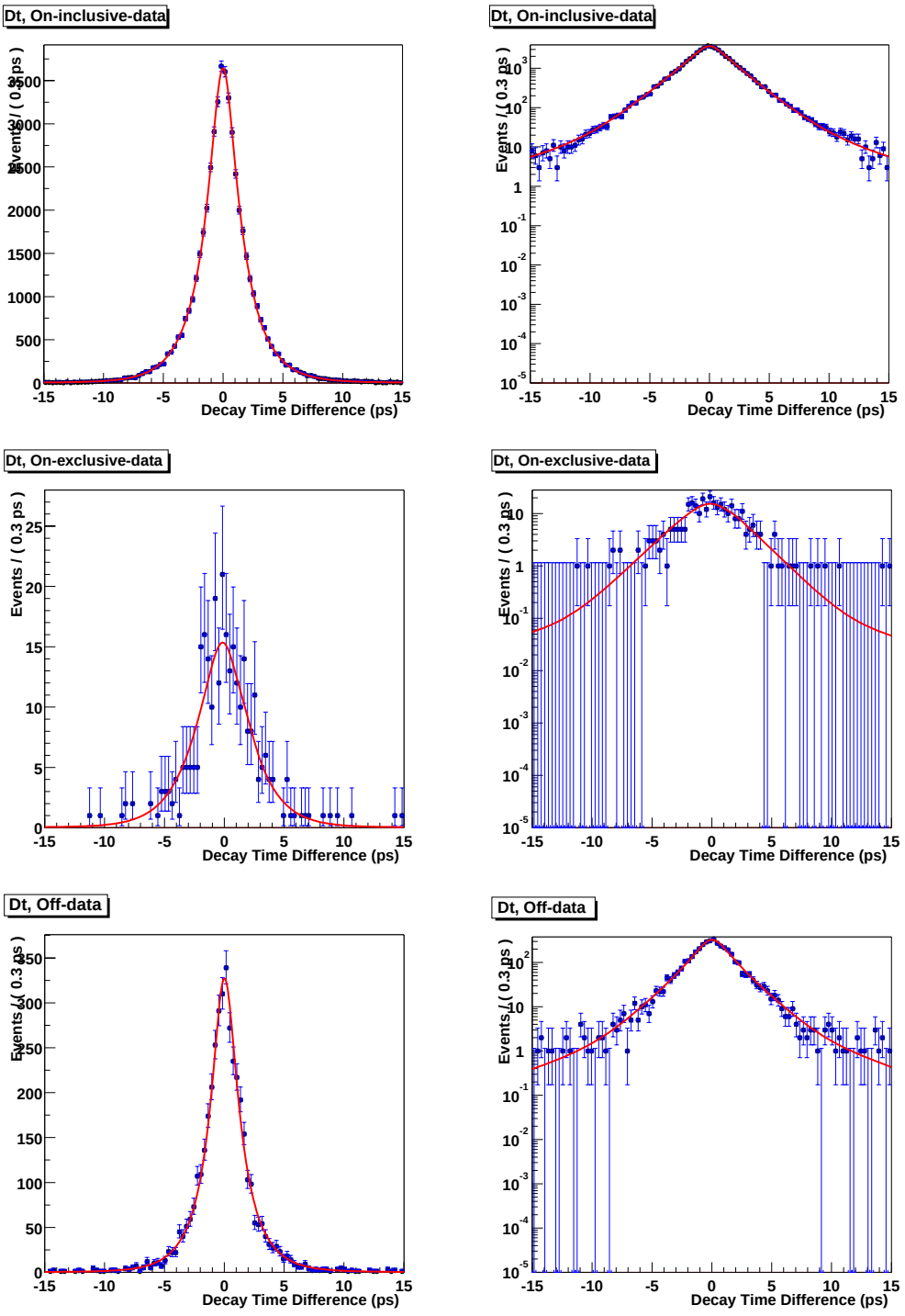

Figure 8.5: Projections of the Δt PDF on the partially reconstructed on-resonance data (top), fully reconstructed on-resonance data (middle), and off-resonance data (bottom). Both linear scale and log plots are shown. All events are right-sign, signal region.

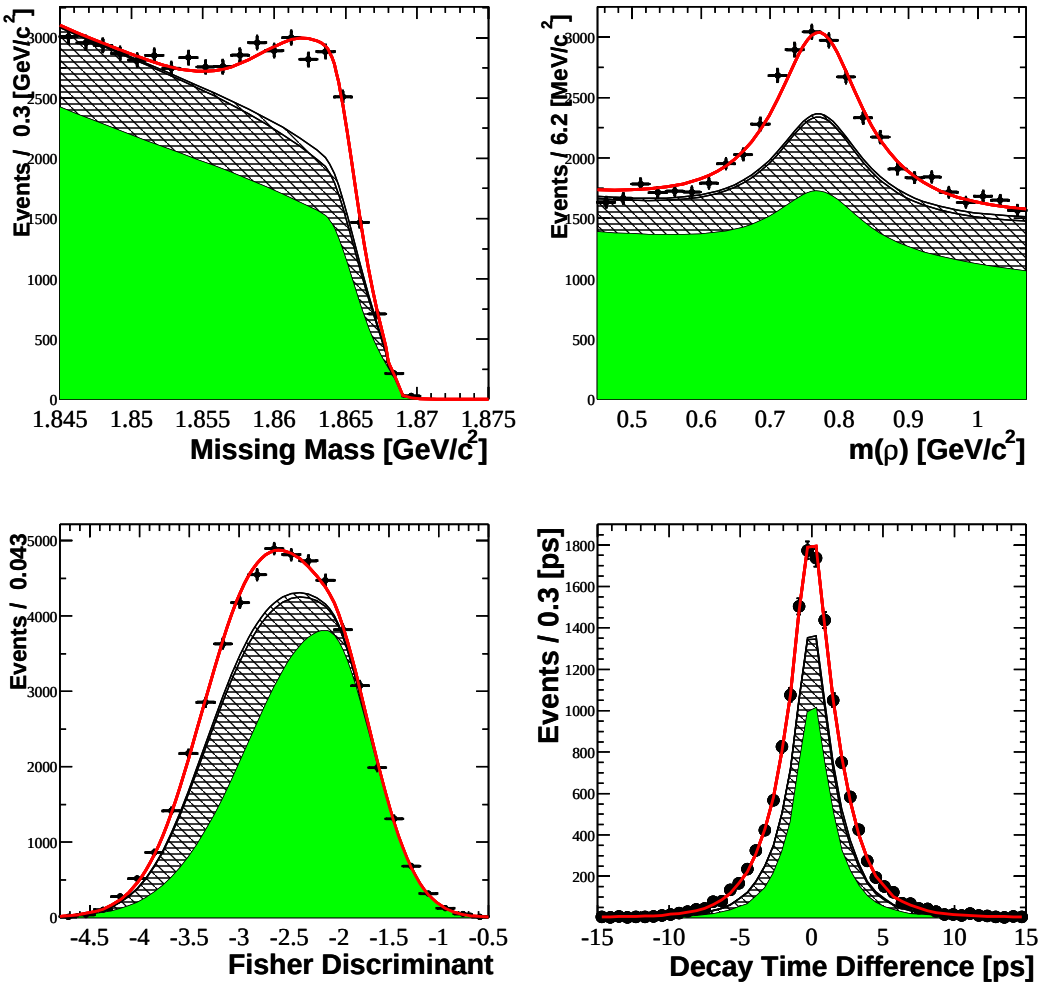

Figure 8.6: The missing mass, ρ mass, Fisher distribution and the Δt distribution for the on-resonance right sign events. The result of the fit is superimposed on data. The hatched, cross-hatched and shaded areas are the peaking $B\bar{B}$, combinatoric $B\bar{B}$ and continuum events respectively.

Table 8.6: Results of the Δt fit to the right-sign signal-region data. See Eqs. (7.10-7.13).

No	Description	Value
$B^0 \to D^{*-}\rho^+$ (and $B^0 \to D^{*-}a_1^+$ parameters)		
1	τ_B	1.535 ± 0.064 ps
2	b of G_n	-0.239 ± 0.005 ps
3	s of G_n	1.0380 ± 0.0042
4	f_n	0.9681 ± 0.0013
5	b of G_w	-0.29 ± 0.18 ps
6	s of G_w	4.50 ± 0.13
7	f_o	$2 \times 10^{-10} \pm 8 \times 10^{-6}$
Continuum parameters		
8	Lifetime of continuum events	0.78000 ± 0.00002 ps
9	b of G_n	0.0163 ± 0.0009 ps
10	s of G_n	1.0349 ± 0.0007
11	f_n	0.9038 ± 0.0005
12	b of G_w	0.346 ± 0.010 ps
13	s of G_w	2.440 ± 0.007
14	f_o	0.01046 ± 0.00014
15	f_τ	0.2125 ± 0.0020

Table 8.7: The change in τ_B due to each bias correction.

Description	$\Delta\tau_B$ Value (ps)
D^0 correction	0.008 ± 0.011
R_{D^0} correction	0.028 ± 0.036
Selection bias	0.014 ± 0.013
Fit Bias	0.031 ± 0.016

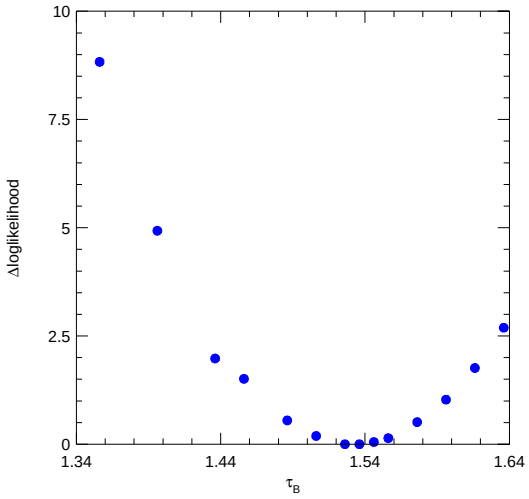

Figure 8.7: Scan of the negative log likelihood obtained from the data, as a function of $\tau_B^{\rm raw}$. The minima is at the fitted value of 1.535 ps.

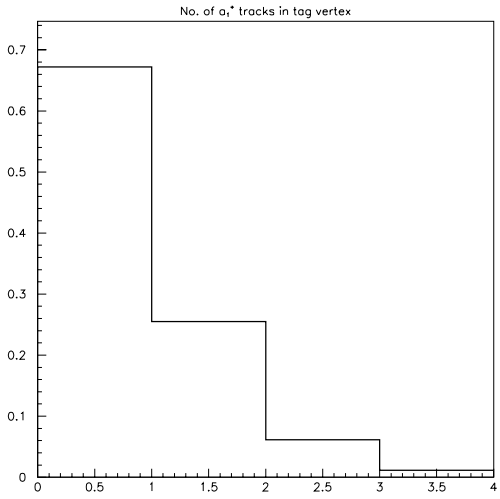

Figure 8.8: The fraction of a_1^+ daughter tracks assigned to the other B^0 vertex in $B^0 \to D^{*-}a_1^+$ events.

Chapter 9

Toy Monte Carlo Studies

9.1. Introduction

A "toy Monte Carlo" sample is a set of random events generated according to a known PDF. These samples are useful for several reasons:

- To generate and fit a sample using the same PDF tests the technical correctness of the generator and the fit engine.
- To generate and fit many statistically independent samples using the same PDF provides a robust estimate of the distribution of the fit parameters, their errors, and their correlations.
- A comparison of the results from generating and fitting a sample using different PDFs can be used to study the systematic errors due to the incorrect assumption about the fit model or the values of the fixed parameters.

- The distribution of the maximum likelihood obtained from a toy Monte Carlo study can be used to estimate the goodness of the fit of a real sample under the assumption that the fit model correctly describes the sample.

A series of studies were done as described below using toy Monte Carlo to check for inherent biases due to numerical limitations, fit parameters close to the limit, limited statistics.

9.1.1. Toy Monte Carlo Simulations of the Signal PDF

Toy Monte Carlo experiments for signal-only events used the Δt PDF that describe the signal events. The value of τ_B used to generate these events was 1.534 ps (Sec. 8.1.3), and the $\sigma_{\Delta t}$ distribution was taken from a Crystal Ball function plus Gaussian fit to the $\sigma_{\Delta t}$ distribution of the on-resonance data, a plot of the error distribution is shown in Fig. 5.7. All other parameters used to generate the signal events were taken from a fit to SP3 signal Monte Carlo. 200 toy experiments were conducted, each having 11740 events, corresponding to the number of events in the SP3 signal Monte Carlo sample. 21 of these fits either failed to converge or the cpu time of the fit exceeded the cpu time limit of the batch machine processing the fit. This shows that there is 10.5% probability for the fit to fail in SP3 signal Monte Carlo. The results of the remaining 179 experiments are shown in Fig. 9.1, and indicate a good agreement between the toy and full Monte Carlo. To study a possible statistics-

Table 9.1: Summary of results from the signal-only toy Monte Carlo experiments. All experiments were generated with $\tau_B^{\rm gen} = 1.534$ ps. $\langle\tau_B\rangle - \tau_B^{\rm gen}$ is the difference between the mean value of τ_B obtained from the fits and the generated value. The error in this quantity is taken to be rms(τ_B) divided by the square root of the number of experiments, where rms(τ_B) is the r.m.s. width of the τ_B distribution of all the experiments.

No. events/experiment	No. experiments	$\langle\tau_B\rangle - \tau_B^{\rm gen}$ (ps)	rms(τ_B) (ps)
1000	169	-0.053 ± 0.006	0.074
5000	179	-0.023 ± 0.004	0.049
11,500	179	-0.012 ± 0.003	0.033
50,000	23	-0.003 ± 0.003	0.012

dependent bias, this test was repeated with experiments containing different numbers of events. The results are shown in Tab. 9.1. It is seen that a bias exists for low statistics and diminishes at high statistics. To study the possible bias due to fitting the true Δt distribution with a Gaussian convoluted with an exponential (Sec. 8.1.3), we generate 100 Toy Monte Carlo experiments with approximately 11,000 events (the same number of events in SP3 signal Monte Carlo) with this PDF and fit it with the same PDF. We find the $\langle\tau_B\rangle - \tau_B^{\rm gen}$ (ps) $= -0.003$ ps and the rms(τ_B) $= 0.0011$ ps. Thus no bias is attributed to the fit of the true distribution of Δt.

9.1.2. Toy Monte Carlo Simulation of the Data PDF

The full fit procedure was validated on Toy Monte Carlo. 200 toy experiments were generated using the simultaneous PDF, described in Sec. 7.1, with the numbers

of events from Tab. 8.3. The value of τ_B used to generate the events was 1.534 ps i.e. the value obtained from the fit to the true Δt in Monte Carlo (Sec. 8.1.3), and the $\sigma_{\Delta t}$ distribution was taken from a Crystal Ball function plus Gaussian fit to the $\sigma_{\Delta t}$ distribution of on-resonance data (Fig. 5.7).

200 experiments were simulated, 25 of which either failed to converge or crossed the cpu time limit of the batch machine. This shows that the probability for the fit to fail in data is 12.5 %. The results of the converged 175 experiments are shown in Figs. 9.2 and 9.3. These fits are seen to have an average bias in τ_B of

$$\left\langle \tau_B^{\text{measured}} - \tau_B^{\text{generated}} \right\rangle = -0.031 \pm 0.005 \text{ ps.} \tag{9.1}$$

where the error is due to toy Monte Carlo statistics. Consequently, we correct for this bias by adding 0.031 ps (See Sec. 10.2.1 for the associated systematic error) to our data measurement of τ_B, yielding the final corrected result

$$\tau_B = 1.616 \pm 0.064 \text{ (stat) ps.} \tag{9.2}$$

9.1.3. Toy Monte Carlo studies with Different Resolution Function

To study the bias due to the choice of the resolution function for signal events we try the full toy Monte Carlo data simulation with a different resolution function to describe the signal events. We replace the 3-Gaussian resolution function of signal

Table 9.2: Summary of results from the signal-only toy Monte Carlo experiments, using the GExp resolution function. All experiments were generated with $\tau_B^{\rm gen} = 1.534$ ps. $\langle\tau_B\rangle - \tau_B^{\rm gen}$ is the difference between the mean value of τ_B obtained from the fits and the generated value. The error in this quantity is taken to be rms(τ_B) divided by the square root of the number of experiments, where rms(τ_B) is the r.m.s. width of the τ_B distribution of all the experiments.

No. events/experiment	No. experiments	$\langle\tau_B\rangle - \tau_B^{\rm gen}$ (ps)	rms(τ_B) (ps)
1000	99	-0.032 ± 0.007	0.070
5000	97	-0.016 ± 0.005	0.045
11,500	122	-0.012 ± 0.003	0.031
50,000	16	0 ± 0.005	0.014

events with a non-per-event-error outlier Gaussian plus the GExp function (a single Gaussian whose bias is fixed at 0 ps and has a floating scale plus the same Gaussian convoluted with an exponential) and repeated the study of full fit procedure. This function has been used to model signal events in the measurement of the B^0 lifetime using fully reconstruction [54]. The result of the fit is $\tau^{\rm raw} = 1.541 \pm 0.067$ (stat) ps, 0.006 ps away from the generated value of 1.534 ps.

We also conducted signal only toy Monte Carlo experiments with the GExp resolution function. The results of the signal-only experiments using GExp are summarized in Tab. 9.2. It is seen that the negative bias $\langle\tau_B\rangle - \tau_B^{\rm gen}$ in these fits is slightly smaller than with the 3-Gaussian resolution function (Tab. 9.1) for low statistic samples. At higher statistics the two resolution function yield the same bias. Thus the agreement of $\tau^{\rm raw}$ when using the 3-Gaussian or the GExp resolution function is mir-

rored in signal-only SP3-Monte Carlo fits which have approximately 11000 events. Fitting the SP3-signal Monte Carlo using the 3-Gaussian resolution function yields $\tau^{\text{raw}} = 1.506 \pm 0.033$ (stat) ps, and the GExp gives $\tau^{\text{raw}} = 1.507 \pm 0.032$ (stat) ps.

The smaller bias in GExp is also seen in full (signal + background) toy Monte Carlo. The results of these experiments are shown in Figs. 9.4 and 9.5. However, when the signal events in the full toy Monte Carlo are generated with the 3-Gaussian function and then the GExp function is used in the full toy Monte Carlo fit, we see an average bias of -0.026 ± 0.008 ps (Figs. 9.6 and 9.7). This is consistent with the -0.031 ± 0.005 ps bias obtained when the 3-Gaussian function is used for both generating and fitting the events (Figs. 9.2 and 9.3). Similarly, when generating events with the GExp function and fitting them with the 3-Gaussian function, a bias of -0.015 ± 0.007 ps is found (Figs. 9.8 and 9.9). The results of the full toy Monte Carlo fits are summarized in Tab. 9.3

Based on these tests, we conclude that using the GExp resolution function is equivalent to and consistent with using the 3-Gaussian function. To account for the differences between the entries seen in Tab. 9.3, we take an conservative systematic error of 0.016 ps.

Table 9.3: Summary of results of biases ($\langle\tau_B\rangle - \tau_B^{\rm gen}$, in ps) in the full (signal + background) toy Monte Carlo experiments. Errors are due to toy experiment statistics only, and are correlated.

Generation PDF	Fit PDF	
	GExp	3-Gaussian
GExp	-0.003 ± 0.006	-0.015 ± 0.007
3-Gaussian	-0.026 ± 0.008	-0.031 ± 0.005

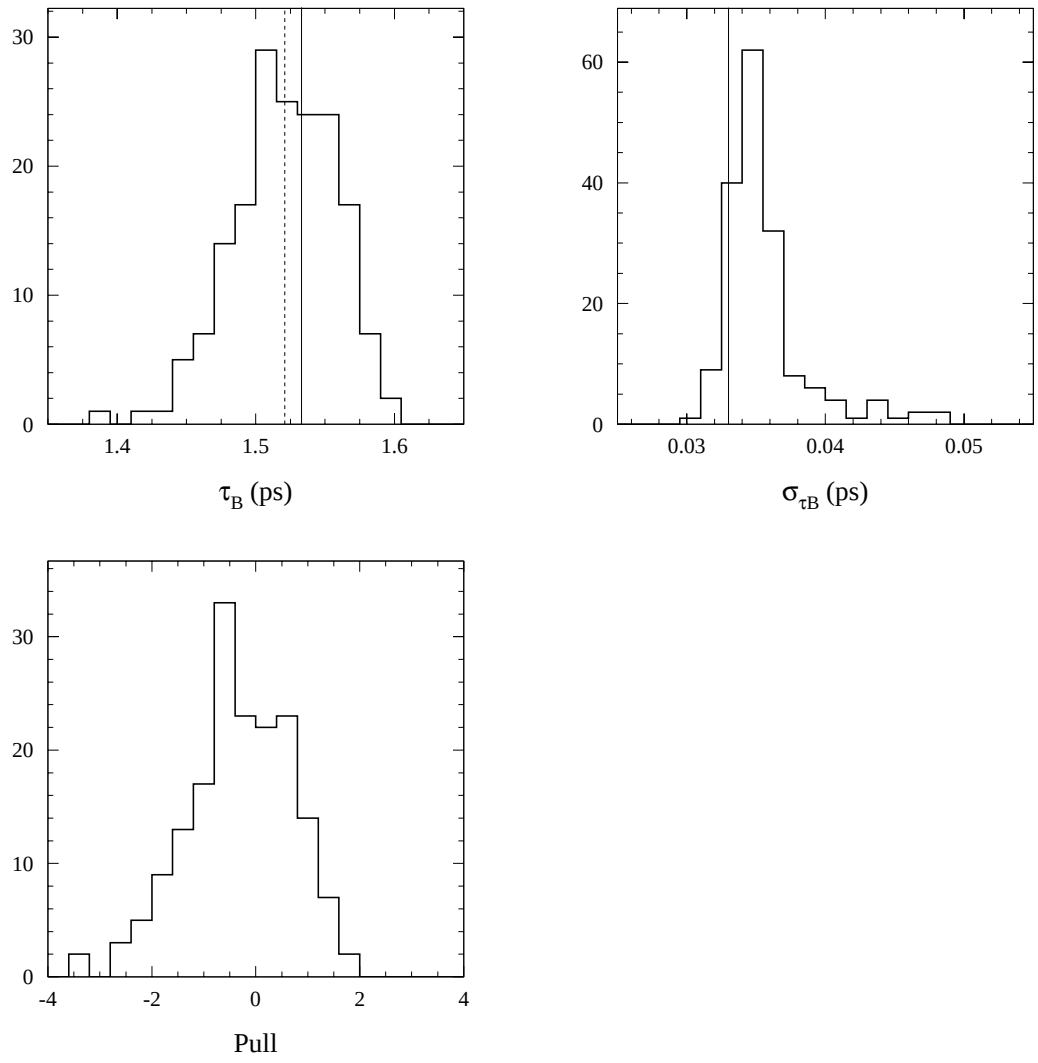

Figure 9.1: Signal-only toy Monte Carlo results, with 11740 events per experiment: Top left: Distribution of τ_B. The solid vertical line is the value with which the events were generated. The dashed line shows the mean τ_B obtained with these toy experiments. Top Right: Distribution of the τ_B statistical error. The vertical line is the value found in the fit to SP3 signal-only Monte Carlo. Bottom: Pull distribution; i.e. $\frac{\langle \tau_B \rangle - \tau_B^{\rm gen}}{\sigma_{\tau_B}}$.

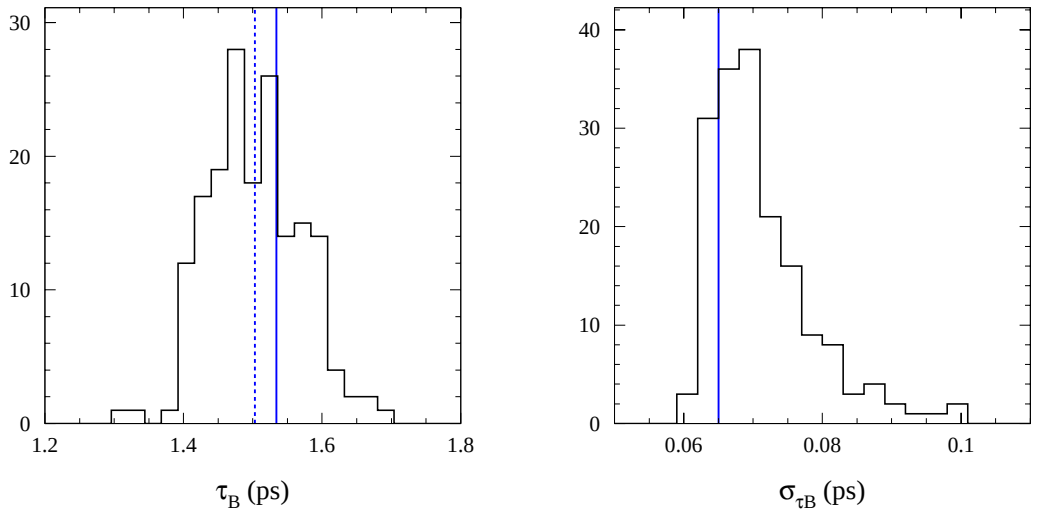

Figure 9.2: Full toy Monte Carlo results: Left: τ_B distribution. The solid vertical line shows the value generated (1.534 ps), and the dashed-line indicates the mean measured value (1.503 ps). Right: Error in τ_B. The vertical line is the value obtained from the fit to the data.

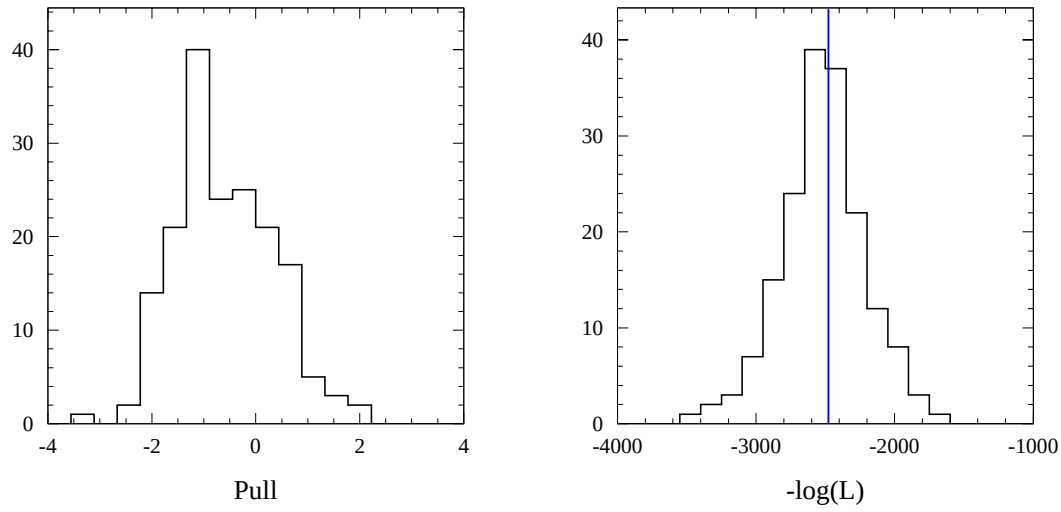

Figure 9.3: Full toy Monte Carlo results: Left: τ_B pull distribution. Right: $-\log(\text{likelihood})$ distribution; i.e. goodness of fit. The vertical line is the value obtained from the fit to the data.

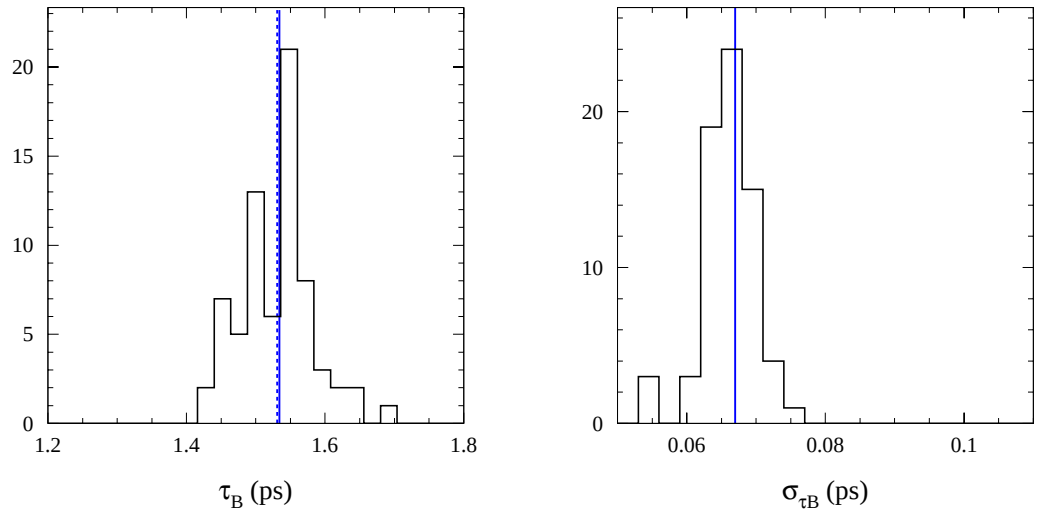

Figure 9.4: Full toy Monte Carlo results when using the GExp resolution function: Left: τ_B distribution. The solid vertical line shows the value generated (1.534 ps), and the dashed-line indicates the mean measured value (1.531 ps). Right: Error in τ_B. The vertical line is the value obtained from the fit to the data.

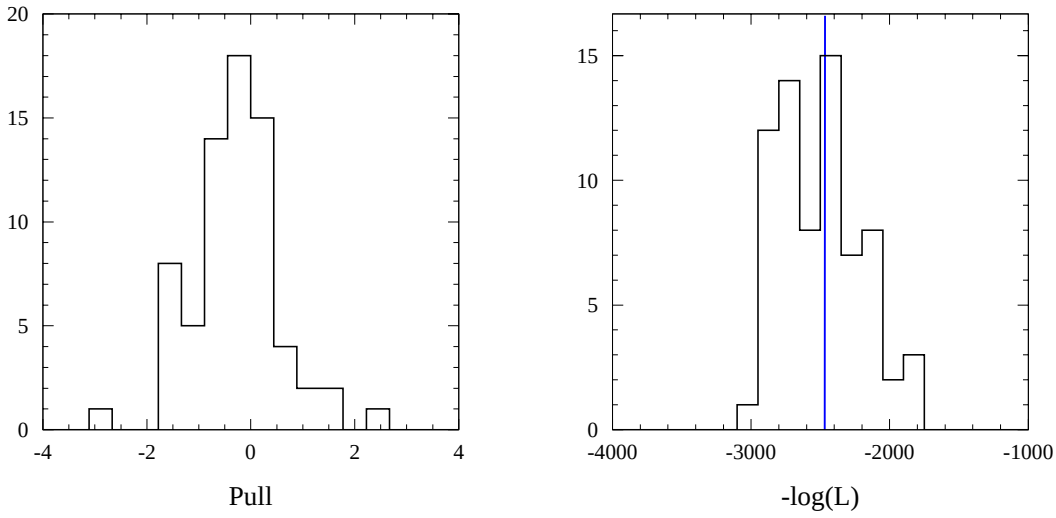

Figure 9.5: Full toy Monte Carlo results when using the GExp resolution function: Left: τ_B pull distribution. Right: $-\log(\text{likelihood})$ distribution. The vertical line is the value obtained from the fit to the data.

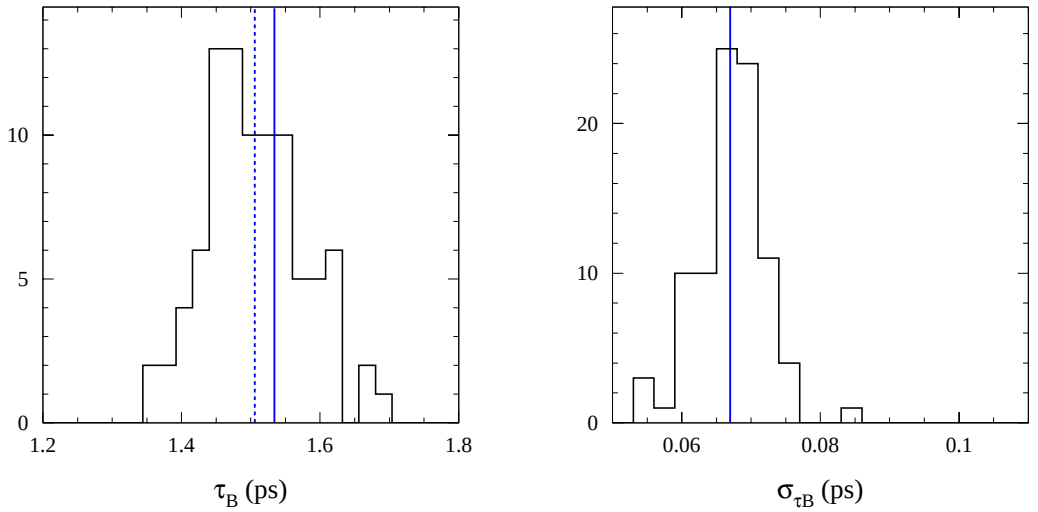

Figure 9.6: Full toy Monte Carlo results when signal events are generated using the 3-Gaussian resolution function, but the GExp resolution function is used in the fit: Left: τ_B distribution. The solid vertical line shows the value generated (1.534 ps), and the dashed-line indicates the mean measured value (1.531 ps). Right: Error in τ_B. The vertical line is the value obtained from the fit to the data.

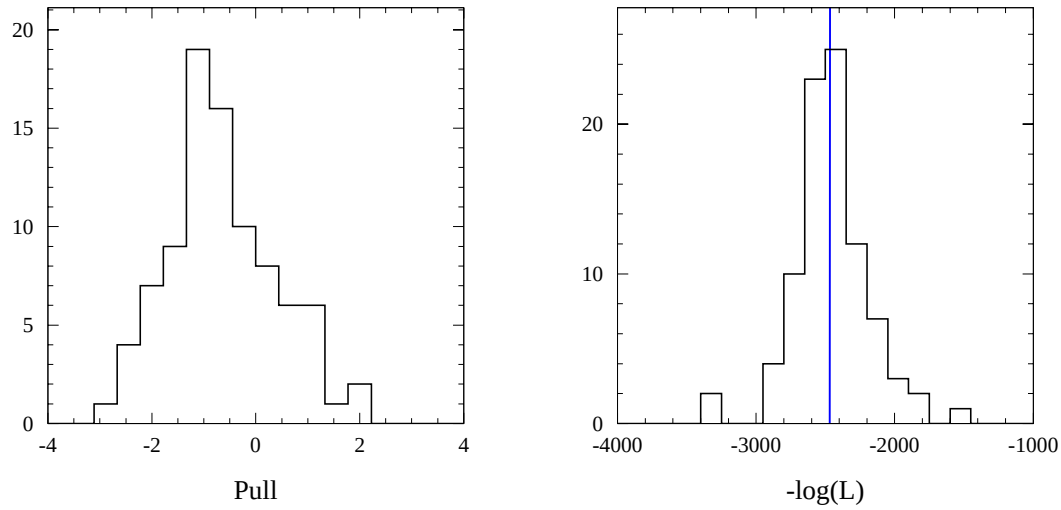

Figure 9.7: Full toy Monte Carlo results when signal events are generated using the 3-Gaussian resolution function, but the GExp resolution function is used in the fit: Left: τ_B pull distribution. Right: $-\log(\text{likelihood})$ distribution. The vertical line is the value obtained from the fit to the data.

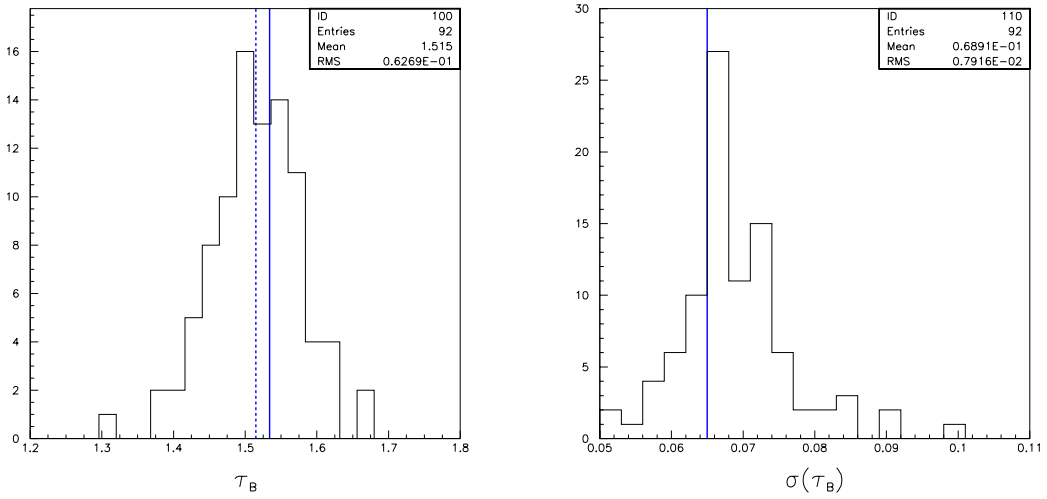

Figure 9.8: Full toy Monte Carlo results when signal events are generated using the GExp resolution function, but the 3-Gaussian resolution function is used in the fit: Left: τ_B distribution. The solid vertical line shows the value generated (1.534 ps), and the dashed-line indicates the mean measured value (1.531 ps). Right: Error in τ_B. The vertical line is the value obtained from the fit to the data.

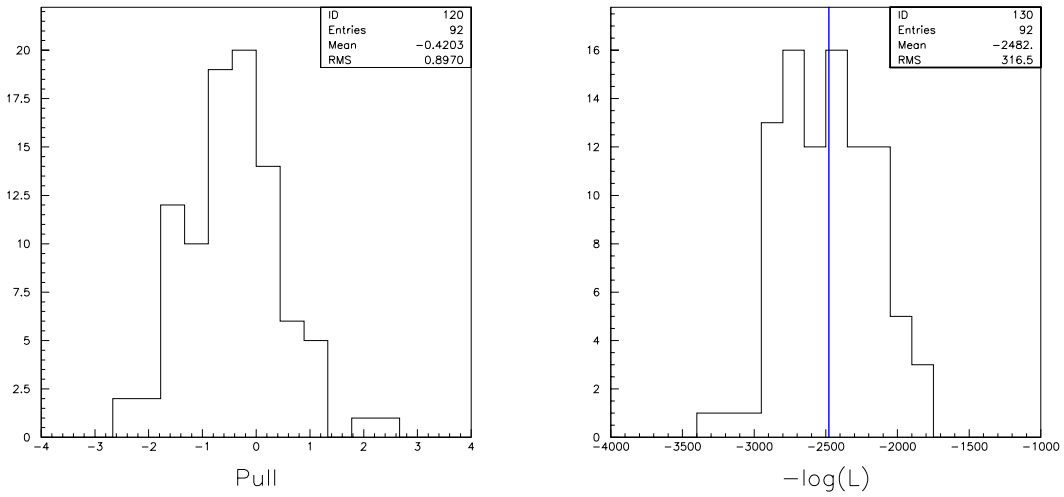

Figure 9.9: Full toy Monte Carlo results when signal events are generated using the GExp resolution function, but the 3-Gaussian resolution function is used in the fit: Left: τ_B pull distribution. Right: $-\log(\text{likelihood})$ distribution. The vertical line is the value obtained from the fit to the data.

Chapter 10

Systematic Uncertainties

10.1. Introduction

The measurement of the B^0 lifetime using the technique of partial reconstruction is complimentary to the same measurement using full reconstruction. The advantage of using the former is the increase in statistics, the disadvantage is that it is a novel technique and many new potential sources of systematic error had to be considered. One could not rely on the systematic error studies done for other time-dependent measurements in *BABAR* that use fully reconstructed events. The signal to background level is 0.61 compared to approximately 4 for full reconstruction so a great deal of work had to go done to understand the influence of the backgrounds on the final result. The following subsection outlines the systematic error studies conducted. A summary of the systematic errors is presented in Table. 10.1. The total systematic error from all contributions is 0.075 ps.

10.1.1. Propagation of Control Sample Kinematic Fit Statistical Errors

The signal, background kinematic parameters and the background Δt parameters were fixed while Δt was fitted in the signal region for $\tau_{_B}$. Hence the effect on the measurement of $\tau_{_B}$ due to these fixed parameters was studied by varying the fixed parameters by their respective errors. The associated change in $\tau_{_B}$ contributes to the final systematic error.

As described in Sec. 7.1.8 the Δt parameters of the combinatoric and peaking background are obtained from fits to data control samples, with an error matrix to represent not just the statistical errors but also taking into account correlations between the floating parameters. A similar error matrix is obtained from the kinematic fit that precedes the Δt fit in the signal-region. The following procedure is used to propagate these errors to the final Δt fit.

Let V be the $N \times N$ error matrix of the fit, and $\mathbf{p}$ be the corresponding vector of N floating parameters of the fit, which are later fixed in the signal-region fit. T is a unitary matrix such that $D \equiv TVT^{-1}$ is a diagonal matrix. Then D is a representation of the errors in a basis in which they are uncorrelated. Similarly, $\mathbf{q} \equiv T\mathbf{p}$ is the representation of the parameters in that basis. $\mathbf{q}^{\pm,i}$ is a vector identical to $\mathbf{q}$, except that the ith element ($i \in [1, N]$) has been varied by $\pm\sqrt{D_{ii}}$ from its

original value:

$$\mathbf{q}^{\pm,i} \equiv \begin{pmatrix} q_1 \\ \cdots \\ q_i \pm \sqrt{D_{ii}} \\ \cdots \\ q_N \end{pmatrix}. \tag{10.1}$$

This corresponds to a $\pm 1\sigma$ variation of the uncorrelated i^{th} error. The transformation $\mathbf{p}^{\pm,i} \equiv T^{-1}\mathbf{q}^{\pm,i}$ produces the corresponding values of the parameters in the original basis. The two vectors, $\mathbf{p}^{\pm,i}$, are then used in the signal-region fit to obtain two new values of the B^0 lifetime, $\tau_{B}^{\pm,i}$. The total systematic error associated with the error matrix V is taken as

$$\sigma = \sqrt{\sum_{i=1}^{N} \frac{\left(\tau_{B}^{+,i} - \tau_{B}\right)^2 + \left(\tau_{B}^{-,i} - \tau_{B}\right)^2}{2}}. \tag{10.2}$$

where τ_{B} is the nominal fit result.

Using this procedure to propagate the error matrix of the kinematic fit to the Δt fit, we find a total error in τ_{B} of 0.029 ps.

In the case of the sideband fit for the combinatorial $B^0\overline{B}^0$, each vector $\mathbf{p}^{\pm,i}$ was first used in a wrong-sign fit to obtain a new set of peaking $B^0\overline{B}^0$ parameters, before proceeding to the signal-region fit. The error in τ_{B} is 0.033 ps.

The error obtained by propagating the error matrix of the wrong-sign fit, for the

peaking $B^0\overline{B}^0$ parameter is 0.002 ps.

10.1.2. Monte Carlo Statistics

The $D_{\rm miss}$ correction factor, R_{D^0}, is obtained with a 2.2% relative error, due to signal Monte Carlo statistics Sec. 8.1.2. This translates to an error of $1.616 \times 0.022 = 0.036$ ps in $\tau_{_B}$. All the kinematic variables for the various background events were obtained from Monte Carlo and are varied according to the method described in Sec. 10.1.1. The resulting error in $\tau_{_B}$ is 0.014 ps. Limited Monte Carlo statistics in the true lifetime measurement, Sec. 8.1.3, results in a 0.013 ps systematic error. The $B^0 \to D^{*-}a_1^+$ bias (Sec. 8.1.1) is known up to an error of 0.011 ps, which is determined by $B^0 \to D^{*-}a_1^+$ Monte Carlo statistics. Limited Monte Carlo statistics translates into a systematic error.

10.1.3. R_{D^0} Correction

The D^0 bias correction factor R_{D^0} is obtained from signal Monte Carlo. A good agreement between the data and Monte Carlo distribution of the number of $D_{\rm miss}$ daughter tracks assigned to the other vertex, $N_{\rm tr}^D$ is shown in Fig. 7.10. Extensive studies were conducted with high statistics, partially reconstructed, $B^0 \to D^{*-}l^+\nu$ Monte Carlo and data [56]. These also show good agreement, in the distribution of $N_{\rm tr}^D$ between data and Monte Carlo. To account for a systematic effect due to an

uncertainty in Monte Carlo to generate tracks that go to the other B^0 vertex, we vary the fraction of events for which $N_{\rm tr}^D = 0$ by $\pm 5\%$ in signal Monte Carlo. The fraction of $N_{\rm tr}^D$ to the total number of tracks in the other B^0 vertex changes from 66 % to 71 % and 61 % respectively when $N_{\rm tr}^D = 0$ is changed by $\pm 5\%$. The associated change in R_{D^0} and $\tau_{_B}$ is 0.999, $\tau_{_B} = 1.533 \pm 0.034\,$ps and 0.967, $\tau_{_B} = 1.480 \pm 0.035\,$ps. Thus a variation of $^{+0.018}_{-0.015}$ in R_{D^0}, translates to ∓ 0.027 ps variation in $\tau_{_B}$. An additional error in R_{D^0} is due to Monte Carlo statistics, Sec. 10.1.2.

10.1.4. Level of $\overline{B} \to D^{**}\rho^+$ Background

From Table. 7.6 we see that in the nominal fit we set the contribution of $\overline{B} \to D^{**}\rho^+$ events, $f_{D^{**}}$ to 0. To evaluate the systematic error associated with this assumption, we take

$$Q^{**} \equiv BR(\overline{B} \to D^{**}\rho^+) \cdot BR(D^{**} \to D^{*+}\pi) = 0.3\%. \tag{10.3}$$

The reasoning behind this value of Q^{**} is described in reference [57]. From the $\overline{B} \to D^{**}\rho^+$ Monte Carlo corresponding to an integrated luminosity of 70 fb^{-1}, 8309 events satisfied all the criteria for a signal event. From this we can estimate that there will be approximately 2400 events in 20 fb^{-1}. This corresponds to approximately 24% of the total $N_{B\bar{B}} = 10,000$ events found by the kinematic fit. Hence $f_{D^{**}}$ is fixed to this fraction. With this value of $f_{D^{**}}$, we repeat the kinematic fit, floating

only the parameters f_{qq} and $(f_{D^{**}} + f_{B\overline{B}})/(1 - f_{qq})$ resulting in a contribution of 2425 $\overline{B} \to D^{**}\rho^+$ events in the data sample. We then proceeded to carry out the Δt fit, with the $\overline{B} \to D^{**}\rho^+$ Δt parameters taken from Monte Carlo. The change in $\tau_{_B}$ with respect to the nominal result is 0.023 ps.

10.1.5. Variation of Fixed Parameters

The scale of the continuum outlier Gaussian is fixed at 10 ps. Varying it between 8 and 12 ps results in a variation of ± 0.015 ps in $\tau_{_B}$. The mean of the continuum outlier Gaussian is fixed at 0 ps. Varying it between ± 1 results in a variation of 0.001 ps. The bias of the outlier signal Gaussian is fixed at 0 ps. Varying it between ± 3 ps yields a change in $\tau_{_B}$ of 0.001 ps. The scale of the outlier signal Gaussian is fixed at 8 ps. Varying it between ± 2 ps yields a change in $\tau_{_B}$ of 0.0001 ps.

10.1.6. Uncertainty in $\boldsymbol{BR(B^0 \to D^{*-}a_1^+)/BR(B^0 \to D^{*-}\rho^+)}$

In the kinematic fit the fraction $N_{D^*a_1}/(N_{D^*a_1} + N_{D^*\rho})$ is set to 11.61 %, which is obtained from Monte Carlo. Hence a systematic error arises due to the uncertainty in the ratio of branching fractions $R_{a_1} \equiv BR(B^0 \to D^{*-}a_1^+)/BR(B^0 \to D^{*-}\rho^+)$. Taking the branching fractions and their errors from the CLEO collaboration measurements [31], we assign a relative error of 31% to R_{a_1}. Varying the value of R_{a_1} used in the data fits by ± 0.31 results in a $^{+0.003}_{-0.002}$ ps change in $\tau_{_B}$. Taking into account the variation

in $\Delta t_{a_1}^{\rm bias}$ due to the variation in R_{a_1} yields a total variation of ± 0.005 ps in $\tau_{_B}$. Note that when R_{a1} is varied the fraction $f_{peakB\bar{B}}$ is still maintained at 9.6 %, Table. 7.6.

10.1.7. Level of Peaking Background

The ratio between the number of peaking background and the sum of the number of signal events and peaking background events in the data is set to 9.6%, the value obtained from Monte Carlo. We expect the simulation of this ratio to be accurate, since it depends only on the probability of substituting the π_f for a track from the other B^0 meson. When this ratio is varied in the data fit by $\pm 5\%$, $\tau_{_B}$ varies by ± 0.003 ps. An additional error associated with the peaking background is described in Sec. 10.1.1.

10.1.8. Bias due to Fully Reconstructed Events

As shown in Sec. 7.1.6, fitting signal Monte Carlo events with or without including fully reconstructed events results in very small difference in the value of $\tau_{_B}$ obtained from the fit. To account for a possible bias, we take the average difference between the fits obtained with the different cone cuts, which is 0.001 ps.

10.1.9. Machine and Detector

Uncertainties in the detector alignment can influence the Δz reconstruction and thus change the Δt resolution function. As we obtain most of the parameters of the resolution function from data, most of the misalignment effects are automatically taken into account. A detailed study of the possible effects to the measurement of the B^0 lifetime has been done in [54], where an error of 0.008 ps is assigned to the effect of detector misalignment. We assume a similar error in this analysis.

The uncertainties in the boost parameters of the machine is about 0.1 % [58]. Since the lifetime depends linearly on the boost parameters we assign a 0.1 % error to the lifetime due to variations in the value of the boost.

Various alignment and calibration procedures use the data to estimate the size of the relative displacement of different sub-detector components. These procedures do not determine or adjust the global length scale of the experiment. Uncertainties in the z scale of the detector biases the B lifetime measurement. One way to determine the z scale is a measurement of the length of something with known dimensions. One measurement of the length of the beryllium beam pipe [59] using protons from material interaction and in the tantalum foil wrapped around it as described in [60]. For the alignment sets C,D,E, the scale factor $f = \frac{\text{length seen by detector}}{\text{length from independent measurement}}$ is consistent with one or two per mil level. This z scale determination predominantly uses tracks that pass the extremities (in z) of the silicon tracker. There is no reason

to expect the z scale of the inner regions of the silicon tracker to be an order of magnitude worse than that of the outer region, and assign 0.4 % as the uncertainty on the z scale in these alignment sets.

10.2. Additional Cross-Checks

We perform a series of consistency checks that are not a part of the systematic error calculation. These studies were done to check for the stability of the measured lifetime as a function of various quantities.

10.2.1. Resolution Function

Additional checks were made regarding the choice of the resolution function and its effect on the measurement of $\tau_{_B}$. The signal resolution function was modified so that the Gaussian biases also scale with $\sigma_{_{\Delta t}}$, changing Eq. (7.11) to

$$G(\Delta t, \sigma_{_{\Delta t}}; b, s) \equiv \frac{1}{\sqrt{2\pi}s\sigma_{_{\Delta t}}} \exp\left(-\frac{(\Delta t - b\sigma_{_{\Delta t}})^2}{2s^2}\right). \tag{10.4}$$

The result of this fit is $\tau_{_B}^{\rm raw} = 1.547 \pm 0.072$ (stat) ps. Comparing with Eq. (8.2), the change in $\tau_{_B}^{\rm raw}$ is 0.012 ± 0.033 ps, but with a significantly larger error. This difference is accounted for by the 0.016 ps error, Sec. 9.1.3. Fitting SP3 signal Monte Carlo using the resolution function defined in Eq. (10.4), we obtain $\tau_B = 1.505 \pm 0.033$ ps, consistent with the result obtained with Eq. (7.11). We conclude therefore that within

the errors, no significant systematic effect can be associated with the choice of scaling or not scaling the signal Gaussian bias with the per-event errors.

We also repeat the fit using the Gaussian convoluted with an exponential, GExp, function, Sec. 9.1.3 and the result of the fit to data is $\tau_B^{\rm raw} = 1.541 \pm 0.067$ ps. Comparing with Eq. (8.2), the change in $\tau_B^{\rm raw}$ is 0.006 ± 0.020 ps.

The results of the fits to the data and signal Monte Carlo using the three signal resolution functions studied here are summarized in Tab. 10.2.

10.2.2. Cone Cut Variation

To check for possible biases to the B^0 lifetime due to the choice of the cone cut of 1 radian, the full fit procedure was repeated for events passing the 0.6, 0.8, 1.2 and 1.4-radian cone cuts. The values of R_{D^0}, $\tau_B^{\rm raw}$, and τ_B obtained with each of the 5 cone cuts are summarized in Tab. 10.3. The consistency between the results of the different cone cuts is displayed in Fig. 10.1. In this figure, the errors shown are the τ_B errors quoted in Tab. 10.3, subtracted in quadrature from the error of the 1-radian cone cut result. Using this measure of the uncorrelated errors, the χ^2 probability for all the results to be consistent with the 1-radian result is 23.3%. The 0.8- and 1.2-radian results are consistent with the 1-radian result at the 55% confidence level.

We therefore conclude that the results obtained with the different cone cuts are consistent. It should be noted that separate evaluation of all the systematic errors

for the different cone cuts will most likely result in higher confidence levels.

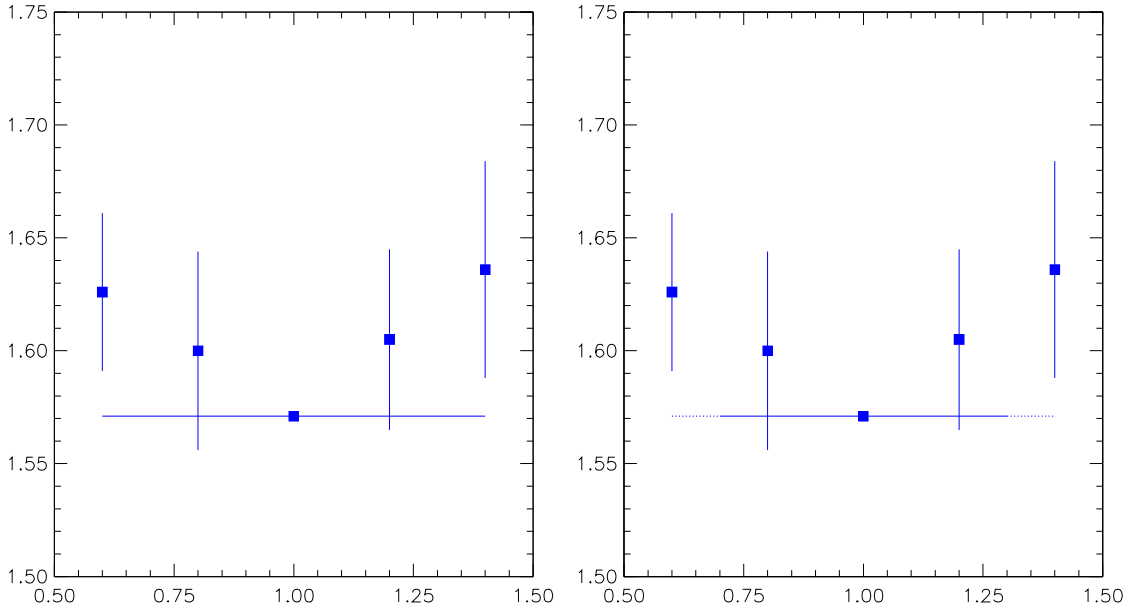

Figure 10.1: τ_B vs. the cone cut. The errors are the τ_B errors quoted in Tab. 10.3, subtracted in quadrature from the error of the 1-radian cone cut result. The χ^2 probability for all the results to be in agreement is 23.3% (left). The probability for just the 0.8- and 1.2-radian cone cut results to be consistent with the 1-radian result is 55% (right).

10.2.3. Parameters of the π_f and Alignment Set

The full fit procedure was performed in bins of the polar angle θ (measured with respect to the z axis) and the azimuthal ϕ to check for dependencies on detector

acceptance. Only the π_f daughter of the ρ is used along with the beam spot constraint to determine z_{rec}. To check for a possible bias to the lifetime due to the momentum of π_f the full procedure was also done in momentum bins of the π_f. As the data is made up of four different alignment sets to study for a possible bias due to this the full fit procedure was done on each of the four alignment sets A, C, D, E. The results of the studies are summarized in Figs. 10.2 and 10.3. Flat line fits of these plots give χ^2 probabilities of 75%, 37%, 8%, and 90%, respectively for the 4 figures. This is consistent with the results being independent of the binning parameter.

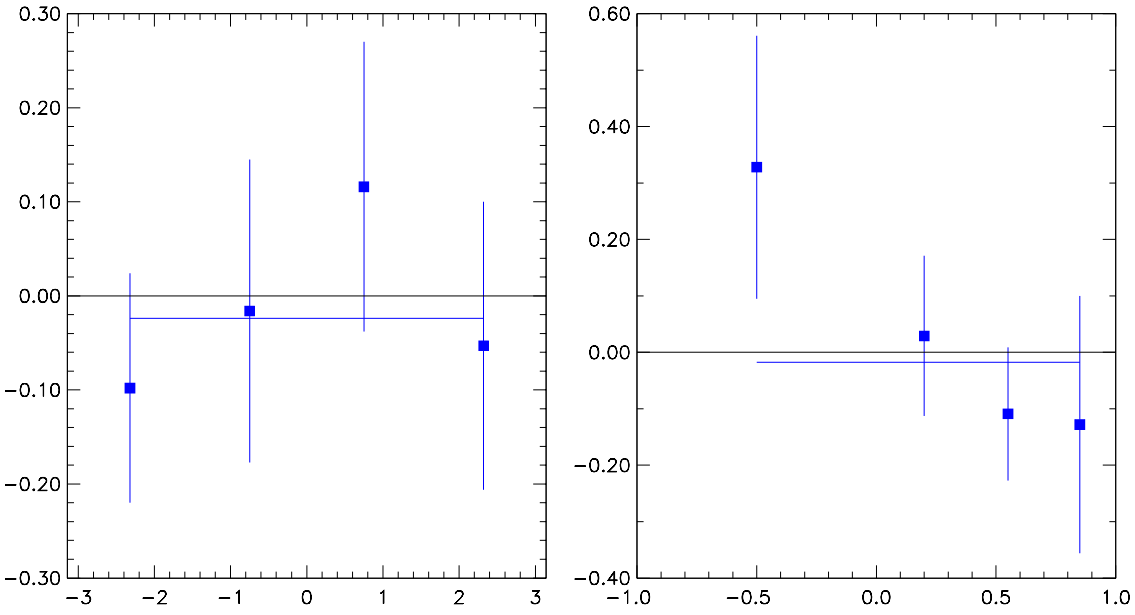

Figure 10.2: Difference from nominal τ_B obtained when fitting the data in bins of the azimuthal angle (left) or $\cos\theta$ (right) of the π_f in the lab frame.

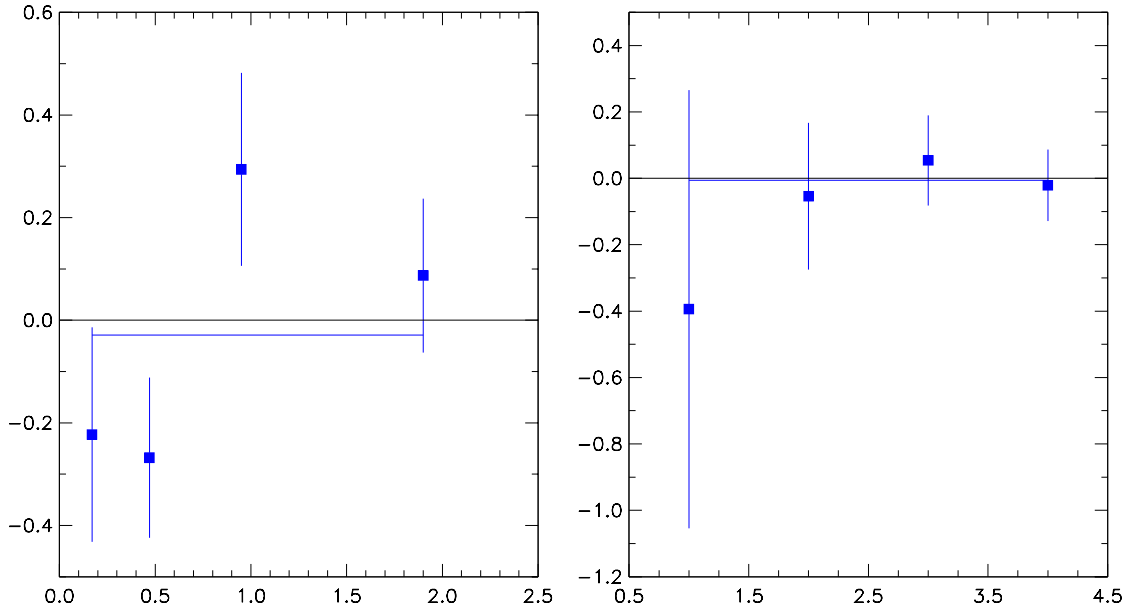

Figure 10.3: Difference from nominal τ_B obtained when fitting the data in bins of the momentum of the π_f in the lab frame (left), or when separating the data by local alignment set (right). The alignment sets are 1 =A, 2 =C, 3 =D, 4 =E.

10.3. Discussion of the systematic errors

From Table. 10.1 we note that the contribution to the systematic error due to Monte Carlo statistics is 0.042 ps, hence a factor four increase in Monte Carlo statistics will help reduce this error by almost a factor of two(taking roughly into account the effect of background events also). Another significant contribution is from the statistics used in data sideband fit and the kinematic fit which contribute 0.044 ps to the total systematics using more data will help reduce this contribution. data

compared to With the use of more data the contributions from the fit bias may also reduce with an increase in the number of signal events, as shown by toy Monte Carlo studies[1]. Having Monte Carlo represent data in a more consistent way would help reduce the errors due to the uncertainties in the number of D^0 tracks that make it into the other B^0 vertex, that now contributes to a systematic error of 0.026 ps. The systematics of 0.01 ps due to global uncertainties are a minor contributions to the total systematics in this analysis.

There is room for improvements to reduce the total systematic error in future analysis using the data collected in the most recent run.

10.4. Conclusions

The measured B^0 lifetime using a sample of partially reconstructed $B^0 \to D^{*-}\rho^+$ events is

$$\tau_{_B} = 1.616 \pm 0.064 \pm 0.075\,\text{ps}. \tag{10.5}$$

This value is consistent with the measured B^0 lifetime using fully reconstructed hadronic decay modes with the same integrated luminosity $\tau_{_B} = 1.546 \pm 0.032 \pm 0.022\,\text{ps}$.

This is the first measurement of the B^0 lifetime using partially reconstructed

[1]With the present data set of 80 fb^{-1} in *BABAR* we could use a cone cut of 1.4 radian instead of the 1 radian, thereby reducing the number of background events.

$B^0 \to D^{*-}\rho^+$ events. The consistency of the result between two complementary procedure validates the use of partial reconstruction for time-dependent analysis. *BABAR* has already started to work toward a measurement of $\sin(2\beta+\gamma)$ using partial reconstruction and a result is expected in the near future.

Table 10.1: Summary of systematic errors. In the section column we refer the reader to the section where the particular systematic error is discussed.

Source	Error (ps)	Section
Statistical error of sideband fit	0.033	10.1.1
Statistical error of kinematic fit	0.029	10.1.1
Statistical error of wrong-sign fit	0.002	10.1.1
Monte Carlo statistics: R_{D^0}	0.036	10.1.2
Monte Carlo statistics: kinematic parameters	0.014	10.1.2
Monte Carlo statistics: Event selection bias	0.013	10.1.2
Monte Carlo statistics: $B^0 \to D^{*-} a_1^+$ bias	0.011	10.1.2
R_{D^0} correction	0.027	10.1.3
Level of $\overline{B} \to D^{**}\rho^+$ background	0.023	10.1.4
Likelihood fit bias	0.016	10.2.1
Variation of fixed parameters	0.015	10.1.5
$Br(B^0 \to D^{*-} a_1^+)/Br(B^0 \to D^{*-}\rho^+)$	0.005	10.1.6
Level of peaking background	0.003	10.1.7
Bias from fully reconstructed events	0.001	10.1.8
SVT misalignment	0.008	10.1.9
Z-scale uncertainty $\pm 0.4\%$	0.007	10.1.9
Boost parameters $\pm 0.1\%$	0.002	10.1.9
Total	0.075	

Table 10.2: Summary of results of fits to the data and signal Monte Carlo using different signal resolution functions. Errors are statistical only.
.

Resolution function	$\tau_B^{\rm raw}$ (ps), data	$\tau_B^{\rm raw}$ (ps), signal Monte Carlo
Eq. (7.11)	1.535 ± 0.064	1.506 ± 0.032
Eq. (10.4)	1.547 ± 0.072	1.505 ± 0.033
GExp	1.541 ± 0.067	1.507 ± 0.032

Table 10.3: Results of the fits obtained with the different cone cuts, used to create Fig. 10.1. $\tau_{B}^{\rm true}$ is the lifetime obtained from signal Monte Carlo truth (Sec. 8.1.3). R_{D^0} is the ratio between the lifetime measured on signal Monte Carlo and $\tau_{B}^{\rm true}$, with the errors of the numerator and denominator taken to be fully correlated. $\tau_{B}^{\rm raw}$ is the value of the lifetime obtained in the fit, with only the statistical error due to the fit. $\tau_{B}^{a_1}$ is the value of $\tau^{\rm raw}$, corrected for the $B^0 \to D^{*-} a_1^+$ bias (Sec. 8.1.1). The error includes the Monte Carlo statistics error from the evaluation of the bias. $\tau_{B} = \tau_{B}^{a_1}/R_{D^0}$.

	0.6 radian	0.8 radian	1.0 radian	1.2 radian	1.4 radian
$\tau_{B}^{\rm true}$ (ps)	1.530	1.530	1.533	1.537	1.542
	± 0.013	± 0.013	± 0.013	± 0.013	± 0.013
R_{D^0}	0.923	0.958	0.982	0.987	1.003
	± 0.019	± 0.029	± 0.020	± 0.021	± 0.022
$\tau_{B}^{\rm raw}$ (ps)	1.493	1.525	1.535	1.576	1.633
	± 0.067	± 0.066	± 0.064	± 0.074	± 0.079
$\tau_{B}^{a_1}$ (ps)	1.504	1.537	1.543	1.582	1.646
	± 0.068	± 0.067	± 0.064	± 0.075	± 0.080
τ_{B} (ps)	1.629	1.604	1.571	1.602	1.641
	± 0.081	± 0.085	± 0.073	± 0.083	± 0.087

Appendix A

The DIRC - Operational Experience and Performance Studies

As part of her research training at the Stanford Linear Accelerator Center the author spend much of the last eighteen months of her doctoral studies involved with the daily operation of the DIRC. As the work was not a central part of her thesis analysis a more complete description of the device and a summary of her DIRC studies is included in this appendix for completeness.

The DIRC, [61] is a new type of detector for particle identification used in the barrel region of the *BABAR* detector. It is a Cherenkov ring imaging device which utilizes totally internally reflecting Cherenkov photons in the visible and near UV range [62]. This technique reduces space requirements and increases the particle identification performance as compared to ring imaging detectors of the previous generation. It provides the identification of pions, kaons and protons for momenta up

to 4 GeV/c with high efficiency.

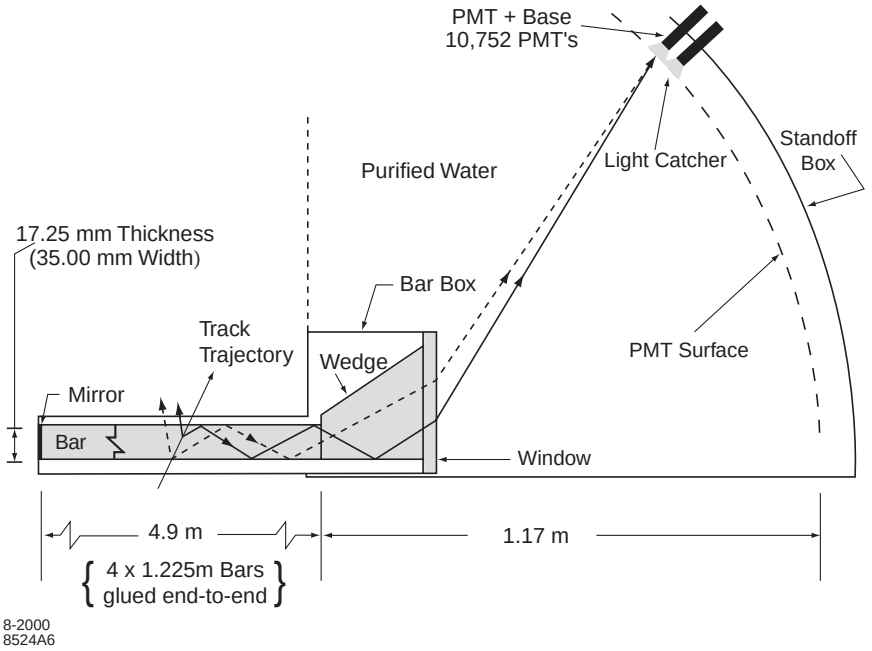

Figure A.1: Schematic of the DIRC fused silica radiator bar and imaging region.

A.1. Principle of the DIRC

Figure A.1 shows a schematic of the DIRC geometry that illustrates the principles of light production, transport, and imaging. The DIRC uses thin, long rectangular bars made of synthetic fused silica (quartz) [29] (H × W × L = 17 mm × 35 mm × 4900 mm) both as Cherenkov radiators and light guides (refractive index $n \approx 1.47$), this material was chosen because of its resistance to ionising radiation, its long attenuation length, large index of refraction, small chromatic dispersion within the wavelength acceptance of the DIRC and because it allows an excellent optical finish

of the bar surfaces [63]. Bars are glued together from four pieces, each 1225 mm long. Altogether, 144 bars are arranged in a 12-sided polygonal barrel with a radius of about 84 cm around the beam axis. The DIRC bars extend 178 cm forward from the interaction point of *BABAR* covering 87% of the polar solid angle in the center-of-mass frame. The azimuthal coverage is 93%, since there are gaps between the bars at the 12 sides of the radiator polygon. Each group of 12 bars are housed in a bar box surrounded by nitrogen at NTP (index $n \approx 1$). The overall assembly of the detector is shown in Fig. A.2. The radiation length of bars at normal incidence is X_0 = 14% and X_0 = 19% for the full assembly. In the following, the variable θ_c is used to designate the Cherenkov angle, ϕ_c denotes the azimuthal angle of a Cherenkov photon around the track direction, and n represents the mean index of refraction of fused silica ($n = 1.473$). The Cherenkov angle is given by the familiar relation and a cartoon illustrating the principle is shown in Fig. A.3

$$\cos\theta_c = 1/n\beta. \tag{A.1}$$

$\beta = \frac{v}{c}$, v = velocity of the particle, c = velocity of light. Since the refractive index of the radiator bar n is larger than $\sqrt{2}$, a certain fraction of the Cherenkov photons produced by a relativistic charged particle traversing the quartz bar will undergo total internal reflection, regardless of the incidence angle of the tracks, and propagate along the length of the bar. Only one end of the bars is instrumented and a mirror

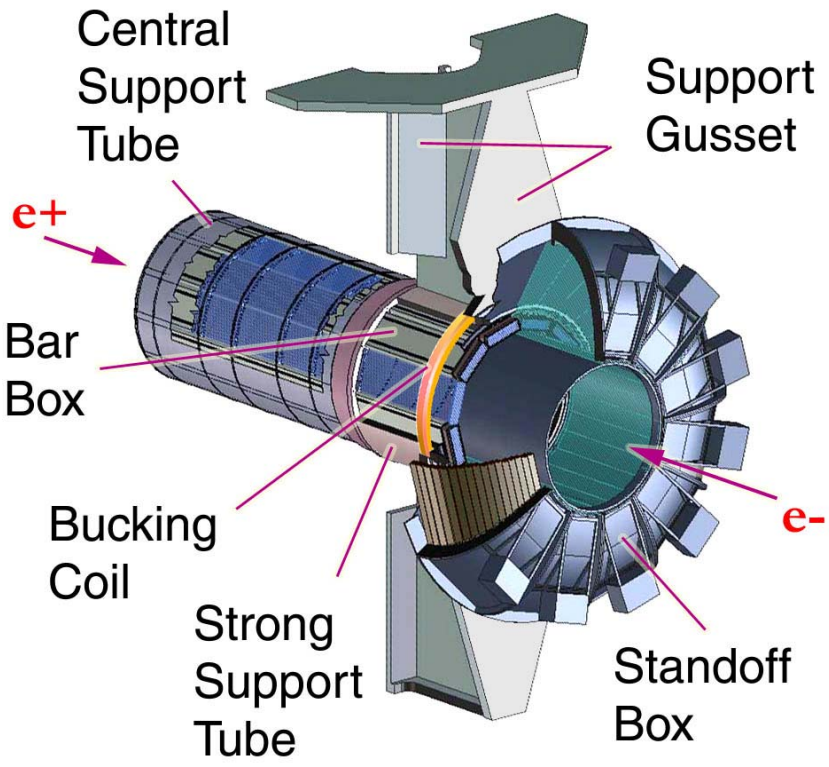

Figure A.2: Schematical view of the DIRC assembly within *BABAR*.

(reflectivity $\approx 92\%$) is placed perpendicular to the bar axis on the other end, where positrons enter the *BABAR* detector. Due to the boost of the $\Upsilon(4S)$ in the lab frame, the density of charged tracks is enhanced on this side and hence it is less preferable for readout. The bars are made of high optical precision (mean surface reflectivity $\approx 99.96\%$ per bounce at 442 nm photon wavelength and opposing faces parallel to 25 mrad), the initial direction of the photon is captured within the rectangular bar during its propagation.

Photons exiting the bar in downward direction, or with large angles in radial

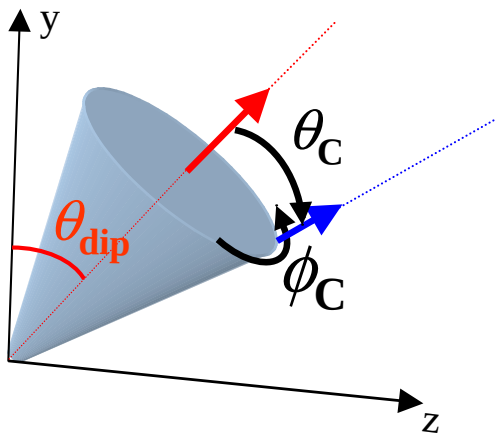

Figure A.3: A cartoon illustrating the principle of Cherenkov angle.

direction, are partly recovered into the instrumented area by a prism at the readout end, Fig. A.1. This optical element is 91 mm long and the top side has a 30 degree opening angle. The bottom side is slightly tilted upwards by 6 mrad to recover the downward going photons that would otherwise hit the support tube. The prism reduces the required photon-sensitive area by more than a factor of two with only a modest effect on reconstruction due to the two ambiguities introduced by the wedge.

A thin (9 mm) quartz window separates the prism from the so-called stand-off box (SOB), a water tank filled with 6000 liters of purified water (refractive index

$n \approx 1.33$) in a toroidal shape (see Fig. A.1). The backplane of the SOB is divided into 12 sectors, each equipped with 896 conventional photo-multiplier tubes The PMTs have a quantum efficiency of approximately 25% at 400 nm wavelength, spectral range: 250 nm – 650 nm, pointing to the exit of a corresponding bar box. Hexagonal reflectors (light catchers) with water-resistant rhodium surfaces surround the photomultiplier tubes forming a honeycomb of reflecting surface that improves the photon detection efficiency by about 20%.

The ratio of the refractive indices of the quartz and water is nearly wavelength independent. Due to this ratio the internal reflection at the readout side of the bar is reduced. Furthermore, the exit angle is magnified by this ratio, increasing the position resolution of the photons. The detector provides a three-dimensional measurement of the photon from the photon exit angles, α_x, α_y with respect to the bar axis and the hit time t_{hit} of the photon. A cartoon to illustrate the DIRC as a three-dimensional imaging device is shown in Fig. A.4. Knowledge of the spatial position of the bar through which the track passes and the photo-tube hit time within a certain readout time interval is used to reconstruct the photon vector pointing from the center of the bar end to the center of the tube. This vector is then extrapolated back into the quartz bar using Snell's law, where the exit angles (ϕ_C, θ_c) with respect to the track are calculated. Most of the photon phase space $(\alpha_x, \alpha_y,\ t_{hit})$ is mapped onto the Cherenkov angles (ϕ_c, θ_c). The contribution of timing, apart from resolving the

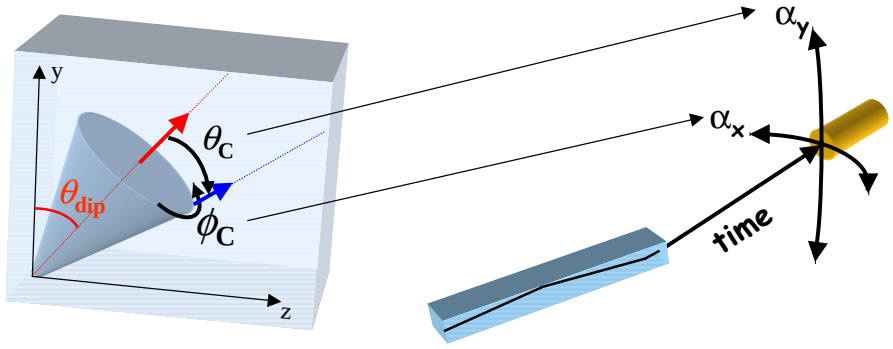

Figure A.4: A cartoon to illustrate the DIRC as a three-dimensional imaging device.

forward-backward photon propagation, is not competitive with the position information, but it is crucial for the suppression of beam background that have a different time structure.

A.2. Timing

An important observable for a Cherenkov photon in the DIRC is the difference, Δt between its measured arrival time, t_m, and expected, arrival time, t_e. The measured arrival time is obtained in several steps:

Bunch crossings in the PEP-II ring occur with a minimum spacing of 4.2 ns, while

relevant physics is accepted at a rate of about 2 kHz. In the level-one (L1) trigger the bunch-crossing time is derived by fast pattern recognition in the super-layers of the drift chamber with a precision of about 70 ns (time jitter). This compares to the 50 ns width of the time distribution of Cherenkov photons created by tracks of a typical collision event in the quartz bars. To collect all photons of an event the readout interval in the DIRC is set to $\pm$300 ns with respect to the L1-trigger time.

The DIRC time, t_{hit}, measurement is provided by a custom made digital chip TDC [64] that resides in the front-end boards mounted on the standoff box. The digitization clock is obtained by subdividing the 59.5 MHz *BABAR* system clock into 5 bits to result in 0.525 ns wide time bins. It was chosen as a function of the 1.4 ± 0.2 ns photo-tube resolution. The time value is stored in a memory buffer for 12 μs, the time it takes for the L1-trigger to complete its operation. The hit time information is transferred by a 1.2 Gbit/s optical fiber from the front-end electronics of the twelve sectors pairwise into six readout modules (ROMs).

At the level of reconstruction, the calibration time t_c is corrected for different delays in the readout electronics and photo-tube response time variations are applied. These are determined with a light pulser system which generates 1 ns pulse duration from a blue light LED, inserted by an optical fiber into 12 diffusers which are located above each bar box window facing the photo-tubes. The pulser produces roughly 10% photo-electron occupancy almost uniformly throughout the photo-tube array.

The pulser is run at about 2 kHz to collect approximately 65,000 light pulses for the determination of the mean-time delay of each tube with a statistical uncertainty of better than 0.1 ns. The time delay values per channel are typically stable to a rms of less than 0.1 ns over more than one year of daily calibrations.

A measure of the bunch-crossing time, t_b, comes from a combined fit to drift-chamber tracks. Therefore, the resolution of t_b depends on the track multiplicity and angular distributions. A typical resolution is about 2.5 ns.

Finally, the measured time calculated from:

$$t_m = t_{hit} - t_{trigger} - t_c - t_b - t_{offset}. \tag{A.2}$$

where t_{offset} is a global time offset. The precision in the parameter t_m for a Cherenkov photon is dominated by the bunch-crossing time t_b. Cherenkov photons originating from charged tracks in a collision event cluster in the arrival time as measured by the DIRC. The mean arrival time of the Cherenkov photons in an event, $\langle \delta t \rangle_{\text{event}}$, has a resolution of 100 - 200 ps. In practice, this self-triggering feature of the DIRC corrects the uncertainty in the bunch-crossing time (neglecting systematic corrections from detector alignment, trigger jitters or calibration). Furthermore, the mean value of the $\langle \delta t \rangle_{\text{event}}$ for a given run measures the deviation from t_{offset}.

The expected arrival time, t_e, of the Cherenkov photon is a sum of the time-of-flight of the charged track from its origin to the quartz bar (typically 3-5 ns), the

photon propagation time in the quartz bar and the prism along its reconstructed path and the time to travel through the water before reaching the surface of the photomultiplier (typically 25-70 ns). The photon propagation time is given by

$$t_p = \frac{L n_g}{c k_z}. \tag{A.3}$$

where L is the bar length, where the photon group velocity ($v_g = \frac{c}{n_g}$) is used instead of the phase velocity ($v_p = \frac{c}{n}$). Since in a dispersive medium energy propagates at the photon group velocity. The relation between the group and phase velocities as a function of the photon wavelength λ is given by

$$n_g(\lambda) = n(\lambda) - \lambda \frac{dn(\lambda)}{d\lambda}. \tag{A.4}$$

For fused silica, n_g is typically several percent larger than $n(\lambda)$ for photons in the energy range detectable by the PMTs. The weighted average value $\left\langle \frac{n(\lambda)}{n_g(\lambda)} \right\rangle \approx 0.97$. In the earlier DIRC reconstruction the photon phase velocity was used to calculate the propagation time. As a part of my DIRC software project I helped establish the value of 0.97 by using a sample of dimuon events that is now used in the reconstruction code.

The spread in the arrival time of a photon is greater than the average bunch crossing. Applying $\langle \delta t \rangle_{\text{event}}$ as a correction yields a precision of better than 1.7 ns

in $\Delta t = t_m - t_e$ - $< \delta t >_{\text{event}}$ which is close to the intrinsic time resolution of the phototubes.

In principle, the resolution of the bunch-crossing time t_b becomes infinitesimal small if one can identify the occurrence of the bunch that collided in the PEP-II fill pattern. The minimum bunch spacing of 4.2 ns is set by the overall 476 MHz system clock common to PEP-II and *BABAR*. However current operational pattern consist of varying spacing of 12.8 ns, 8.4 ns or even alternating between 8.4 ns and 4.2 ns. Due to this variation, the colliding bunches are found empirically from a fit of the bunch pattern to the event Δt.

A.3. Operational Issues

Interactions of lost beam particles with residual gas in the beam pipe (bremsstrahlung, Coulomb scattering) produce low energy photons with energies between 2 MeV and 2.5 MeV for 90% of them. These penetrate the water in the standoff box and the quartz bars and can generate secondary Cherenkov photons due to electrons from Coulomb scattering. Another source of secondary Cherenkov light is not a physical source due to lost beam particles. They preferentially hit beam pipe elements and produce secondaries which can enter the standoff box. They produce so-called "hot spots" in the read-out.

For a maximum background photon hit rate per photo-tube of 200 kHz one expects

1300 hits in a ±300 ns readout time window corresponding to 12% occupancy. The readout efficiency rapidly degrades when counting rates exceed this threshold. The TDC and readout electronics dead-time reaches several percent at 300 kHz and 20% at 700 kHz single tube hit rate. At the highest current luminosity the rate of single photon hits per tube is kept below 200 kHz. Therefore, fast feedback to the Pep-II control provided by an analog signal from a tube in the innermost row of each standoff-box sector. Locations of beam related hot spots are tracked with CsI-crystal detectors placed along the beam-pipe and then covered with local lead shielding. A cylindrical lead shielding in the inner radius of the standoff box was inserted during the fall of 2001 to reduce the occurrence of hot spots. To improve the DIRC data acquisition robustness, an upgrade of the TDC has been designed to keep the dead-time at a few percent for rates up to 1 MHz. Installation is scheduled for the summer 2002 shutdown.

On the other hand, in a time interval of ±8 ns about 11 randomly distributed photons are present while for a typical multi-hadron event with 8 charged tracks entering the quartz bars at the same time all 240 signal photons are recorded. This demonstrates the potential use of the time observable Δt in suppressing background at the reconstruction level. In Fig. A.5 the dramatic effect is shown for a dimuon event.

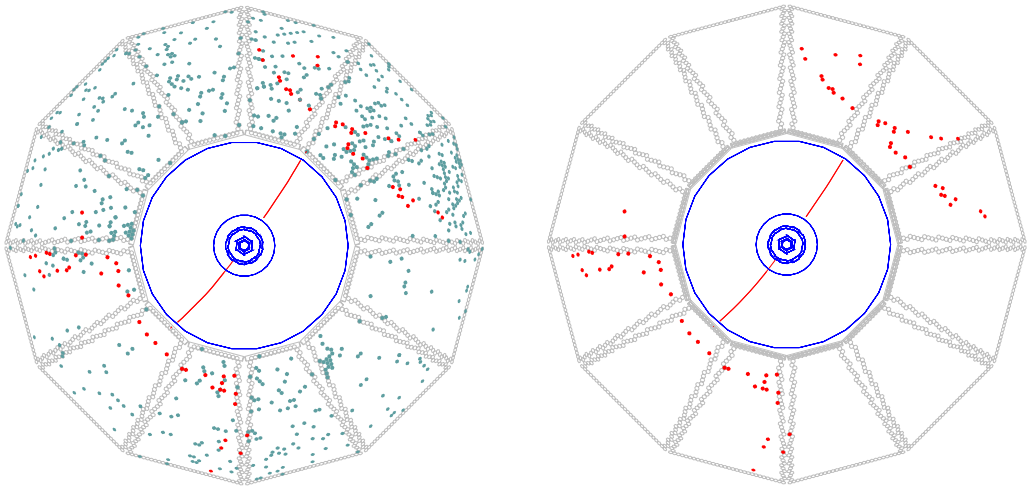

Figure A.5: A typical $e^+e^- \to \mu^+\mu^-$ event in the $r\phi$ projection of the standoff box. Left: Photo-multipliers which detect light within a time interval of ± 300 ns centered at the beam crossing time are shown as dots. Right: Only those photo-tubes are plotted which were hit within 8 ns of the expected Cherenkov photon arrival time.

A.4. Performance

In the absence of correlated systematic errors, the resolution ($\sigma_{C,track}$) on the track Cherenkov angle should scale as

$$\sigma_{C,track} = \sigma_{C,\gamma}/\sqrt{N_{pe}}. \tag{A.5}$$

In Figure A.6 we show the single photon angular resolution obtained from dimuon events in data. There is a broad background of less than 10% relative height under the peak, that originates mostly from track-associated sources, such as δ rays, reflections off the glue-fused silica boundaries, and combinatorial background [65]. As a part of

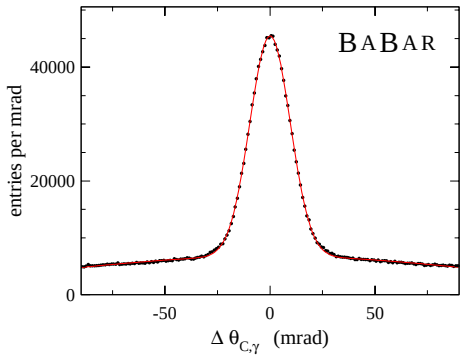

Figure A.6: The difference between the measured and expected Cherenkov angle for single photons, $\Delta\theta_{c,\gamma}$ for single muons in $\mu^+\mu^-$ events. The curve shows the result of a fit of two Gaussians to the data. The width of the narrow Gaussian is 9.6 mrad.

DIRC software work the author made comparative studies between DIRC Monte Carlo and data. In Fig. A.7 we show Monte Carlo and data Cherenkov angle reconstruction. This indicates a 20% discrepancy between the amount of background level in Monte Carlo and data. This is because the Monte Carlo does not include effects due to refraction off the glue and underestimates the amount of δ rays. The track Cherenkov angle resolution for dimuon events is shown in Figure A.8. The width of the fitted Gaussian distribution is 2.4 mrad compared to the design goal of 2.2 mrad.

The measured time resolution is 1.7 ns, close to the intrinsic 1.5 ns transit time spread of the PMTs. The number of photo-electrons shown in Figure A.9 varies between 16 for small values of $|\cos\theta_{\rm track}|$ at the center of the barrel and 60 at large values of $|\cos\theta_{\rm track}|$. This variation is well reproduced by Monte Carlo simulation, and can be understood from the geometry of the DIRC. The number of Cherenkov photons varies with the path-length of the track in the radiator, it is smallest at

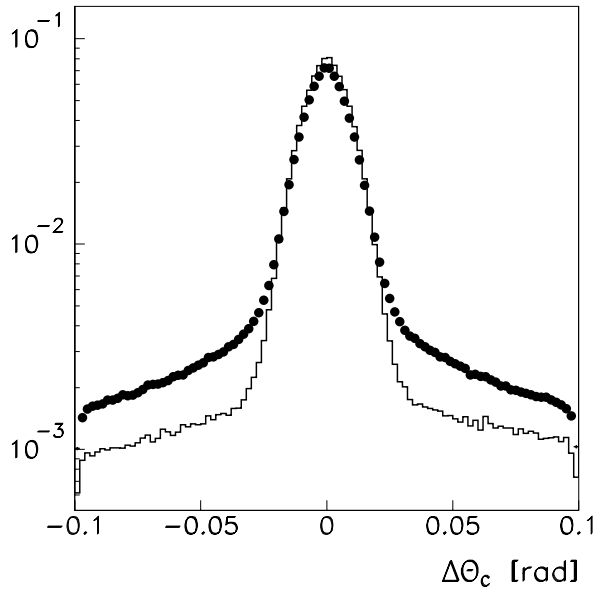

Figure A.7: The single photon Cherenkov angle distribution for the muon track as reconstructed in the DIRC for data(dots) and Monte Carlo(line) overlayed. On the y axis is the probability plotted on a log scale.

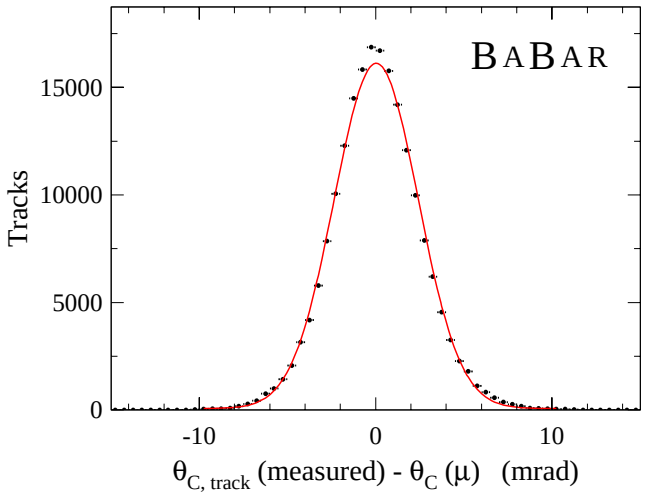

Figure A.8: Resolution of the reconstructed Cherenkov polar angle per track for dimuon events. The curve shows the result of a Gaussian fit with a resolution of 2.4 mrad.

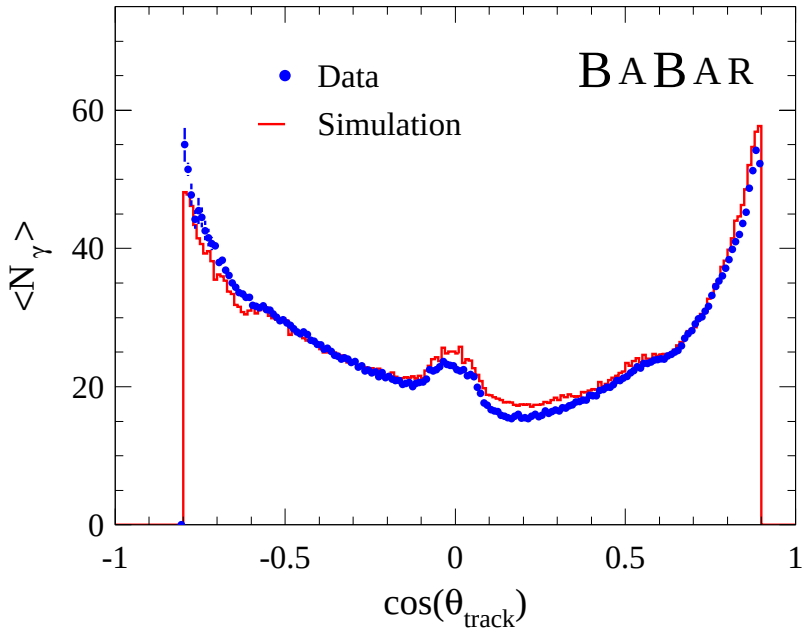

Figure A.9: Number of detected photons versus track polar angle for reconstructed tracks in dimuon events compared to Monte Carlo simulation.The mean number of photons in the simulation has been tuned to match the data.

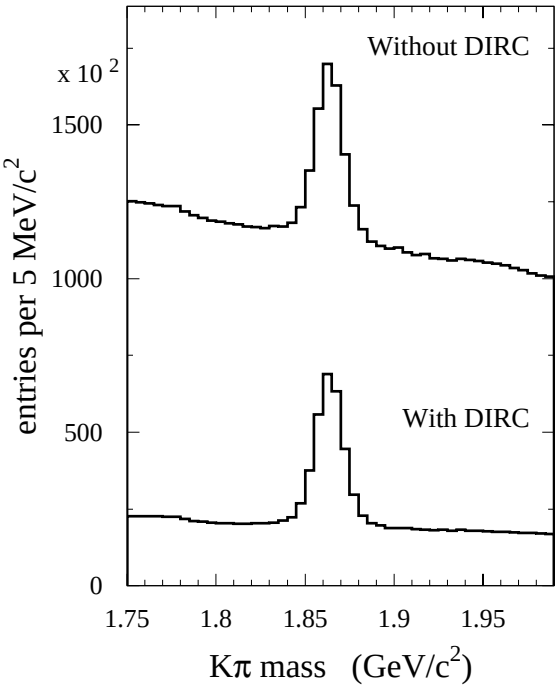

Figure A.10: Invariant Kπ inclusive mass spectrum with and without the use of the DIRC for kaon identification. The mass peak corresponds to the decay of the D^0 particle.

perpendicular incidence at the center and increases towards the ends of the bars. In addition, the fraction of photons trapped by total internal reflection rises with larger values of $\mid \cos\theta_{\rm track} \mid$. This increase in the number of photons for forward going tracks is a good match to the increase in performance required at larger momentum.

The $K\pi$ invariant mass spectra is shown as an example of the use of the DIRC for particle identification is in Figure A.10. It is seen that the ratio of signal to background increases by a factor of five from without the DIRC to with the DIRC used for particle identification. The peak corresponds to the decay of the D^0 particle.

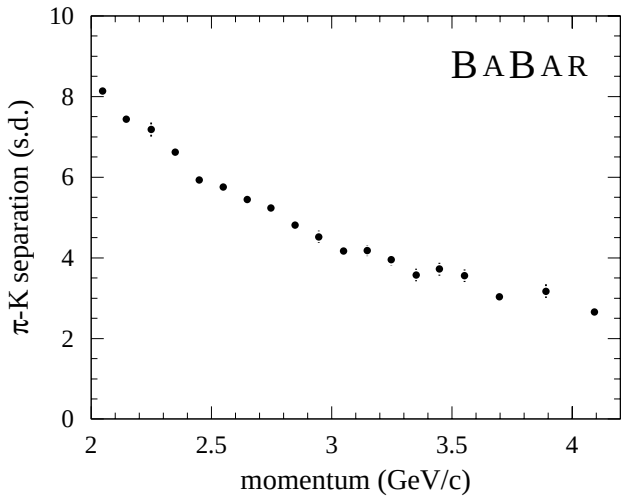

Figure A.11: DIRC π-K separation versus track momentum measured in $D^0 \to K^-\pi^+$ decays selected kinematically from inclusive D^* production.

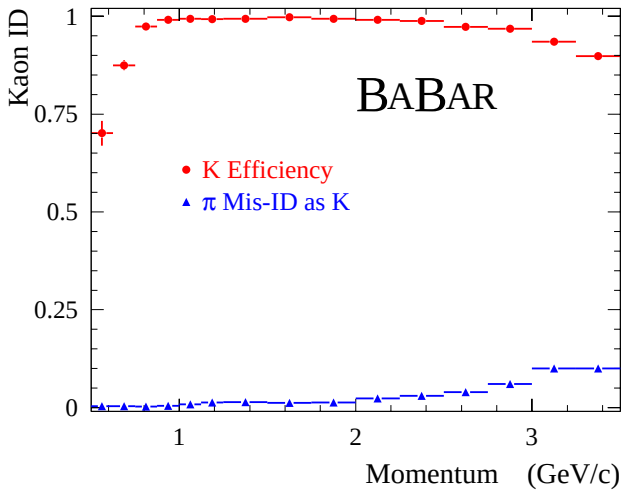

Figure A.12: Efficiency and misidentification probability for the selection of charged kaons as a function of track momentum, for a particular choice of particle selection criteria. The data use $D^0 \to K^-\pi^+$ decays selected kinematically from inclusive D^* production.

Due to the small mass difference between the D^* and the D^0 the decay of D^* can be kinematically well constrained by its decay to a D^0 and a slow π. The D^0 decays to a kaon and a pion. Thus there are three charged tracks where the two π's have the same charge while the kaon has the opposite charge. This constraint helps measure the signal over background in the decay of the D^*. Thus the PID performance of the DIRC has been studied with a sample of pions and kaons, selected kinematically using $D^0 \to K^-\pi^+$ decays from inclusive D^* production. The pion-kaon separation power of the DIRC was defined as the difference of the expected Cherenkov angles for pions and kaons, divided by the measured track Cherenkov angle resolution. As shown in Figure. A.11, the separation between kaons and pions at 3 GeV/c is about 4.4σ, which is within 10% of the design goal.

The efficiency to identify correctly a charged kaon that traverses a radiator bar and the probability to mis-indentify a pion as a kaon are also determined from the inclusive D^* sample. This is shown as a function of the track momentum in Figure A.12 for a particular choice of particle selection criteria. The kaon selection efficiency and pion misidentification, integrated over the K and π momentum spectra of the D^* control sample, are $97.97 \pm 0.07\%$ (stat. only) and $1.83 \pm 0.06\%$ (statistics only), respectively.

A.5. Summary

The new type of Cherenkov detector DIRC developed for *BABAR* is well suited for the particle identificaton requirments of the experiment. It has been a crucial component of many published physics analysis including the flagship $\mathcal{CP}$ violation measurements.

The DIRC has been robust and stable for three years and is operating essentially in factory mode. 99% of all photomultiplier tubes and electronic channels operating with nominal performance.

The detector performance achieved is close to that predicted by the Monte Carlo simulations, though alignment and additional code developments are expected to provide further improvements.

Bibliography

[1] C. S. Wu, *et al.*, Phys. Rev. 105, 1413 (1957).

[2] J. H. Christenson *et al.*, Phys.Rev.Lett **13**, 138 (1964).

[3] D. Andresa *et al.*, Phys. Rev. Lett **45**, 219 (1980).

[4] V. Fanti *et al.*, Phys. Lett. B 465, 335-348(1999).

[5] A. Alvi-Harati *et al.*, Phys. Rev. Lett. 83, 22-27(1999).

[6] *BABAR* Collaboration, (B. Aubert *et al.*), Phys. Rev. Lett. **86** 2515 (2001).

[7] The BELLE Collaboration, (A. Abashian *et al.*), Phys. Rev. Lett. **86** 2509 (2001).

[8] M. Kobayashi and T. Masakawa, $\mathcal{CP}$ Violation In the Renormalizable Theory of Weal Interaction, Prog.Theor.Phys.**49**,752,(1973).

[9] G. C. Branco, L. Lavoura, J. P. Silva, $\mathcal{CP}$ Violation (Oxford Science Publications, 1999).

[10] A. D. Sakharov, Violation of $\mathcal{CP}$ Invariance, C Asymmetry, And Baryon Asymmetry of the Universe, Pisma Zh.Eksp.Teor.Fiz **5**, 32(1967).

[11] C. Itzykson, J. Zuber, Quantum Field Theory (McGraw-Hill,1980).

[12] $\mathcal{CPT}$ theorm was discovered by J. Schwinger and G. Lunders and perfected by W. Pauli, N. Bohr. The Development of Physics, W.Pauli, ed. (New York: McGraw-Hill, 1955).

[13] The CPLEAR Collaboration, Phys. Lett. B, Vol 471(2-3)(1999) pp 332-338.

[14] I.I. Bigi, A.I. Sanda, $\mathcal{CP}$ Violation.

[15] P. F. Harrison and K. R. Quinn [*BABAR* Collaboration], The *BABAR* Physics Book: Physics at the asymmetric B factory, (1998).

[16] *BABAR* Collaboration, (B. Aubert *et al.*), hep-ex/0112044.

[17] Particle Data Group (C. Caso *et al.*), Review of Particle Physics (2000).

[18] I. I. Bigi *et al.*, in $\mathcal{CP}$ violation, ed. C. Jarlskog, World Scientfic, Singapore (1992).

[19] A. Ali, "B Decays - Introduction and Overview", in B Decays, ed. S. Stone, World Scientific (1994).

[20] M. K. Gaillard and B. W. Lee, Phys. Rev. D. **10**, 897, (1974b).

[21] G. D. Rochester and C. C. Bulter, Nature 160, 855 (1947).

[22] N. Cabibbo, Phys. Rev. Lett **10**, 531 (1963).

[23] L. Wolfenstein, Phys. Rev. Lett. **51**, 1945 (1983).

[24] C. Jarlskog, Phys. Rev. Lett. 55, 1945 (1983).

[25] The *BABAR* Collaboration (B. Aubert *et al.*), hep-ex/0203007.

[26] D. London, N. Sinha and R. Sinha, Phys. Rev. Lett. **85**, 1807 (2000).

[27] The CLEO Collaboration (J. P. Alexander *et al.*), Phys. Rev. Lett **77**, 5000 (1996).

[28] *BABAR* Collaboration, B. Aubert *et al.*, Nucl. Instr. and Methods **A479**, 1 (2002).

[29] The vender of fused silica: TSL Group PCL,

P.O. Box 6, Wallsend, Tyne & Wear, NE28 6DG, England.

Quartz Products Co., 1600 W. Lee St., Louisville, Kentucky 40201.

Manufacturer of quartz bars: Boeing, Rockedyne Division, 2511 C Broadbent Parkway NE, Albuquerque, New Mexico 87107.

[30] R. Santonico, R. Cardarelli, Nucl. Instr. Methods A187 (1981) 377.

[31] The CLEO Collaboration (M.S. Alam *et al.*), Phys. Rev. **D50** (1994), 43.

[32] The CLEO Collaboration (B.H. Behrens *et al.*), Physics Letters B, Volume 490, Issue 1-2, (2000), pp. 36-44

[33] Private communication with Dr. Jinglong Zhang.

[34] Nucl. Phys. **B149** (1979), 413; [E: ibid. **B157** (1979), 543].

[35] The CLEO Collaboration, ICHEP98 852, CLEO CONF 98-23 (1998).

[36] R. A. Fisher, The use of multiple measurements in taxonomic problems, Annals of Eugenics **7**, (1936) 179-188.

[37] B. Ford *et al.*, Choice of Kinematic Variables in B Meson Resonstruction, *BABAR* Analysis Document #53 (2000).

[38] S. Spanier, Kaon Selection at the *BABAR* Experiment, *BABAR* Analysis Document # 116 (2000)

[39] U. Langenegger *et al.*, Cut-Based Electron Identification, *BABAR* Analysis Document # 90 (2001).

[40] L. Lista *et al.*, Muon Identification in the BaBar Experiment, *BABAR* Analysis Document # 60 (2000).

[41] R.Kerth *et al.*, The *BABAR* coordinate system and units, *BABAR* note 230 (1995).

[42] Siegmund Brandt, Statistical and Computational Methods in Data Analysis, Ed. North-Holland, 1973.

[43] Vertexing and Composition Tools group, The *BABAR* Vertexing, *BABAR* analysis document 102 (2000)

[44] S.Meztler, *et al.* , Measurement of B Lifetimes at *BABAR* *BABAR* analysis document # 65, 2000

[45] D.Kirkby, Generator Level Studies for $B^0\overline{B}^0$ M̃ixing, http://www.slac.stanford.edu/d̃avidk/BBMix/GenStudy, 2000

[46] J.Back *et al.*, A users giude to the RooFitTools package for unbinned maximum likelihood fitting, *BABAR* analysis document # 18

[47] Eric Charles thesis, University of Wisconsin,
"A measurement of the $\mathcal{CP}$ Parameter $sin(2\beta)$ Using Fully
Reconstructed $b \to c\bar{c}$ Decays at the *BABAR* Experiment".

[48] C. Hearty, Measurement of the Number of Upsilon(4S) Mesons Produced in Run1 (B Counting), *BABAR* analysis document # 134 (2001)

[49] GEANT Detector Description and Simulation Tool, Version 3.21, CERN Program Library W5103, CERN (unpublished) (1995).

[50] F.James, Minuit Function minimization and error analysis, CERN progam library long writeup D506 (1994)

[51] H. Albrecht *et al.*, (ARGUS Collaboration), *Phys. Lett.* **B 254**, 288 (1991).

[52] W . T. Eadie *et al.*, Statistical Methods in Experimental Physics, North Holland, (1988)

[53] R. Brun and D. Lienart, HBOOK User Guide, CERN Program Library Y250 (HDIFF routine)

[54] Jan Stark *et al.*, Measurement of the charged and neutral B meason lifetime using fully reconstructed B decays, *BABAR* analysis document #144, (2001)

[55] Particle Data Group,K. Hagiwara *et al.*, Phys. Rev. D **66** 010001-1 (2002)

[56] M. Margoni, M. Rotondo, and F. Siminotto,
A measurement of B^0 lifetime with $B^0 \to D^* l\nu$ using inclusive reconstruction, *BABAR* analysis document #182 (2001).

[57] http://babar-hn.slac.stanford.edu:5090/HyperNews/get/event_gen/151/1.html.

[58] http://www.slac.stanford.edu/BFROOT/www/Physics/Tools/PepBeam

[59] *BABAR* collaboration D. Boutigny *et al.*, Technical design report, SLAC-R-95-457 (1995)

[60] W. Dunwoodie *et al.*, Study of material interactions with gamma conversions and protons, *BABAR* analysis document # 106 (2001)

[61] B. Ratcliff, SLAC-PUB-5946 (1992), SLAC-PUB-6047 (1993);
P. Coyle *et al.*, Nucl. Inst. Methods A343, 292 (1994).

[62] The *BABAR* DIRC Collaboration, I. Adam *et al.*,
IEEE Trans. Nucl. Sci. 45 (1998) 450, 657

J. Cohen-Tanugi, M. C. Convery, B. N. Ratcliff, X. Sarazin,

J. Schwiening, J. Va'vra, SLAC-JOURNAL-ICFA-21,

ICFA Instrumentation Bulletin, Fall 2000 Issue.

[63] I. Adam *et al.*, IEEE Trans. Nucl. Sci. **45** No. 3 (June) 657;

[64] P. Bailly, J. Chauveau, J.F. Genat, J.F. Huppert, H. Lebbolo, L. Roos, *et al.*, A 16-channel digital TDC chip, Nucl. Instr. Meth. A vol. #1 (1999) pp. 432-437.

[65] A. Yarritu, S. Spanier and J. Va'vra, SLAC-PUB-9073 (2001), submitted to IEEE Trans. Nucl. Sci.